7-12-2014

Optical Filaments and Gas Dynamics in Air

Jeremy Yeak

Jeremy Yeak

Candidate

Electrical and Computer Engineering

Department

This dissertation is approved, and it is acceptable in quality and form for publication:

Approved by the Dissertation Committee:

Edl Schamiloglu  , Chairperson

Mansoor Sheik-Bahae

Mark Gilmore

Norman Roderick

Edward Walters

Optical Filaments and Gas Dynamics in Air

by

Jeremy Yeak

B. Eng., Universiti Putra Malaysia, 1999
M.S., OSE, University of New Mexico, 2008

DISSERTATION

Submitted in Partial Fulfillment of the
Requirements for the Degree of

Doctor of Philosophy
Optical Science and Engineering

The University of New Mexico

Albuquerque, New Mexico

May, 2014

Dedication

To my parents and my family for their continuous love and support...

"The difference between fact and fiction is that fiction has to make sense."

– Tom Clancy

Acknowledgments

First and foremost, I would like to thank Prof. Jean-Claude Diels for opening my eyes to the world of optics and femtosecond lasers. I am grateful to him for the knowledge he has imparted to me, and also for his patience and guidance over the many years I have spent in Albuquerque, New Mexico.

The research presented in this dissertation would not have been possible without the support from Dr. Kevin Kremeyer at Physics, Materials and Applied Mathematics (PM&AM) Research, LLC. I would like to thank him for guiding me professionally, and in terms of gas dynamics, providing me the resources to further pursue experimental investigations in Tucson, and also for proof-reading my dissertation. Credit must also given to Mr. Charles Suchomel at Wright Patterson Air Force Base and Dr. Victoria Franques at the Department of Energy for their support and funding my work in Tucson. Without them, this research would not have borne much fruit.

My thanks also go to my previous lab mates at the University of New Mexico. Among them are Dr. Jens Schwarz, Dr. Olivier Chalus, Dr. Daniel Mirell, and Dr. Alexander Albrecht. They have provided me with moral support and comfort when experiments didn't go quite as planned. I also would like to thank my former and current colleagues at PM&AM Research who have nagged me to finish my dissertation.

I also want to thank my Ph.D. committee members who have taken the time and effort to review my dissertation, and have provided wonderful technical feedback to make this dissertation even better. They include Prof. Mansoor Sheik-Bahae, Prof. Ed Walters, Prof. Norm Roderick and Prof. Mark Gilmore.

Last but not least, I would like to thank Prof. Edl Schamiloglu, the chair of my Ph.D. committee, who has not only given me the opportunity and motivation to complete my dissertation, but also advised me how to navigate through sticky situations. He has also provided me with valuable feedback to the writing of this dissertation. Without his patience and belief in me, all this would not have been possible.

Optical Filaments and Gas Dynamics in Air

by

Jeremy Yeak

B. Eng., Universiti Putra Malaysia, 1999
M.S., OSE, University of New Mexico, 2008

Ph.D., OSE, University of New Mexico, 2014

Abstract

Until now, the propagation dynamics of intense ultrashort laser pulses leading to optical filamentation in air has only been investigated in the frame of a dynamic balance between linear diffraction, Kerr self-focusing and plasma defocusing. This has led to the development of different theories surrounding the generation and persistence of optical filaments propagating over many Rayleigh lengths in air. These theories include wave-guiding model, moving focus model, dynamic spatial replenishment model and conical wave model. However, these models fail to capture the gas dynamics that arise from optical filaments interacting with air.

In this work, we demonstrate that initial conditions are critical to the formation of optical filaments through the use of an aerodynamic window. Filament characteristics in air, such as spectral broadening, electrical conductivity and fluorescence, are measured and presented. Using these as diagnostic tools, we also show that the optical filamentation of ultrashort laser pulses can be enhanced at high repetition rates because of the thermal response of air, resulting from the interaction of each

laser pulse with the modified atmospheric density distribution left behind by the preceding pulse. This is explained by the sudden deposition of energy by a filament in the air which generates a cylindrical shock wave, leaving behind a column of rarefied air. This low-density region persists for an extended period and can materially affect the propagation dynamics of an ensuing pulse that follows before the low-density region has relaxed sufficiently to ambient conditions. By further increasing the repetition rate, the onset of ionization is shifted downstream and the spectral continuum displays a stronger broadening on both sides of the original pulse spectrum. This gas dynamic interaction regime of filamentation can be utilized to enhance the length and spectral width of filaments for remote sensing and long range laser-induced high voltage discharges.

Contents

List of Figures

List of Tables

Glossary

Abbreviations

a.u.	Arbitrary units
AR	Antireflection
ASE	Amplified spontaneous emission
CCD	Charge-coupled device
CMOS	Complementary metal-oxide semiconductor
CPA	Chirped-pulsed amplifier
cw	Continuous wave
DC	Direct current
EM	End mirror
FM	Folding mirror
FP	Faraday rotator (polarizer)
FWHM	Full width at half maximum

FROG	Frequency-resolved optical gating
GIM	Grazing incidence mirror
GP	Glan polarizer
GS/s	Gigasamples per second
GVD	Group velocity dispersion
HWP	Half-wave plate
ICCD	Intensified charge-coupled device
IR&D	Internal Research and Development
IR	Infrared
KLM	Kerr-lens mode-locked (oscillator)
KTP	Potassium titanyl phosphate
LIBS	Laser-induced breakdown spectroscopy
LIDAR	Light detection and ranging
Nd:YAG	Neodymium-doped yttrium aluminum garnet (laser)
Nd:YLF	Neodymium-doped yttrium lithium fluoride (laser)
OC	Output coupler
PBS	Polarizing beamsplitter
PC	Pockels cell
PM&AM	Physics, Materials, and Applied Mathematics Research, L.L.C.

PMT	Photomultiplier tube
SPM	Self-phase modulation
Ti:S	Titanium:sapphire (laser)
TFP	Thin film polarizer
TSP	Team Specialty Products
TTL	Transistor-transistor logic
UNM	University of New Mexico
UV	Ultraviolet
WP	Waveplate

Roman symbols

b	Crystal axis
A, B	Nonlinear coefficients in polarization vector
c	Speed of light
C	Capacitance
C_h	Heat capacity
d	Gap between electrodes
d_{QW}	Thickness of quantum well
e	Electrons or electronic charge
E	Electrical field strength

E_A	Electron affinity
f	Focal length of a lens
$\hbar$	Reduced Planck's constant
I	Laser pulse intensity
k	Wavenumber
K	Number of photons
l	Cavity length
L_d	Characteristic dispersion length
n	Index of refraction
n_0	Linear index of refraction
$n_t h$	Thermal index of refraction
$\tilde{n}_2$	Nonlinear index of refraction
m_e	Mass of electron
p_0	Ambient pressure
P	Power
$P(E)$	Polarization
P_{cr}	Critical power
r	Radius of low density tube or radial coordinate
R	Resistance

t	Time
T	Temperature
T_l	Laser-induced temperature change
U_I	Ionization potential
$\bar{v}$	Average speed
V	Voltage
w	Gaussian beam size (diameter)
w_0	Minimum spot size (diameter)
x, y, z	Cartesian coordinates
z_R	Rayleigh range

Greek symbols

α_0	Gain or absorption coefficient
α_K	Transition rate of K-photon ionization
β_K	K-photon ionization cross section
γ	Keldysh parameter
ϵ_0	Electric permittivity of vacuum
λ	Laser wavelength
κ	Thermal conductivity
ν	Laser frequency

ρ_c, ρ_e, ρ_0	Critical plasma density, electron plasma density, air density
σ	Ionization cross section
ϕ	Phase of laser pulse
χ	Susceptibility of the medium
ω	Radial frequency of the laser

Chapter 1

Introduction

1.1 Overview

Over the past two decades, ultrashort pulse lasers have seen remarkable progress and development. In the 1980's, ultrashort pulse referred to picosecond pulses, which were generated by active or passive mode-locked lasers. These mode-locked lasers were vastly different from Q-switched lasers that produced nanosecond pulses. In the 1990s, the term "ultrashort pulse" referred to femtosecond pulses and, at the turn of the millenium, attosecond pulses. As a result of generating shorter and shorter pulses with correspondingly higher peak powers, a plethora of nonlinear phenomena have been discovered. One remarkable phenomenon is filamentation. In all transparent media (solids, liquids and gases), once the critical power for self-focusing is exceeded, the laser pulse will self-focus, marking the onset of filamentation. In solids and liquids, stimulated Raman and Brillouin scattering counter-balance the self-focusing action of the nanosecond pulses by depleting the pulse energy, and thus, forming self-trapped channels within the transparent media. With femtosecond pulses, a much more dynamic picture emerges. As the femtosecond pulse self-focuses in air, the

intensity of the laser pulse increases, generating free electrons through multiphoton ionization. This has an effect of defocusing the beam, and thereby reduces the intensity of the laser pulse. Typically, a filament is formed at the center core of the laser beam where the intensity is at its highest, and surrounded by an energy reservoir that replenishes the energy lost in a filament due to ionization and absorption losses. This dynamic balance ensures that the femtosecond filament propagates over long distances in air. Consequently, the intensity within a filament is usually clamped to about 5 x 10^{13} W/cm^2 in air [1]. This means that roughly 0.5 mJ of energy gets trapped inside a 100 μm filament formed by a 30 fs laser pulse in air.

While there have been numerous publications on filamentation of intense femtosecond pulses in air, a complete and cohesive understanding of this highly complex phenomenon is still elusive. Nonetheless, the interest in filaments has only intensified as scientists are still discovering new subtleties of filamentation in air. Some of the remarkable characteristics of a filament are described below to underline its potential for a variety of applications.

1.2 Long Range Propagation

Although the first filaments were observed in glass using nanosecond pulses back in 1964 [2], femtosecond filaments in air were only discovered in 1995 when gigawatts of peak powers became available. Braun *et al.* observed small-scale filamentation in air using 200 fs pulses with pulse energies up to 50 mJ in the near IR at a central wavelength of 775 nm [3]. These filaments were formed at a distance of 10 meters away from the grating compressor, and continued to propagate for another 20 meters. In that same year, Prof. Jean-Claude Diels' team at the University of New Mexico reported UV filaments at 248 nm [4]. They observed multiple filaments being formed using 0.5–1 ps pulses with energies in excess of 100 mJ after propagating

over 10 meters. The experimental demonstration of filaments in air (both in the near infrared and ultraviolet range) was a breakthrough, as it signified a paradigm shift from viewing filaments as deleterius (because they caused damage tracks in a solid-state laser gain medium – distorting the profile of the amplified beam and reducing the output power) to a much desired property for cleaning the spatial profile of the laser beam as it propagated through turbulent air over long distances.

This hallmark of a filament stems from its ability to overcome linear diffraction, and thus propagate over many Rayleigh lengths with a characteristic sub-millimeter beam diameter. It is achieved when the peak power of the laser beam undergoing filamentation exceeds the critical power for self-focusing.

1.3 Electrical Property

Early experiments pointed to the existence of a plasma trail left in the wake of femtosecond pulses. Due to the high peak powers in these very short pulses, the electric fields are sufficiently high to ionize air molecules. The generation of free electrons can be attributed to multiphoton ionization and/or tunneling ionization depending on the laser wavelength and pulse duration. The Keldysh parameter γ [5] provides a good rule of thumb to indicate the dominant ionization process. The Keldysh parameter γ can be defined as [6]:

$$\gamma = \nu \frac{\sqrt{2 m_e U_I}}{e E_0} \tag{1.1}$$

where ν is the frequency of the laser, e and m_e are the electronic charge and mass, respectively, U_I is the ionization potential of the medium, and E_0 is the electric field strength of the laser pulse (in V/m). The value of the Keldysh parameter γ discriminates between two gaseous ionization processes. If $\gamma \gg 1$, the dominant ionization regime is multiphoton ionization, and if $\gamma \ll 1$, tunneling ionization is dom-

inant. For example, assuming that the intensity inside a filament in air is clamped at 5 x 10^{13} W/cm^2, then $\gamma = 0.45$ for a central wavelength $\lambda = 800$ nm. If $\lambda = 266$ nm (in the ultraviolet wavelength range), $\gamma = 1.36$. Thus, for shorter wavelengths, multiphoton ionization is mainly responsible for the generation of free electrons using intense laser pulses.

The occurence of a tenuous plasma over long distances has sparked interest in using filaments to trigger and guide lightning discharges with femtosecond laser pulses [7]. Experiments have been conducted in the laboratory demonstrating both the reduction of the electrical breakdown threshold of air and the guidance of the electrical discharge along the electrically conductive laser/filament channel [8, 9]. Fig. 1.1 shows the visible plasma generated by a 2.5 mJ, 30 fs laser pulse with central wavelength $\lambda = 800$ nm by a lens with focal length $f = +0.75$ m. (The direction of the laser beam propagation is from left to right.)

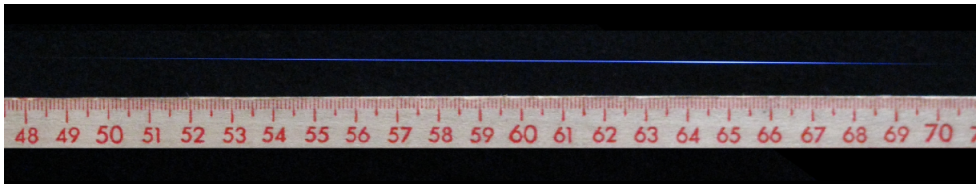

Figure 1.1: A laser plasma in air generated by focusing 2.5-mJ, 30-fs pulses at $\lambda = 800$ nm by an $f = +0.75$ m lens. (PM&AM Research, IR&D)

The energy expended during the ionization of air caused by focusing the intense laser pulse can be estimated. Using an $f = +0.75$ m lens to focus down an 800 nm laser pulse with an initial beam size of 8 mm (full width at half maximum), the minimum spot size is $w_0 = 150$ μm and the Rayleigh range $z_R = 8.8$ cm. If the collimated length is defined as twice the Rayleigh range, the ionization channel is expected to be $2z_R = 17.7$ cm, which is roughly the length of the plasma shown in Fig. 1.1. At 1 atm and at 20 °C, the density of air molecules is 2.5 x 10^{25} m^{-3}. (This is close to Loschimdt's number, $n_0 = 2.687$ x 10^{25} m^{-3}. However, Loschimdt's number is

defined as the density of an ideal gas molecules at 0 °C and at 1 atmosphere pressure.) Assuming the composition of air molecules to be 20% oxygen and 80% nitrogen, and taking the ionization potentials of O_2 and N_2 to be 12.07 eV and 15.58 eV, respectively, the amount of energy needed to singly ionize all the air molecules in a cylindrical volume of $\frac{1}{2}\pi z_R {w_0}^2$ is $E = 186$ mJ. However, the plasma shown in Fig. 1.1 is obtained using $E = 2.5$ mJ. Thus, a much more dynamic picture emerges when an intense ultrashort pulse undergoes focusing in air, redistributing its energy along its propagation path. Despite attempts to simply scale the pulse energy up for long range electrical discharge and guiding, experiments to guide outdoor lightning have so far not been successful. This can be attributed to the break-up of the main laser beam into multiple filaments [10]. Above a certain energy threshold, modulation instabilities can develop easily in the laser beam causing small-scale filamentation. This results in an upper limit of the total energy that can be trapped within a filament, consequently, limiting the propagation distance of the filament.

1.4 Broad Spectral Range

Another unique property of intense femtosecond pulses propagating in air is the spectral transformation of the laser pulse into a supercontinuum. This was first reported in 1996 using 100 mJ pulses of 150 fs duration at center wavelength of 800 nm [11]. The observed supercontinuum consisted of weakly diverging conical rings surrounding a white light core while the spectrum spanned from 400 nm to 1000 nm, as shown in Fig. 1.2. The conical emission was taken at a distance of roughly 20 meters after the pulse compressor of a 5 kHz titanium:sapphire chirped-pulse regenerative amplifier that produced 2 mJ pulses with a nominal pulse duration of 40 fs and center wavelength $\lambda = 780$ nm, corresponding to a peak power $P = 50$ GW. In this setup, the beam did not pass through any lens and was allowed to freely

propagate in air.

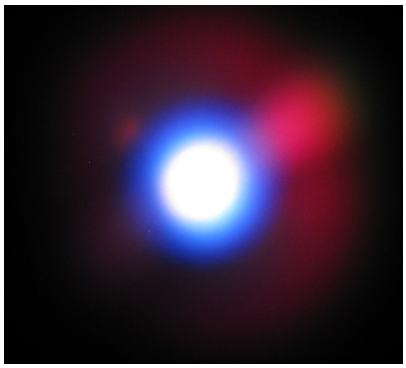

Figure 1.2: Conical emission of a filamenting laser beam propagating after 20 meters in air. (PM&AM Research, IR&D)

Depending on the initial focusing conditions, the supercontinuum that develops in the filamentation process can be *strikingly* different, as depicted in Fig. 1.3. In Fig. 1.3(a), the supercontinuum is obtained when a 25 fs, 3 mJ pulse (120 GW peak power) from a Ti:sapphire laser at 3 kHz repetition rate is focused by a f=+30 cm lens. A filament with a beam diameter of less than w_0 = 1 cm is formed in the center, surrounded by the supercontinuum, which diverges very quickly. By using much weaker focusing, this supercontinuum is transformed into white light, as seen in Fig. 1.3(b). In this geometry, the same pulse is focused down by a f=+4 m lens in air. The generated white light stays confined within the filamenting laser beam beyond the Rayleigh range of the laser beam.

1.5 Applications

Since filaments are capable of delivering high peak intensity pulses over long distances, they have been used to detect metals and biochemical agents up to distances over 90 meters [12, 13] using laser-induced breakdown spectroscopy (LIBS). The fil-

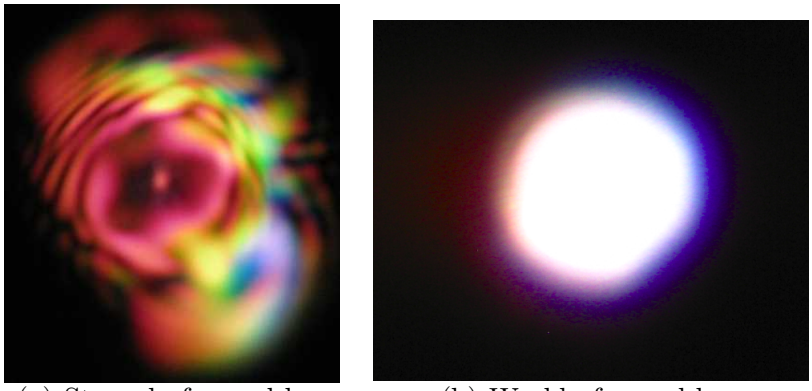

(a) Strongly focused beam (b) Weakly focused beam

Figure 1.3: Supercontinuum generated by a strongly focused and a weakly focused filamenting laser beam in air. (PM&AM Research, IR&D)

amenting laser pulses have sufficient intensity for ablation and subsequent ionization of the target material. The emission spectrum of both the ionic and atomic lines are then analzyed, primarily using a spectrometer that is connected to an intensifed charge-coupled device (ICCD) camera.

Another important application of optical filaments is in light detection and ranging (LIDAR) and atmospheric sensing. Owing to the broad spectral range of the supercontinuum, a remote source of coherent white light can be generated at a known position in the atmosphere. Measuring the absorption of the backscattered light in the return signal as a function of the white light position will yield a map of the chemical composition in the atmosphere [14, 15].

One interesting potential application of optical filaments is to trigger and guide lightning discharges because of the increased electrical conductivity in a filament. Although a lot of fundamental research has been performed to understand the plasma dynamics that occur because of filamentation [4, 8, 9, 16, 17, 18], successful and reliable triggering of outdoor lightning using femtosecond laser pulses has yet to be realized. This can be mainly attributed to the spatial beam break-up into multiple

filaments – ultimately placing an upper limit on both the electron density of the generated plasma and the length of the filaments themselves.

This dissertation describes research that has been performed by the author during the time period June, 2002 through March, 2014. Portions of this research were performed in the laboratory of Prof. Jean-Claude Diels at the University of New Mexico (from June 2002 through May 2009), and portions of this research were performed at PM&AM Research, LLC in Tucson, AZ (from June 2009 through March 2014). Some of the research has been carried out with fellow students at the University of New Mexico. Credits are appropriately given in the text and the figures. Some of the research results were directed and supported by PM&AM Research as internal research and development (IR&D), and are identified as such. Those results that are not attributed to fellow researchers are those obtained solely by the author.

The remainder of this dissertation is organized as follows. Chapter 2 begins with the description of self-action effects that occur in the filamentation of ultrashort laser pulses in air. It also reviews the main theories on the generation and propagation of optical filaments in air, and how they have been shaped by different experimental observations and theoretical modeling efforts. Chapter 3 demonstrates and highlights the importance of initial conditions prior to the formation of optical filaments in air using an aerodynamic window, and how they affect the interaction of ultrashort laser pulses with air. The effect of ionization by a filamenting laser pulse and its subsequent relaxation to ambient conditions are explored experimentally in Chapter 4. These experiments provide evidence that the thermal response of air plays a critical role in enhancing the nonlinear filamentation effects at high repetition rates. Chapter 5 concludes with the suggestion that the thermal response of air should be considered in the nonlinear index of refraction $\tilde{n}_2$ of air for a more accurate and complete description and characterization of optical filaments in air. Finally, two applications of long range optical filaments are given in the appendices: Appendix A describes the

construction of a 600-kV DC discharge system for long range laser-induced electrical discharges using filaments while Appendix B provides the theoretical and experimental framework to prolong the lifetime of the free electrons with a long pulse alexandrite laser through plasma heating and photodetachment processes.

This dissertation aims to further explore the influence of gas dynamics on the formation of ultrashort laser pulse filamentation in air in the hope that one day, filaments can be practically implemented in a wide range of applications.

Chapter 2

Understanding Filaments

2.1 Self-Action Effects in Filaments

In this section, important self-action effects observed in the propagation of femtosecond laser pulses in air will be described. Self-action effects can be attributed to the action of the laser pulse acting on itself (without any external forces or optical components) – changing its characteristics as it propagates through the medium.

To begin the discussion of light-matter interaction, the induced polarization $P(E)$ of the material due to the electric field E of the laser pulse can be represented as

$$P(E) = \epsilon_0\chi(E)E = \epsilon_0\chi^{(1)}E + \epsilon_0\chi^{(2)}E^2 + \epsilon_0\chi^{(3)}E^3 + ... + \epsilon_0\chi^{(m)}E^m \tag{2.1}$$

where χ represents the susceptibility of the material or medium. The first term in Eq. 2.1 represents the linear response of the medium, which is usually described through the linear index of refraction:

$$n_0 = \sqrt{1 + \chi^{(1)}}. \tag{2.2}$$

The second term in Eq. 2.1 is only relevant in non-centrosymmetric media. The $\chi^{(2)}$ term gives rise to sum frequency or difference generation in nonlinear crystals. An

example is the second harmonic generation of 532 nm wavelength in a potassium titanyl phosphate (KTP) crystal in a Nd:YAG laser operating at $\lambda = 1064$ nm. In amorphous or isotropic media, such as air or water, the lowest order of nonlinear susceptibility is the $\chi^{(3)}$ term. The third order polarization term can be written as [19]:

$$P^{(3)} = \epsilon_0 \chi^{(3)} \Big(\frac{3}{8} |\tilde{\mathcal{E}}|^2 \tilde{\mathcal{E}} e^{i\omega_l t} + \frac{1}{8} \tilde{\mathcal{E}}^3 e^{3i\omega_l t} \Big) + c.c. \tag{2.3}$$

Since the third harmonic generation that is associated with $\chi^{(3)}$ is weak, the second term is usually ignored. Thus, the nonlinear refractive index can be written as:

$$n_2 = \frac{3\chi^{(3)}}{8n_0}. \tag{2.4}$$

Adopting the same terminology or convention as in [19], the total index of refraction due to linear and nonlinear terms can be expressed as:

$$n = n_0 + n_2 |\tilde{\mathcal{E}}(t)|^2 = n_0 + \tilde{n}_2 I(t) \tag{2.5}$$

with $\tilde{n}_2 = 2n_2/(\epsilon_0 c n_0)$. For the discussion that follows, a tilde ($\tilde{n}$) will be used to denote the index of refraction when it is associated with the intensity of the laser pulse I:

$$n = n_0 + \tilde{n}_2 I. \tag{2.6}$$

For $\lambda = 800$ nm, $\tilde{n}_2$ for air is 3.2 x 10^{-19} cm^2/W [20] and for water is 4.1 x 10^{-16} cm^2/W [21].

2.1.1 Self-Phase Modulation

As a result of changes in the refractive index, there will be a change in the phase shift due to the intensity of a laser. For a plane wave propagating in the z-direction, the electric field can be written as:

$$E(z,t) \exp\{i(\omega_0 t - kz)\} \tag{2.7}$$

where ω_0 is the central frequency of the laser, and k is the wavenumber given by $k = \frac{n\omega_0}{c}$ with $n = n + \triangle n$ being the index of refraction of the medium. Assuming the medium responds instantaneously to the laser pulse intensity and the pulse shape is preserved after propagating through the medium, the accumulated phase is now:

$$\begin{aligned} \exp\Big\{i\Big(\omega_0 t - \frac{\omega_0 n z}{c}\Big)\Big\} &= \exp\Big\{i\Big(\underbrace{\omega_0 t - \frac{\omega_0 n_0 z}{c}}_{linear} - \underbrace{\frac{\omega_0 \triangle n z}{c}}_{nonlinear}\Big)\Big\} \\ &= \exp\Big\{i\Big(\phi_L + \phi_{NL}\Big)\Big\}. \end{aligned} \tag{2.8}$$

The change in the phase of the laser pulse due to the nonlinear refractive index will cause a change in the spectrum $\delta\omega(t)$ of the laser pulse resulting in:

$$\begin{aligned} \delta\omega(t) &= \frac{d}{dt}\phi_{NL} \\ &= \frac{d}{dt}\Big(-\frac{\omega_0 z \triangle n}{c}\Big) \\ &= \frac{-\omega_0 z}{c}\frac{d}{dt}\Big(\tilde{n}_2 I\Big) \\ &= -\frac{\tilde{n}_2 \omega_0 z}{c}\frac{dI}{dt}. \end{aligned} \tag{2.9}$$

Since the leading part of the pulse has positive slope for dI/dt, self-phase modulation (SPM) will result in the generation of longer wavelength components (red-shift), while the trailing part of the pulse will create shorter wavelength components (blue-shift) for a positive $\tilde{n}_2$.

2.1.2 Critical Power and Self-Focusing

While self-phase modulation changes the pulse propagation in the temporal domain, self-focusing is responsible for the changes in the spatial domain. From Eq. 2.6, the total index of refraction of the laser pulse propagating in the medium also depends

on the intensity of the laser pulse, I. Although it may be somewhat counter-intuitive at first sight, it is not the critical *intensity* of the laser pulse that determines when self-focusing begins but rather the critical *power*. This is because for a given power, linear diffraction is much larger for a smaller beam with a higher intensity (and larger $\tilde{n}_2 I$) than for a larger beam with a lower intensity (and smaller $\tilde{n}_2 I$). In fact, the critical power needed to overcome both linear diffraction and $\tilde{n}_2 I$ in both cases is the same.

Above this critical power P_{cr}, the laser pulse begins to self-focus, provided that the nonlinear term $\tilde{n}_2 > 0$. The self-focusing can be described as follows: In the typical Gaussian pulse, the center portion of the beam has the highest intensity and thus, has the highest index of refraction. This slows the propagation of the center portion of the pulse with respect to the outer region where the intensity of the pulse is much lower. Consequently, the beam will collapse to a singularity if there are no arresting mechanisms, such as nonlinear losses and/or plasma defocusing. This is schematically depicted in Fig. 2.1.

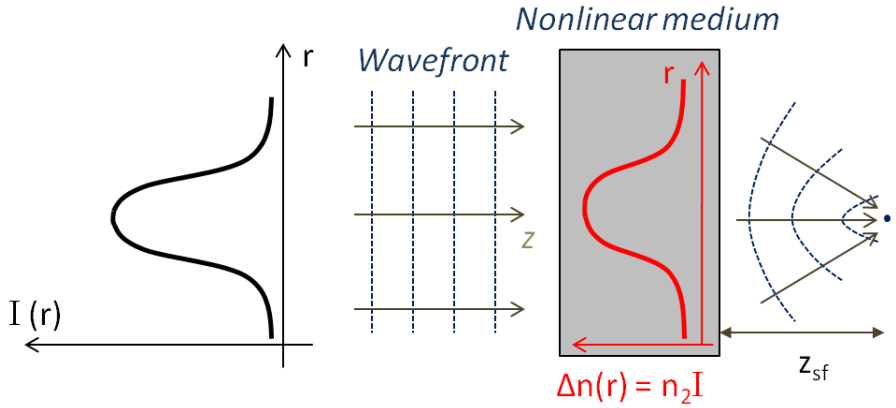

Figure 2.1: Effect of self-focusing by a nonlinear medium on the pulse wavefront without plasma defocusing or other balancing forces.

With this understanding in mind, the critical power for self-focusing can be defined as the power required to [19]:

1. Overcome the spherical wavefront curvature of a cw beam due to linear diffraction; or
2. Cancel the phase factor on-axis for a Gaussian pulse; or
3. Overcome the diffraction angle so that the beam can be trapped within a waveguide.

These definitions are given in Table 2.1 with computed values for P_{cr} with $\tilde{n}_2 = 3.2$ x 10^{-19} cm^2/W and $\lambda = 800$ nm.

Table 2.1: Definitions of Critical Power P_{cr} [19].

Critical Power	Phase On-Axis	Wavefront Curvature	Waveguide
P_{cr}	$\frac{1}{4\pi}\frac{\lambda^2}{n_0\tilde{n}_2}$ = 1.6 GW	$\frac{1}{8\pi}\frac{\lambda^2}{n_0\tilde{n}_2}$ = 0.8 GW	$\frac{(1.22)^2\pi}{32}\frac{\lambda^2}{n_0\tilde{n}_2}$ = 2.9 GW

These values for the self-focusing critical power are smaller than the more commonly accepted value given by [22]:

$$P_{cr} \equiv \frac{3.77\lambda_0^2}{8\pi n_0 \tilde{n}_2} = 3 \text{ GW}. \tag{2.10}$$

This semi-empirical relationship, obtained by simulating the long range propagation of cw beams undergoing self-focusing, provides a better approximation to the critical power P_{cr} than the general definitions in Table 2.1.

It is worth noting that the critical power P_{cr} depends on the response of the medium to the duration of the laser pulse. Up until now, the discussion has largely been restricted to the instantaneous response of the bound electrons in the medium that contribute to the total induced polarization (both linear and nonlinear), and thus to the total index of refraction $n = n_0 + \tilde{n}_2 I$. With longer pulses (typically longer than 200 fs), the medium has a longer time to interact with the laser pulses through excitation of molecular vibrations and delayed nuclear response, causing the

critical power to be reduced. In Ref. [23], the critical power dropped from 10 GW to 5 GW when the pulse duration increased from 42 fs to 200 fs.

2.1.3 Plasma Defocusing

Once the critical power is exceeded, the intensity of the femtosecond laser pulse increases due to self-focusing. In the case of solids, filamentary damage tracks may be observed along the laser path once this occurs. The damage is irreversible, caused by the optical breakdown of the material. In air, the laser pulse does not collapse to a singularity, as a result of nonlinear losses and/or ionization. For example, the generation of free electrons serves to counter the effects of self-focusing. Free electrons are generated mainly through multiphoton ionization as the pulse shrinks down in size – increasing its intensity – through self-focusing. While tunneling ionization may occur, this is a higher nonlinear process, requiring higher intensity than multiphoton ionization. For $\lambda = 800$ nm, the dominant ionization regime is multiphoton ionization for laser intensities $I \leq 10^{13}$ W/cm^2 and tunneling ionization for $I \geq 10^{14}$ W/cm^2. Regardless of the ionization mechanism for the filamentation process in air, the rate of electron generation follows [21]:

$$\frac{\partial \rho_e}{\partial t} = \sigma_K I^K (\rho_0 - \rho_e) + \frac{\sigma}{U_i} \rho_e I - r \rho_e \rho_i \tag{2.11}$$

where ρ_e and ρ_0 are the electron density and density of air molecules, respectively. The first term provides the electron generation through multiphoton ionization, where K is the number of photons needed to overcome the ionization potential U_i, and σ_K is the transition rate related to the K-photon absorption/ionization process cross section given by $\beta_K = \sigma_K \times K\hbar\omega_0\rho_0$. The critical plasma density ρ_c is given by

$$\rho_c = \frac{m_e \omega^2}{4\pi e^2} \tag{2.12}$$

where m_e and e are the electronic mass and charge, respectively. The second term represents the ionization due to inverse bremsstrahlung where its cross section σ is

given by the Drude model:

$$\sigma = \frac{k\omega_0\tau_c}{n_0^2\rho_c(1+\omega_0^2\tau_c^2)} \tag{2.13}$$

where τ_c is the collision time. In air, τ_c = 350 fs and σ = 5.1 x 10^{-20} cm^2. The last term is the loss of free electrons due to recombination where r is the recombination rate between free electrons ρ_e and the positive ions ρ_i. For short pulses (typically less than 200 fs), only the first term matters since the pulses are short enough that avalanche ionization and electron-ion recombination do not play a role or affect the propagation of the pulses.

The plasma resulting from the ionization of air by the femtosecond laser pulse serves to defocus the beam through the induced change in the index of refraction according to:

$$n = \left(1 - \frac{\rho_e}{\rho_c}\right)^{1/2} = \left(1 - \frac{\omega_p^2}{\omega^2}\right)^{1/2} \approx 1 - \frac{\omega_p^2}{2\omega^2} \tag{2.14}$$

where ρ_e is the electron density produced by the femtosecond laser pulse with plasma frequency ω_e. Thus, the change in the index of refraction due to plasma can be written as:

$$\triangle n_p = -\frac{\omega_p^2}{2\omega^2} = -\frac{e^2\rho_e}{2m_e\epsilon_0\omega^2}. \tag{2.15}$$

Because of plasma generation, the laser pulse will experience a smaller index of refraction at the center of the beam compared to the outer edge, resulting in the spatial spreading or defocusing of the beam. The change in the index of refraction will also result in the generation of higher frequencies (blue-shifting of the spectrum).

Following from Eq. 2.8, the change in spectrum resulting from plasma generation is:

$$\begin{aligned}
\delta\omega(t) &= \frac{d}{dt}\phi_{NL} \\
&= \frac{d}{dt}\Big(-\frac{\omega z \triangle n_p}{c}\Big) \\
&= -\frac{\omega z}{c}\frac{d}{dt}\Big(-\frac{e^2\rho_e}{2m_e\epsilon_0\omega^2}\Big) \\
&= \frac{e^2 z}{2m_e\epsilon_0 c\omega}\frac{d\rho_e}{dt} \\
&= \frac{e^2 z}{2m_e\epsilon_0 c\omega}\sigma_K I^K(\rho_0 - \rho_e).
\end{aligned} \tag{2.16}$$

2.1.4 Intensity Clamping

Because the plasma serves to defocus the beam, it sets an upper limit for the intensity of a laser pulse that undergoes self-focusing. In this limit, the change of the refractive index due to the Kerr effect (in Eq. 2.5) is balanced by the change of the refractive index due to plasma generation (Eq. 2.15):

$$\begin{aligned}
\tilde{n}_2 I &= \frac{e^2\rho_e}{2m_e\epsilon_0\omega^2} \\
\Rightarrow I &= \frac{e^2\rho_e}{2\tilde{n}_2 m_e\epsilon_0\omega^2}.
\end{aligned} \tag{2.17}$$

Assuming that the electron plasma density created within the filament is $\rho_e = 10^{16}$ cm^{-3} and the nonlinear refractive index $\tilde{n}_2$ is 3.2 x 10^{-19} cm^2/W, the clamped intensity is estimated to be $I = 0.89$ x 10^{13} W/cm^2, which is within an order of magnitude of the observed value of $I \approx 4$ x 10^{13} W/cm^2 [1].

For the generation of optical filaments using a spherical lens or mirror, the intensity within a filament may be higher due to the combined effects of self-focusing and external focusing. Based on the simple lens equation, the new focal position f_{new} is:

$$\frac{1}{f_{new}} = \frac{1}{f_{lens}} + \frac{1}{z_{sf}} \tag{2.18}$$

where f_{lens} is the geometrical focal length of the lens and z_{sf} is the self-focusing distance given by [22]

$$z_{sf} = \frac{0.367ka^2}{\left\{\left[\left(\frac{P}{P_{cr}}\right)^{1/2} - 0.852\right]^2 - 0.0219\right\}^{1/2}} \tag{2.19}$$

where k is the wavenumber given by $k = \frac{2\pi n}{\lambda}$, and a is the laser beam radius at $1/e^2$ of the peak intensity.

With stronger focusing, the intensity of the pulse increases and consequently, causes a larger change in $\tilde{n}_2 I$. Because of this, the plasma density must increase to prevent the collapse of the filamenting beam into a singularity based on Eq. 2.17.

2.1.5 Pulse Mode Self-Cleaning

It has been observed that the laser pulse that undergoes filamentation experiences self-mode cleaning where a circularly symmetric spatial profile emerges that corresponds to the lowest or fundamental transverse mode of a filament. Even if the initial beam profile may not be a perfect Gaussian beam, the different high order spatial features compete with each other as the pulse undergoes self-focusing and subsequent plasma defocusing. However, the lowest order spatial mode wins out and becomes the dominant mode because it has the smallest beam diameter and will be the first to self-focus and ionize the air, creating a plasma that will defocus all other higher modes along the propagation of the beam [24]. This results in the self-spatial filtering or the self-mode cleaning of the filamenting laser beam.

Fig. 2.2 shows an example of the pulse mode self-cleaning process. Although the initial spatial profile of the pulse may not be Gaussian, as seen in Fig. 2.2(a), the pulse still experiences self-focusing because its power is greater than the critical power P_{cr}. As the pulse propagates further in air, it continues to decrease in size due

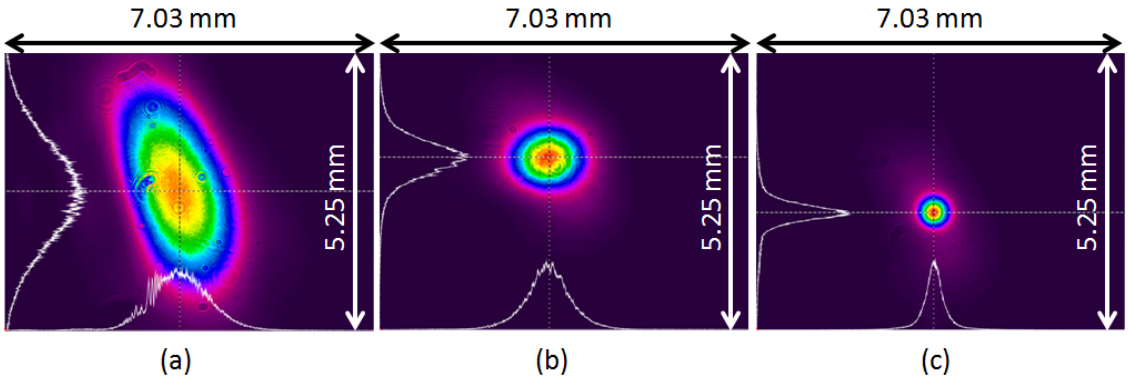

Figure 2.2: Pulse mode self-cleaning: (a) Initial profile of the beam profile undergoing self-focusing; (b) Collapse of the beam to the lowest spatial mode; and (c) Profile of the beam at the onset of filamentation in air. (PM&AM Research, IR&D)

to self-focusing, as shown in Fig. 2.2(b). The lowest spatial mode begins to dominate until the appearance of an optical filament in air, as characterized by Fig. 2.2(c). At this point, the beam size is at its minimum since plasma defocusing balances self-focusing in a filament. Any other higher modes or higher spatial frequencies will be defocused or filtered out by the generated plasma, leaving only the lowest order mode to survive within the optical filament.

2.2 Filamentation Models

Since the discovery of optical filaments in air by Braun *et al.* in 1995 [3], different models have been proposed to explain the various nonlinear phenomena associated with the formation of optical filaments in air. This section reviews some of the models that have been developed to describe the dynamic formation of filaments in air. Although various models may sufficiently capture the universal characteristics of the long range propagation of filaments in air, the different subtleties of the different models will be highlighted to accentuate some of the nonlinear interactions of

filaments with air.

2.2.1 Townes Soliton

In the absence of ionization, the diffraction of a laser beam can be overcome by self-focusing since these terms have opposing effects on the wavefront of the laser beam. If these terms strictly balance each other, the laser pulse will propagate as a spatial soliton, without experiencing any changes to its beam size as it propagates in the z-direction [25]:

$$2ik\frac{\partial E}{\partial z} = -\nabla_T^2 E - \frac{2k^2\tilde{n}_2}{n_0}|E|^2 E \tag{2.20}$$

where $E = E(x, y, z)$ represents the electric field, $k = 2\ \pi n_0/\lambda$ is the wave vector, λ is the laser wavelength, n_0 and $\tilde{n}_2$ are the linear and nonlinear refractive indices, respectively. The first term on the right hand side of Eq. 2.20 represents the diffraction of the beam with $\nabla_T^2 = \partial^2/\partial x^2 + \partial^2/\partial y^2$ the transverse Laplacian operator.

By forcing the change of the electric field E along z to be zero for a spatial soliton, the solution to Eq. 2.20 is given by

$$A(z, r) = R_\alpha(r) \times \left(\frac{n_0}{2k^2\tilde{n}_2}\right)^{1/2} \exp\left(\frac{i\alpha^2 z}{2k}\right) \tag{2.21}$$

with $r = (x^2 + y^2)$, α is a positive constant and $R_\alpha(r) = \alpha R(\alpha r)$ satisfies

$$\frac{d^2R(r)}{dr^2} + \frac{1}{r}\frac{dR(r)}{dr} - R(r) + R(r^3) = 0 \tag{2.22}$$

with boundary conditions $\frac{dR(r)}{dr}\Big|_{r=0} = 0$ and $\lim_{r\to\infty} R(r) = 0$. Mathematically, this family of solitons is known as Townes soliton. However, the solution is highly unstable, and will breakup if there is any slight imbalance between the two effects. Townes solitons have been observed in solids or liquids with nanosecond pulses.

2.2.2 Self-Guiding Model

This model was first put forth by Braun *et al.* [3] when optical filamentation in air was discovered. To explain how the femtosecond filamenting laser pulse was able to maintain its characteristically small beam diameter over long distances - beyond the Rayleigh range of the laser beam - they proposed that linear diffraction was *exactly* balanced by self-focusing and plasma defocusing. This balance could be written as:

$$\tilde{n}_2 I = \frac{\omega_p^2}{2\omega^2} + \frac{(1.22\lambda)^2}{8 n_0 \pi w_0^2} \tag{2.23}$$

where n_0 and $\tilde{n}_2$ are the linear and nonlinear refractive indices of air, λ and ω are the central laser wavelength and frequency, I the laser pulse intensity, and w_0 is the minimum spot size (diameter) of the laser. The plasma frequency ω_p is given by:

$$\omega_p = \left[\frac{e^2 \rho_e(I)}{m_e \epsilon_0} \right]^{1/2} \tag{2.24}$$

where ρ_e is the electron plasma density generated by the intense laser pulse, and ϵ_0 is the permittivity of free space. For the case of multiphoton ionization, the rate of electron generation is proportional to the laser intensity I raised to the K-th power:

$$\begin{aligned} \frac{d\rho_e}{dt} &\propto I^K \\ \Rightarrow \frac{d\rho_e}{dt} &= \sigma_K I^K \end{aligned} \tag{2.25}$$

where K is the number of photons required to overcome the ionization potential of a gas molecule, and σ_K, the proportionality constant that represents the K-photon ionization cross section.

The self-guiding model is different from the Townes soliton because it includes ionization effects (the generation of plasma that serves to defocus the beam) for filament formation in air. This model represents a *quasi* steady-state response of air molecules due to propagation of intense femtosecond laser pulses in air.

2.2.3 Moving Focus Model

In a dispersionless medium, a propagating laser pulse can be viewed as a series of transverse slices with their own peak powers independent of each other. In this case, the propagation of the individual slices can be treated as a continuous wave Gaussian beam. This assumption is valid if space-coupling effects, such as group velocity dispersion (GVD), are weak and can be neglected [20]. For a typical $\tau_0 = 100$ fs pulse with central wavelength of $\lambda = 800$ nm, the characteristic dispersion length L_d is calculated to be 167 m according to [19]:

$$L_d = \frac{\tau_0^2}{2|k''|} \tag{2.26}$$

where the group velocity dispersion of air at $\lambda = 800$ nm is given by $k'' = 30$ fs^2/m. This characteristic dispersion length L_d is much longer than the distances observed in the laboratory, where typical distances are limited to less than 20 meters.

Fig. 2.3 depicts the temporal slicing of a femtosecond pulse in the moving focus model. In the leading portion of the pulse, the peak power P of the slice is less than the critical power P_{cr} for self-focusing, resulting in the linear diffraction beam slice. The next slice of the pulse is above the critical power, and experiences a nonlinear self-focus distance z_{sf} given by Eq. 2.19, according to Marburger's formula [22, 26]. Since the next slice contains the central portion of the pulse, and has the highest peak power, the self-focusing distance is the shortest compared to all the time slices. Although the subsequent slice has a peak power less than the central slice, its peak power is still above the critical power P_{cr}, leading to a self-focusing position farther from the central focus. However, this slice will also experience a change in the refractive index caused by the earlier time slices, resulting in a slight shift in the position of its self-focusing distance z_{sf}, compared to the earlier time slice with the same peak power. Finally, the last time slice of the pulse has a peak power less than the critical power and will experience linear diffraction and increase

in beam diameter. Thus, the longitudinal self-focusing of the individual time slices of the intense laser pulse creates an illusion of a continuous waveguide or plasma channel that persists over many Rayleigh lengths in air.

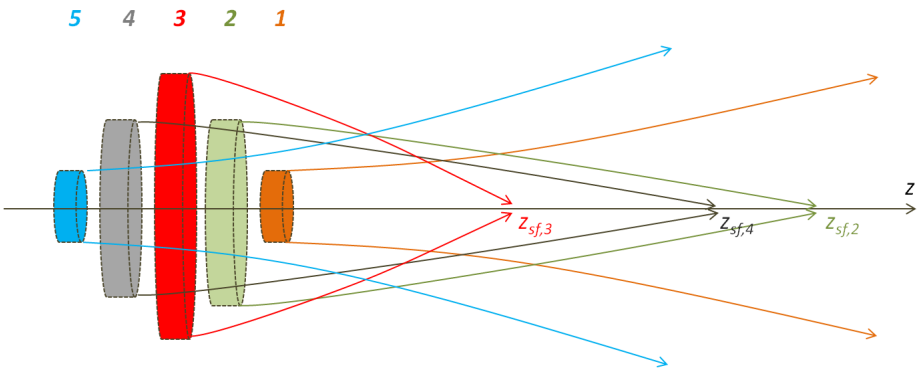

Figure 2.3: Moving focus model. (Adapted from [19].)

It is worth noting that the above scenario does not mention any saturation mechanism or plasma generation. If, for example, free electrons are generated through photoionization of air by the intense laser pulse, the later time slices will experience different propagation conditions (such as reduced refractive index) compared to the earlier time slices. This will not only change the self-focusing distances of the later time slices, but also change in the diffraction pattern that will show up in the transverse dimension due to the longitudinal changes created by the earlier time slices. This may be seen in the far-field of the filament. The temporally asymmetric focusing behavior of the individual time slices has been used to explain a host of obsverations, such as X-wave generation and conical emission [24].

2.2.4 Dynamic Spatial Replenishment Model

Although the discovery of optical filamentation in air prompted many experimentalists to explore and understand the formation and properties of filaments in air leading

to numerous experimental papers, computational physicists were equally excited by these new results. In 1998, the dynamic spatial replenishment model was proposed [27]. In the dynamic spatial replenishment model, as the intense laser pulse begins to filament in air, the leading edge increases in intensity due to self-focusing and thereby generates a plasma, which not only arrests the self-focusing, but also serves to defocus the beam. As a result of energy losses due to ionization and other nonlinear effects (such as rotational Raman scattering), the intensity of the trailing edge of the pulse is reduced, and the pulse energy is transferred into the spatial ring surrounding the leading peak, as depicted in Fig. 2.4. However, upon further propagation, the trailing edge begins to form as a peak due to replenishment from the energy reservoir due to self-focusing. This dynamic pulse evolution of focusing, defocusing and subsequent refocusing can repeat itself a few times, creating a channel that persists over many Rayleigh lengths in air. The dynamic spatial replenishment model incorporated the temporal dynamics that were missing in prior models, and demonstrated how rotational Raman scattering and other delayed nonlinear responses may affect the propagation of ultrashort laser pulses in air.

2.2.5 Conical Wave Model

The conical wave model was first proposed after observing that conical emission may be attributed to multiple pulse splitting in the filamentation process in water [28, 29]. Instead of relying *solely* on an energy reservoir surrounding the hot center core of the beam for the regeneration of the filament, pulse splitting plays a role in feeding the central core after the initial filament has faded. The daughter pulses created from the first pulse splitting generate dynamic X waves (wavepackets that exhibit an X shape in the both the near and far fields). The formation of X waves can be seen as an "attractor" for the development of z-invariant waves.

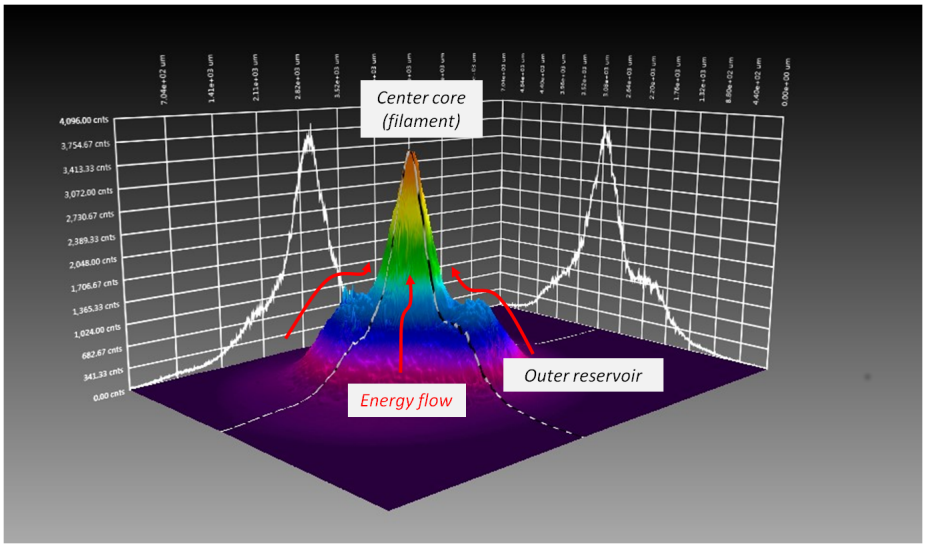

Figure 2.4: Dynamic spatial replenishment model: The outer reservoir continuously replenishes the energy loss in the filament core due to multiphoton ionization and nonlinear losses. (PM&AM Research, IR&D)

The formation of a conical wave can also be viewed as a spontaneous reshaping from an initial Gaussian beam due to non-negligible nonlinear losses [30]. These nonlinear losses, such as multiphoton excitation, serve to flatten the intensity profile of a Gaussian beam, creating a flat top beam profile. Due to self-focusing, energy is transferred from the outside into the center core, creating a Bessel beam with formation of a filament at its center. As the beam propagates, the filament energy is replenished from the photon bath or energy reservoir, yielding the conical emission. This pulse evolution is seen to be driven by the requirement to achieve a condition for minimum nonlinear losses and maximum robustness (against diffraction and dispersion effects) for long range propagating, z-invariant waves.

A comprehensive numerical investigation was performed to explore the significance of various events that arrest the collapse of a self-focusing beam [21]. By ignoring plasma defocusing, simulation results demonstrated multiple pulse splitting and confirmed the formation of X-waves in the filamentation experiments using

water as the Kerr medium. The inclusion of plasma defocusing produced interference fringes in the far-field spectrum with the spectrum becoming more asymmetric though the overall structure of the X-wave remained roughly the same. From this numerical simulation, an overall picture emerges: The formation and regeneration of an optical filament at the center of the beam is being continuously fed by the outer/extended reservoir due to self-focusing. The center core contains a fraction of the total energy of the pulse, and its energy is dissipated by nonlinear losses. The outer part of the beam has much lower intensity than the center core, and thus, dispersion and diffraction are the dominant players responsible for the spectral features observed in the near- and far-fields of the generated X-waves.

2.2.6 Current Understanding

At present, the general consensus is that optical filaments are formed based on the *dynamic* balance between linear diffraction, nonlinear self-focusing, plasma defocusing and other nonlinear losses, such as multiphoton absorption and Raman scattering. The low-intensity energy reservoir that surrounds the filament core serves not only to provide energy for the dynamic replenishment of the filament, allowing it to reform a few times, but it can also lead to the generation of X-waves. Since the central core of the filament has a broader spectrum, it propagates with a different group velocity than the outer reservoir. Spectral components in the filament core can generate new spectral components with the pump pulse in the reservoir through four-wave mixing, leading to the formation of conical rings surrounding the white central core observed in the far-field. However, the initial conditions of the pulse undergoing filamentation play an important role in determining the observed traits of the optical filament. For example, the generation of conical emission surrounding a white (or spectrally broad) central core of a filament is typically observed in free propagation (i.e., without external focusing) of short intense pulses in air because of the longer interaction

region over which four-wave mixing and self-spatial filtering can take place. With external focusing by either a spherical lens or mirror, this interaction region is much smaller, and no conical rings are observed with the filament. External focusing also limits various self-action effects that occur within a filament, often limiting the robust propagation of the filament over extended distances in air. Nonetheless, the dynamic competition between linear diffraction, nonlinear self-focusing, plasma defocusing and nonlinear losses are still present regardless of the initial focusing or preparation of the filament in air.

Chapter 3

Formation of Optical Filaments in Air

Although optical filaments can now be routinely generated in air using sub–100 fs laser pulses with a few millijoules of energy, their creation is highly nonlinear and depends on the dynamic balance between diffraction, self-focusing, plasma defocusing and nonlinear losses. The complexity of the interaction of various competing forces in the formation of filaments has even led to the suggestion of including higher order Kerr effects [31, 32]. Computational modeling may not be able to conclusively resolve whether higher order Kerr effects are essential to the formation of optical filaments since almost all models require the accurate measurement of various parameters, such as the nonlinear index of refraction $\tilde{n}_2$ and the multiphoton ionization cross section σ_K. Consequently, theoretical models generally provide a qualitative understanding of the formation of filaments in air, and the relative importance of the different nonlinear phenomena that can occur in the filamentation process. This can simply be achieved by "turning on/off" the different nonlinear terms in the simulation, and then comparing the results. Oftentimes, certain experimental parameters are slightly adjusted in the simulations to obtain results that are consistent with the experiments,

or when experimental parameters are not readily available for a particular simulation run. While the adjustment and/or switching on and off of various nonlinear terms can be done with relative ease through computational modeling, it is much more difficult to achieve ideal conditions so that the formation of filaments can be investigated experimentally. The problem is further compounded by the fact that the power and intensity associated with the laser pulse are sufficiently high that optical damage will occur, and thus, ruling out the implementation of direct measurements using conventional optical lenses, mirrors and detectors.

This chapter is devoted to the experimental investigation of the formation of filaments in air using an aerodynamic window. This aerodynamic window can also be used as a diagnostic tool to study the characteristics of optical filaments as they propagate in air.

3.1 Aerodynamic Window: An Ideal Tool for Experimentalists

To obtain a quantitative analysis of the formation of an optical filament in air, it is highly desirable to accurately capture the interaction of the intense femtosecond laser pulse with air. For example, increasing the air density will invariably increase the nonlinear refractive index of air $\tilde{n}_2$. Conversely, by reducing the air density to vacuum, the Kerr self-focusing disappears as $\tilde{n}_2$ vanishes along with the air. Thus, the formation and propagation of optical filaments in air under different atmospheric conditions can be investigated. However, isolating the region of interaction between the optical filament and modified air can be daunting and expensive due to the high peak intensity in a filament. As discussed in the previous chapter, the intensity inside a filament is clamped to $I \approx 4 \text{ x } 10^{13}$ W/cm^2, and is sufficiently high to damage any

optical elements, such as optical windows. (The optical breakdown threshold for fused silica is $I \approx 10^{12}$ W/cm^2, and for metals $I \approx 10^{11}$ W/cm^2 [33].) Consequently, to perform measurements in which an optical filament crosses into or out of a sealed pressure chamber, one will only be able to do single-shot experiments – replacing the entrance and/or exit windows after each laser shot.

To overcome this labor intensive and costly technique, we proposed and implemented a novel solution using an aerodynamic window [34, 35, 36]. Instead of using fused silica as an optical window, the pressure difference between ambient atmosphere and vacuum can be maintained by centrifugal forces induced by the curvature of a supersonic gas jet in the aerodynamic window [37]. Since the medium of the window is essentially air, the window is not susceptible to any optical damage caused by the high intensity of the filament. Furthermore, air has a much smaller nonlinear index of refraction $\tilde{n}_2 = 3.2$ x 10^{-19} cm^2/W compared to $\tilde{n}_2 = 3.5$ x 10^{-16} cm^2/W for fused silica at $\lambda = 800$ nm [38], resulting in a much smaller effect of the filament crossing an aerodynamic window.

Utilizing these advantages afforded by the aerodynamic window, two different experimental setups can be envisioned to measure the effects of atmospheric conditions on the formation and propagation of optical filaments. In the first setup, as illustrated in Fig. 3.1, an optical filament is formed by weakly focusing an intense femtosecond laser pulse in vacuum. Because it is in near-vacuum, there is no measurable self-focusing nor plasma generation associated with the *preparation* of the filament. Thus, the onset of filamentation in the air can be controlled to occur precisely at *Window 2*, which is the boundary between vacuum and ambient air. Upon exiting the vacuum chamber into ambient-pressure air, the intense laser pulse is expected to spontaneously form an optical filament due to the dynamic balance between self-focusing, plasma defocusing and other competing effects. The distance between *Window 2* and the positive lens is the geometrical focus of the lens $z = f$.

Because the intensity of the filamenting laser pulse is expected to be the highest at *Window 2*, the aerodynamic window is placed here. Conversely, since the beam entering the vacuum chamber has not focused down to sufficiently high intensity, *Window 1* can be a fused silica. To avoid any optical damage, the vacuum chamber should be sufficiently long that the laser intensity I at *Window 1* is adequately low to ignore any Kerr effects due to $\tilde{n}_2 I$.

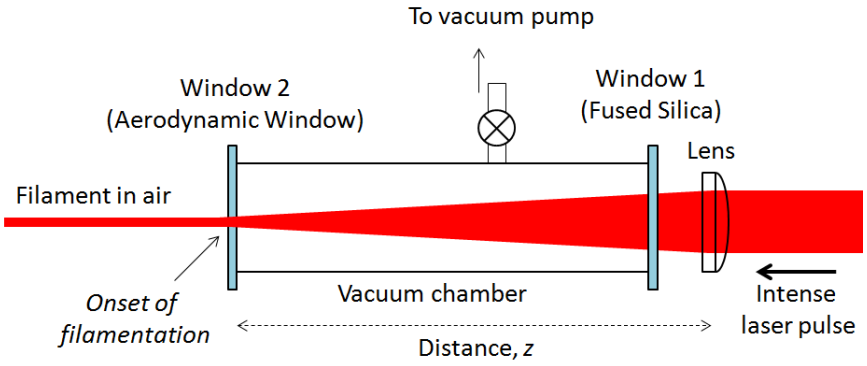

Figure 3.1: Preparation of an optical filament in a vacuum chamber.

The second experimental setup, as schematically depicted in Fig. 3.2, allows us to perform optical diagnostics on the optical filament. When the optical filament enters the low-pressure chamber via the aerodynamic window, the dynamic balancing of the various nonlinear effects disappears. Consequently, the filament diffracts *linearly* in vacuum. After propagating a distance z, the beam size is sufficiently large so that the pulse intensity will not cause any damage or induce any nonlinearities due to $\tilde{n}_2$. This will allow us to perform direct optical diagnostics (such as beam profile, pulse energy and spectral measurements) on the diffracted beam. Assuming that the filament has a Gaussian beam profile, and is terminated at $z = 0$, the filament beam size w_{fil} at $z = 0$ can be inferred by simply measuring the beam size $w(z)$ at the detector:

$$w_{fil} = \frac{w(z)}{\sqrt{1 + (\frac{z}{z_R})^2}} \tag{3.1}$$

where z_R is the Rayleigh range defined by $z_R = \frac{\pi w_0^2}{\lambda}$ where λ is the laser wavelength and w_0 is the minimum spot size, which in this case, is the same as the beam size of the filament w_{fil}.

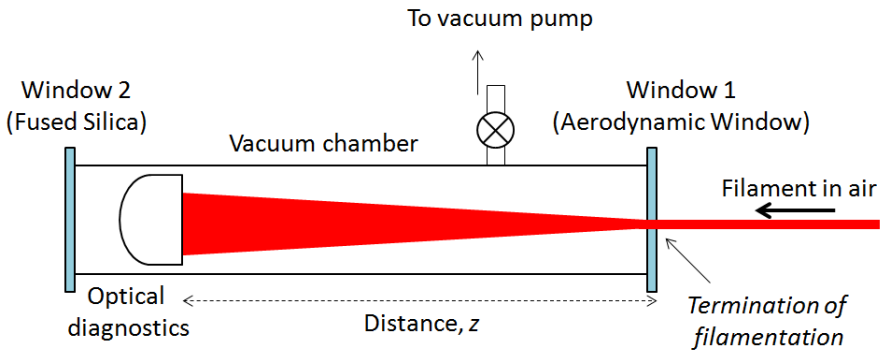

Figure 3.2: Measuring the beam size and spectrum upon the termination of an optical filament in vacuum.

3.1.1 Aerodynamic Window: Design and Test

For the work presented here, the aerodynamic window was suggested by Kevin Kremeyer, designed by H. Wilhem Behrens at TRW, and was constructed by Team Specialty Products (TSP) in Albuquerque, NM. Further details of the design can be found in [34]. Based on the simulation of the design, the pressure on one side of the aerodynamic window can be kept at a pressure close to vacuum, as shown in Fig. 3.3.

Fig. 3.4 shows the pressure obtained inside the vacuum chamber at the different air pressures at the 4.2-mm inlet of the aerodynamic window using a different number of roughing pumps to pump down pressure chamber. Even without any roughing pump to evacuate the vacuum chamber, the pressure is reduced to about 85 Torr. Using up to three roughing pumps, the pressure in the vacuum chamber can be further lowered to about 5 Torr. The optimal air pressure at the inlet to achieve the lowest pressure in the vacuum chamber is about 5 Torr.

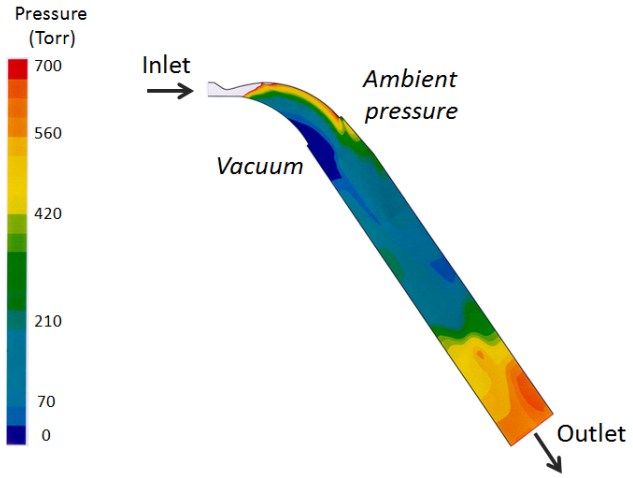

Figure 3.3: Simulation result of the pressure profile in an aerodynamic window [34].

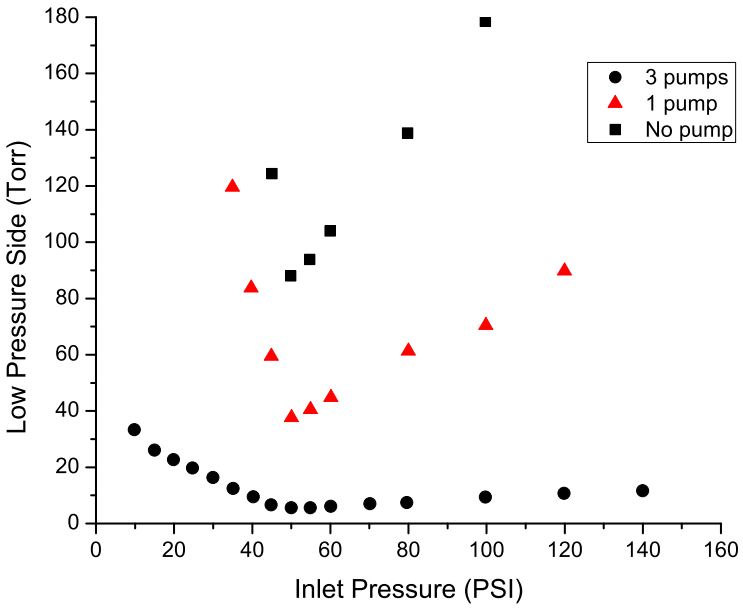

Figure 3.4: Test results of the pressure maintained by an aerodynamic window in the laboratory [35].

3.2 Femtosecond Laser System at UNM

In the experimental results presented here, the femtosecond laser system is a home-built titanium:sapphire (Ti:S) chirped-pulse amplifier (CPA) system. Fig. 3.5 shows the block diagram of this laser amplifier system. At the heart of the laser is a Kerr-lens mode-locked (KLM) oscillator. This oscillator produces a pulse train of 94 MHz with a nominal pulse duration of 80-90 fs, at central wavelength $\lambda = 775$ nm. The output power from the mode-locked oscillator is typically 200-400 mW, and thus, the pulse energy is roughly 2-4 nJ.

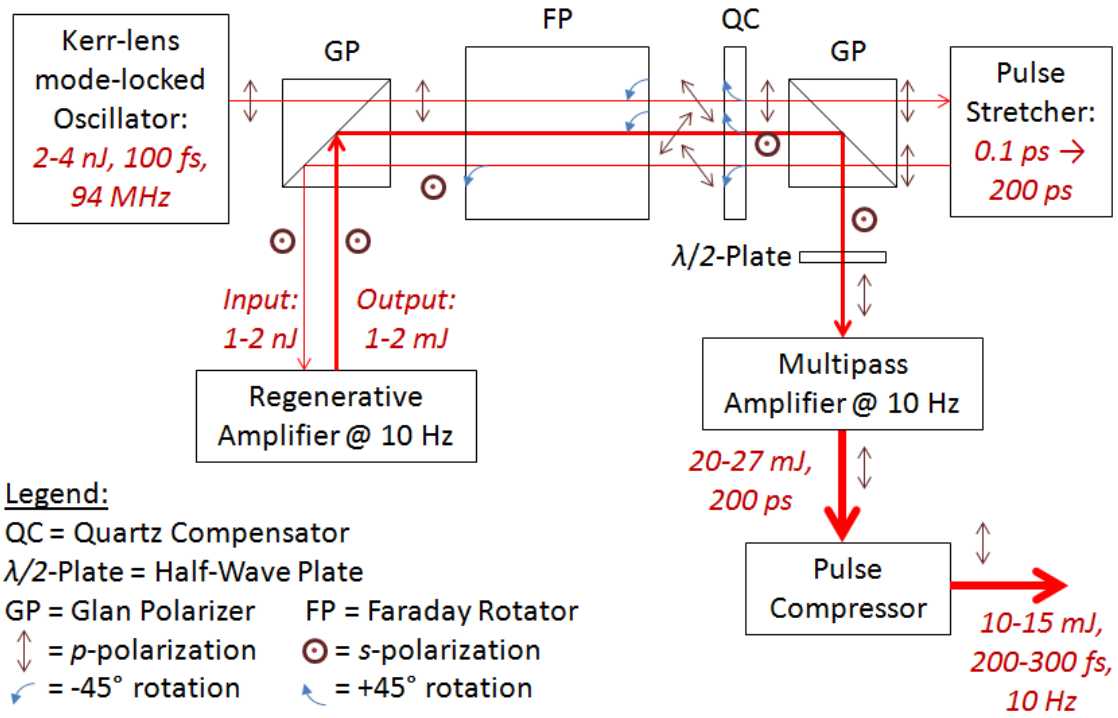

Figure 3.5: Block diagram showing the various sub-systems of the femtosecond Ti:S laser.

The pulse train from the oscillator is then sent to a pulse stretcher, stretching the pulses from ∼100 fs to ∼200 ps by imparting a positive chirp where the longer wavelength components arrive earlier in time compared to the shorter wavelength

components. The pulses need to be stretched in time to safely amplify these pulses in the regenerative amplifier and multipass amplifier stages. (Increasing the pulse duration will result in the lowering of the pulse intensity). An optical isolator is placed between the oscillator and the pulse stretcher to prevent any laser feedback into the oscillator. It consists of a Faraday rotator and a quartz compensator, sandwiched between two Glan polarizers. The quartz compensator rotates the polarization in the opposite direction of the Faraday rotator so that the net polarization of the laser pulse after passing through both the Faraday rotator and the quartz compensator is zero going from left to right, but experiences 90 ° rotation in the opposite direction.

The stretched pulses are then sent into a regenerative amplifier where the pulse energy is increased from ∼1-2 nJ (after losses in stretcher) to 1-2 mJ. The regenerative amplifier consists of a thin film polarizer and a Pockels cell that collectively perform pulse picking – selecting a 10-Hz pulse train (from the initial 94-MHz pulse train) to be amplified in the cavity of the regenerative amplifier. The pulse makes about 27-30 round trips within the regenerative cavity before it is switched out by the Pockels cell.

After emerging from the regenerative amplifier cavity, the amplified pulse passes through the Faraday rotator again and is then redirected to a three-pass amplifier stage, where the energy is further increased from 1-2 mJ to ∼25 mJ. The Ti:S crystal in the multipass amplifier is pumped on both sides by a frequency-doubled Q-switched Nd:YAG laser, where the pump beam is relay imaged from the output of the second harmonic crystal in the Nd:YAG laser onto the Ti:S crystal for mode-matching and to achieve the best beam profile.

To obtain transform-limited pulses with the highest power, the amplified pulses are directed to a pulse compressor, consisting of a double-passed parallel grating pair. This pulse compressor introduces a negative chirp to compensate for the positive chirp imparted by the pulse stretcher. By adjusting the separation of the grating

pair in the compressor, the linear chirp (and thus, the output pulse width) can be adjusted to obtain the shortest pulse duration after the amplifier stages. Due to higher order dispersion terms that are introduced by transmissive optics in the regenerative cavity that cannot be compensated by the compressor grating pair, the final pulse is always longer than the pulse coming out of the KLM oscillator. The output pulse from this laser amplifier system is typically 200-300 fs with a nominal pulse energy of 10-15 mJ, at a repetition rate of 10 Hz, and having a p-polarization. A more detailed description of the laser can be found in [36, 39].

3.3 Experimental Setup

Fig. 3.6 shows the schematic of the experimental setup to investigate the preparatory phase of an optical filament in air and/or vacuum. The output laser beam from the CPA laser system is loosely focused by a plano-convex fused silica lens with a focal length of $f = +3$ meters. The pulse duration is nominally 250 fs with a pulse energy of 9 mJ, having a beam diameter D of 8 mm (at $1/e^2$) and a central wavelength $\lambda =$ 780 nm. Thus, the minimum beam diameter is $d_0 \approx \frac{4f\lambda}{\pi D} = 372$ μm (or minimum spot size $w_0 = d_0/2 = 186$ μm) by assuming a Gaussian beam profile. The minimum spot size is comparable to the accepted beam size values of filaments, which range from 100 μm to 1 mm. Thus, the experimental setup will allow us to obtain conditions that are favorable for the creation of optical filaments in air. The nonimal peak power for the pulse is 36 GW, which is over 10 times larger than the critical power $P_{cr} = \frac{3.77\lambda^2}{8\pi n_0 \tilde{n}_2} = 2.8$ GW.

Because of the pressure dependence of the nonlinear index of refraction $\tilde{n}_2$, the onset of filamentation changes when the pressure in the vacuum chamber is varied from ambient conditions to 8 Torr, at which no nonlinear effects can be observed. The position of the $f = +3$-m lens is then adjusted so that the geometrical focus lies at

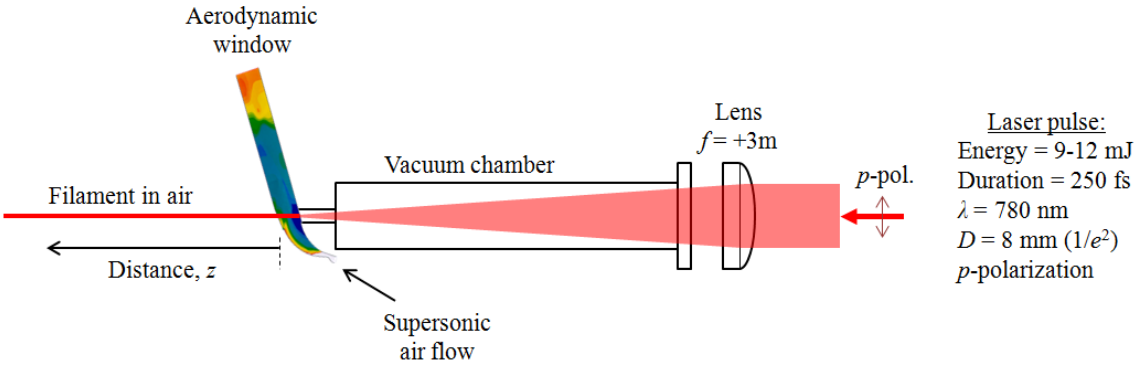

Figure 3.6: Schematic of experimental setup to investigate the formation of filaments in air.

the exit of the aerodynamic window. Due to tenuous formation of an optical filament in air as a result of a dynamic balance between self-focusing and plasma defocusing, it is extremely difficult to pinpoint precisely the start of the filamentation process. For this reason, the geometrical focus will be used as a reference position in our experiments.

3.3.1 Prior Work

Due to the physical constraints on our laboratory space, a grazing incidence mirror (GIM) was used instead of having a second aerodynamic window to terminate the filamentation process (as suggested in Fig. 3.2) so that the filament profile and spectrum could be measured directly at a known distance z. This grazing incidence mirror was coated for a 99.9999% reflectivity for 89 ° for s-polarized light at λ = 1064 nm. When this mirror was used for p-polarized laser wavelength $\lambda = 780$ nm, only 0.3% of the laser pulse was transmitted through the mirror at an incident angle $\theta = 89\,^\circ$ [36]. The transmitted laser pulse intensity was sufficiently low that no nonlinearities were accumulated in transmission. The setup is sketched in Fig. 3.7. The optical detector was either a beam profiler to measure the beam size of a filament,

or a spectrometer to measure the spectral components of a filament.

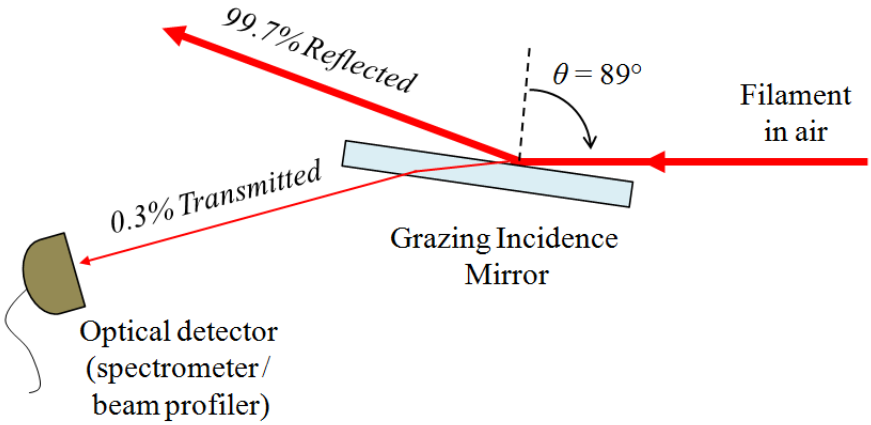

Figure 3.7: Grazing incidence mirror for the direct measurement of optical filament characteristics. (Adapted from [36].)

Using this setup, the beam size of a filament that was launched in air and also in vacuum has been documented in [36]. For an optical filament launched (or prepared) in vacuum, the beam size w remained fairly constant and was less than 225 μm over a propagation distance from z = 20 cm to z = 70 cm, as shown in Fig. 3.8 [40]. In contrast, the beam size of a filament that was prepared in air increased linearly from w = 200 μm (at z = 0 cm) to w = 375 μm (at z = 70 cm), which was still a smaller increase compared to the linear diffraction of a Gaussian beam.

The spectral measurement of the filaments prepared in air and in vacuum also yielded different results, as shown in Fig. 3.9. These spectra were taken at a distance z = 12 cm away from the geometrical focus. When the filament is launched in air (with the aerodynamic window turned off), the effects of the nonlinear index of refraction $\tilde{n}_2$ of air can be seen in Fig. 3.9(a) where self-phase modulation causes the broadening towards the longer wavelength components, or is red-shifted. Furthermore, self-focusing also occurs due to $\tilde{n}_2$, which increases the pulse intensity and leads to earlier plasma generation. As a result, the filament spectrum also experiences a stronger

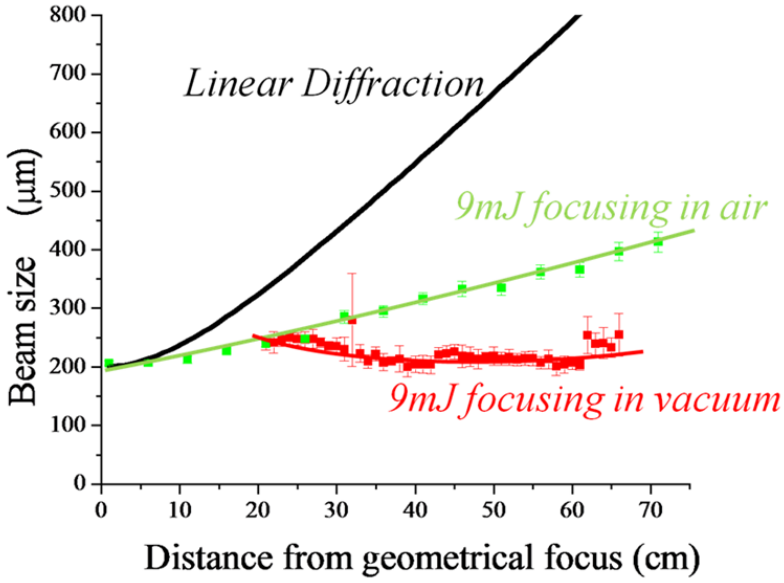

Figure 3.8: Variation of filament beam size along the propagation distance z for both cases of vacuum and air preparation using 9-mJ pulses [36, 40].

blue-shift (increasing its intensity towards the shorter wavelength components) as seen in Fig. 3.9(b). The overall spectral intensity is noticeably higher in Fig. 3.9(a) for the filament that is prepared in vacuum because less energy is lost in the absence of $\tilde{n}_2$ and the concomitant plasma generation in vacuum.

After propagating to $z = 82$ cm, the redder components of the filament spectrum have increased in both cases when the filament is prepared in air and in vacuum, as seen in Fig. 3.10. However, the spectrum of the filament prepared in air remains more blue-shifted than that of the filament prepared in vacuum.

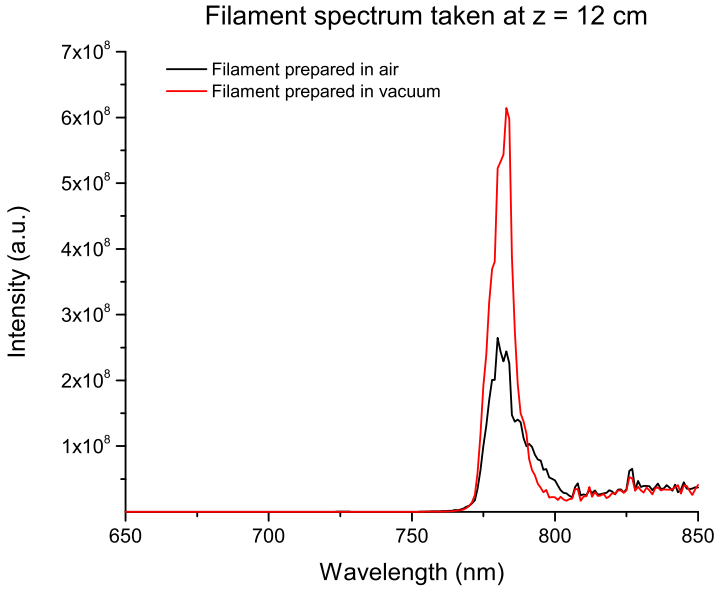

(a) Spectral intensity (linear scale)

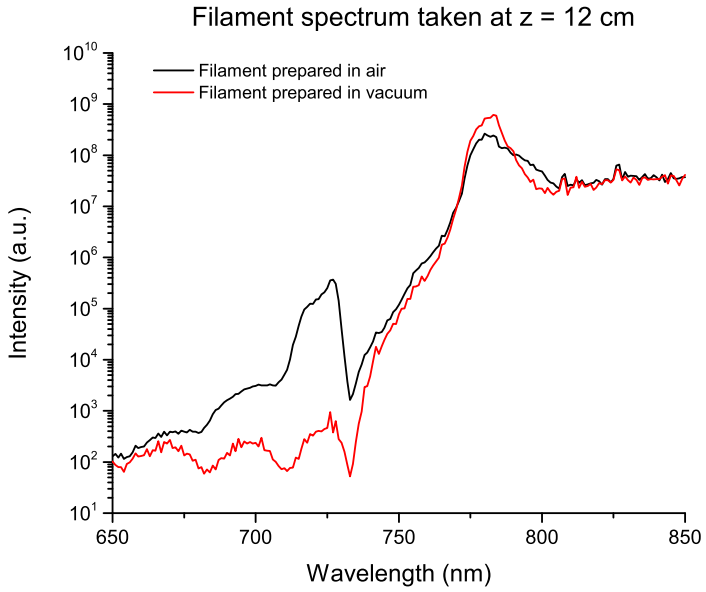

(b) Spectral intensity (logarithmic scale)

Figure 3.9: Filament spectrum taken at $z = 12$ cm when launched in air and in vacuum on a: (a) linear scale; and (b) logarithmic scale. (Adapated from [36].)

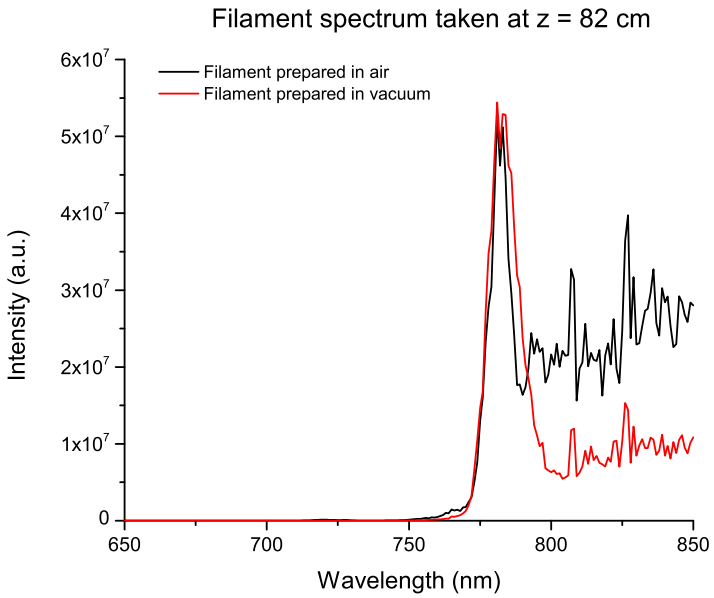

(a) Spectral intensity (linear scale)

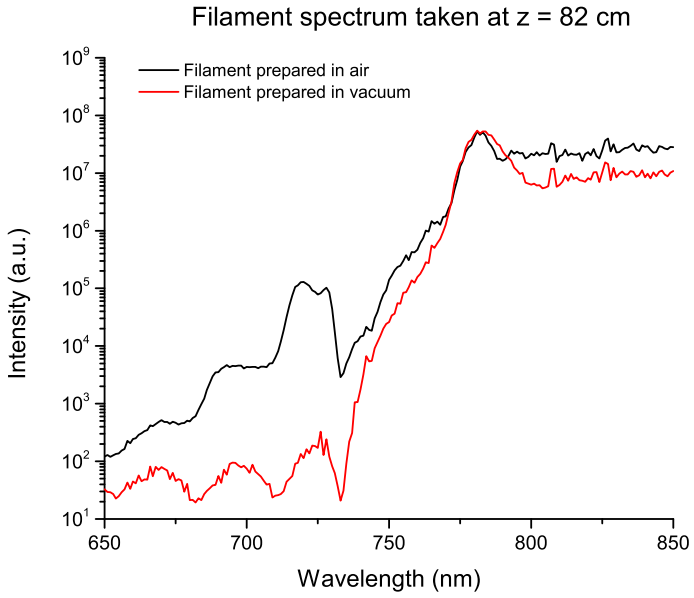

(b) Spectral intensity (logarithmic scale)

Figure 3.10: Filament spectrum taken at $z = 82$ cm when launched in air and in vacuum on a: (a) linear scale; and (b) logarithmic scale. (Adapted from [36].)

3.3.2 Ionization of Air by Optical Filaments

To explore the ionization and plasma dynamics in greater detail for both cases of filaments prepared in air and in vacuum, the experimental apparatus, as sketched in Fig. 3.11, was prepared. The electrode pair was made of copper and had a center bore that allowed the filaments to pass through without ablating the copper electrodes. An electric potential of 4 kV was applied across the two electrodes while the gap between them was kept at $d = 2$ cm. The electrode pair was mounted on a rail, and was scanned along the z propagation of the filament. Because of multiphoton ionization, the optical filament generated an electric current i that flowed between the pair of electrodes, and thus, completed the electrical circuit. This current induced a voltage drop across the 22-Ω load resistor. A fast oscilloscope was then used to measure the induced voltage generated by the ionization current in a filament. The strength of the induced voltage was indicative of the degree of ionization occuring within a filament – the higher the measured induced voltage was, the stronger the ionization was, as more electrons were generated that contributed to the electrical conductivity of the optical filament in air.

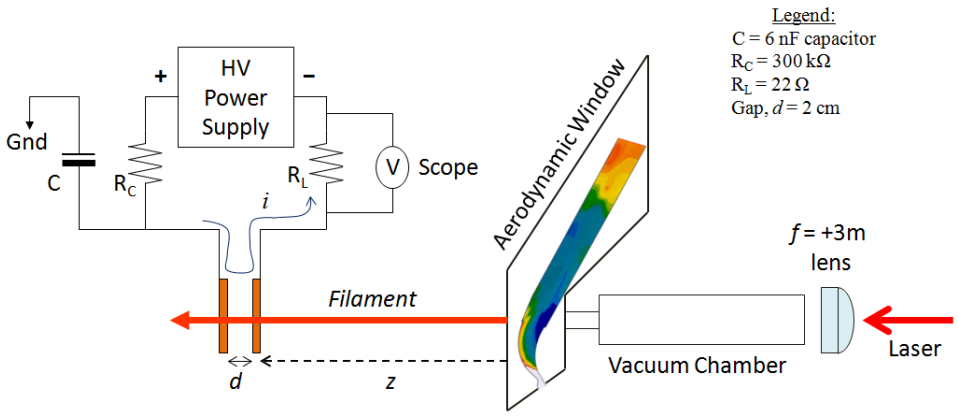

Figure 3.11: Experimental setup to measure the relative ionization by an optical filament along its propagation path z. (Adapted from [40].)

This setup was similar to the technique used by Tzortzakis *et al.* where the electron density within a filament channel was estimated to be 3 x 10^{16} cm^{-3} [41]. In our experiments, we were interested in the changes in the relative degree of ionization along the filament channel to determine the dependence of the spectral broadening on the plasma generated within the filament.

Fig. 3.12 shows the experimental results for the relative ionization in a filament that was prepared in air and in vacuum. (We have published these results in [40].) For both cases, the linear decrease in the induced voltage as the filament propagated away shows that the pulse energy was depleted because of losses due to the ionization of air molecules. Nonetheless, the magnitude of the slope of the induced voltage versus distance z in the case of a filament prepared in air was almost 18% larger (or steeper) than that of a filament prepared in vacuum. This seems to suggest that the filament that was initially formed in air experienced a faster rate of energy loss due to plasma generation compared to the filament that is formed in vacuum.

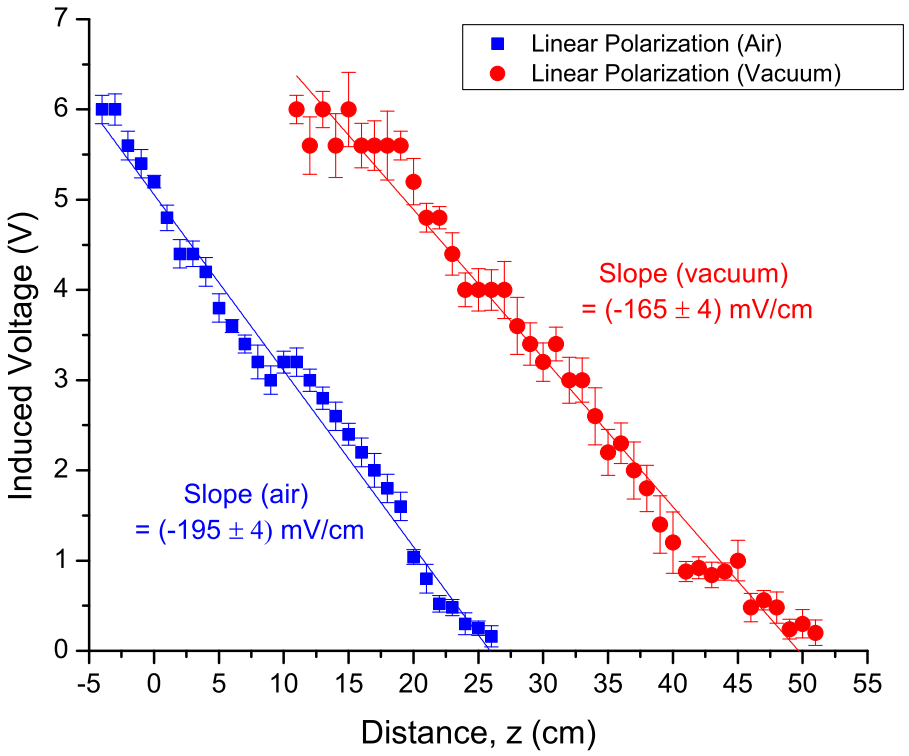

Figure 3.12: Induced voltage as a measure of relative ionization by an optical filament along its propagation path z, with the geometrical focus of the lens at $z = 0$ where it is defined as at the exit of the aerodynamic window. (We have previously reported this result in [40].)

To simply test whether more electrons were generated in the filament that was prepared in air, we investigated the variation of the electrical breakdown threshold of air along the filament propagation. The experimental setup was identical to that shown in Fig. 3.11 except that the gap was reduced to $d = 1$ cm. The voltage across the electrode pair was slowly increased until air breakdown was observed. For Albuquerque, which is mile-high, we observed the electrical breakdown threshold to be about 21 kV/cm in the laboratory. The electrical breakdown threshold induced by the optical filament was then plotted versus propagation distance z from the

aerodynamic window, as shown in Fig. 3.13. In the case of the optical filament prepared in vacuum, a plateau was observed between $z = 11.8$ cm and $z = 21.8$ cm, where the measured breakdown electric field was 13 kV/cm. Beyond $z = 22$ cm, the breakdown electric field increased linearly at a rate of 0.233 kV/cm^2, which was a smaller increase compared to 0.382 kV/cm^2 for the filament prepared in air. Based on these results, we can conclude that there were more electrons generated in the filament that was initially prepared in vacuum to compensate for a stronger self-focusing stemming from a larger change in the refractive index ($\triangle n = \tilde{n}_2 I$) because of the higher peak intensity that resulted from a smaller filament beam diameter, as reported in [36].

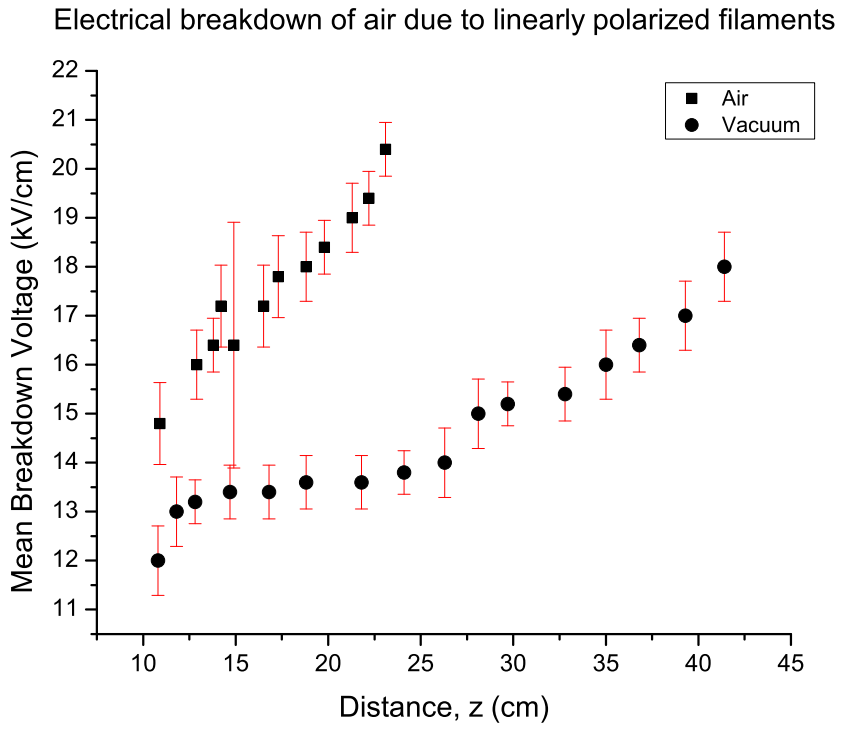

Figure 3.13: Variation in the breakdown voltage caused by an optical filament along its propagation path z.

3.3.3 Nitrogen Fluorescence

In addition to the ionization technique, nitrogen fluorescence has been used to characterize the length of an optical filament in air [42, 43]. The fluorescence of nitrogen typically lies in the ultraviolet region, and comes mainly from the first negative band system ($B^2\Sigma_u^+ \rightarrow X^2\Sigma_g^+$ transition at $\lambda = 391$ nm) for N_2^+ and the second positive band system ($C^3\Pi_u \rightarrow B^3\Pi_g$ transition at $\lambda = 337$ nm) for N_2. In a filament, multiphoton ionization of nitrogen by an intense laser pulse gives rise to the creation of a free electron and positive nitrogen ion N_2^+. This ion combines quickly with a neutral molecule to produce N_4^+, which recombines with the free electron to generate an excited $N_2(C^3\Pi_u)$ and a ground N_2. Subsequent relaxation of the excited N_2 to the ground state emits a photon at $\lambda = 337$ nm. The ionization, excitation and relaxation pathway can be summarized below:

$$N_2 + Kh\nu \rightarrow N_2^+ + e^- \tag{3.2}$$

$$N_2^+ + N_2 \rightarrow N_4^+ \tag{3.3}$$

$$N_4^+ + e^- \rightarrow N_2(C^3\Pi_u) + N_2(B^3\Pi_g) \tag{3.4}$$

$$N_2(C^3\Pi_u) \rightarrow N_2(B^3\Pi_g) \tag{3.5}$$

where K is the number of photons required to ionize molecular nitrogen. ($K = 10$ because the ionization potential $U_i = 15.58$ eV for N_2.) Although both fluorescent wavelengths ($\lambda = 391$ nm $\lambda = 337$ nm) can be used to trace out the ionization channel of a filament, the second positive band system is typically used because it has a longer lifetime [44].

The experimental setup to investigate the filament length based on the fluorescence of nitrogen is sketched in Fig. 3.14(a). One advantage of using nitrogen fluorescence over the ionization technique is that a higher spatial resolution can be achieved longitudinally. (This is because the electrical length of a filament was inte-

grated over the gap of the electrodes for each voltage measurement.) The nitrogen fluorescence was collected by an uncoated fused silica lens $f = +5$ cm guiding light onto a photomultiplier tube (PMT) that had a spectral response in the UV region. An interference filter (Edmund Optics NT62-130) centered at $\lambda = 337$ nm and bandwidth $\triangle\lambda = 10$ nm was used to block out the laser light and any other emission except at $\lambda = 337$ nm. The peak transmission of the interference filter was about 30%. A typical voltage trace from the PMT is shown in Fig. 3.14(b). We can see that the full-width at half maximum (FWHM) of the voltage signal is less than 10 ns, which is limited by the bandwidth of the PMT.

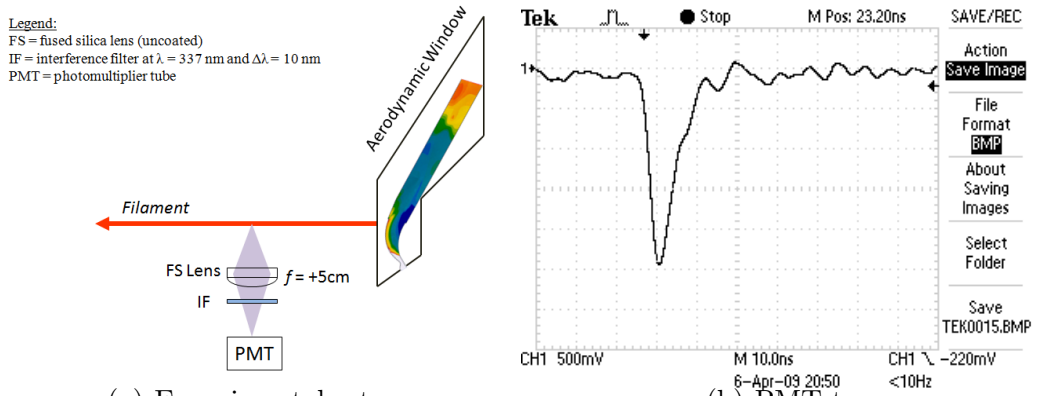

(a) Experimental setup (b) PMT trace

Figure 3.14: (a) Experimental setup to detect the nitrogen fluorescence from a filament; (b) PMT signal of the fluorescence on an oscilloscope.

By scanning the PMT along the propagation of the filament, we were able to characterize the length of the filaments that were initially prepared in air or in vacuum, as graphed in Fig. 3.15. We can see that the onset of filamentation was shifted about 24 cm downstream from the geometric focus in the case of vacuum preparation of the filament. For the case of ambient air, a slight increase in the fluorescence signal at $z = 10$ cm may be explained by a refocusing event of a filament, provided that the power exceeded the critical power, P_{cr}.

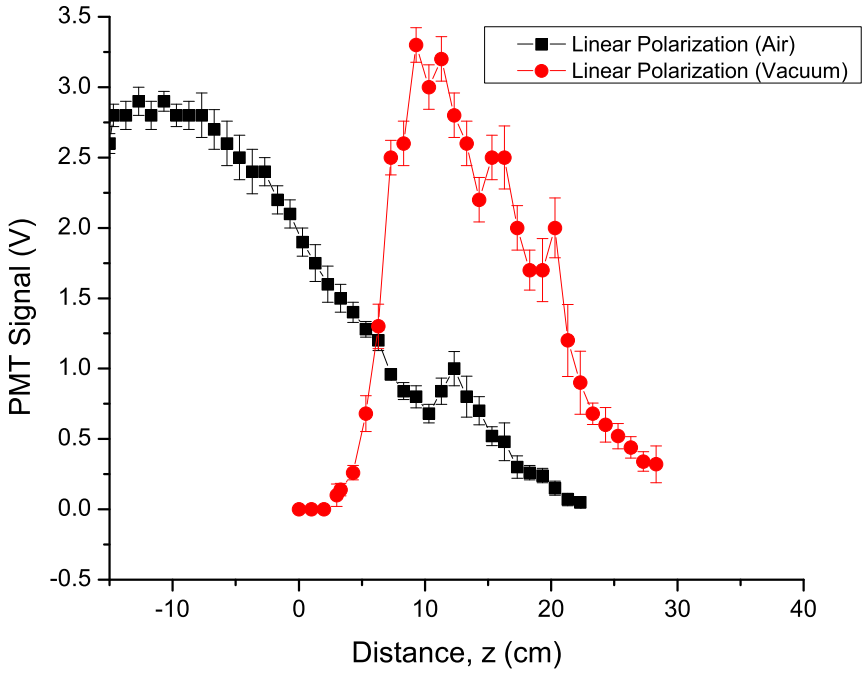

Figure 3.15: Nitrogen fluorescence at $\lambda = 377$ nm by an optical filament along its propagation path z with the geometrical focus is at $z = 0$ cm. (We have previously reported this result in [40].)

3.4 Polarization Dependence

We have also applied the aerodynamic window to the formation of optical filaments using circularly polarized femtosecond laser pulses. In the experiments described above, the laser pulse was p-polarized. Two thin film polarizers (TFPs) with 200:1 polarization extinction ratio were used in series to achieve an extinction ratio greater than 40000:1. In the following experiments, the thin film polarizers were replaced with a quarter-wave plate ($\lambda/4$) to generate circularly polarized light.

3.4.1 Ionization of Air

The experimental setup shown in Fig. 3.12 was used again to detect the relative ionization along the propagation path of a filament. Fig. 3.16 compares the induced voltages between a linearly polarized filament and a circularly polarized filament that was prepared in air. Overall, the induced voltage for the circularly polarized filament is smaller than that for the linearly polarized filament. Furthermore, its slope is also steeper, which means that plasma generation ended at a faster rate for the circularly polarized case.

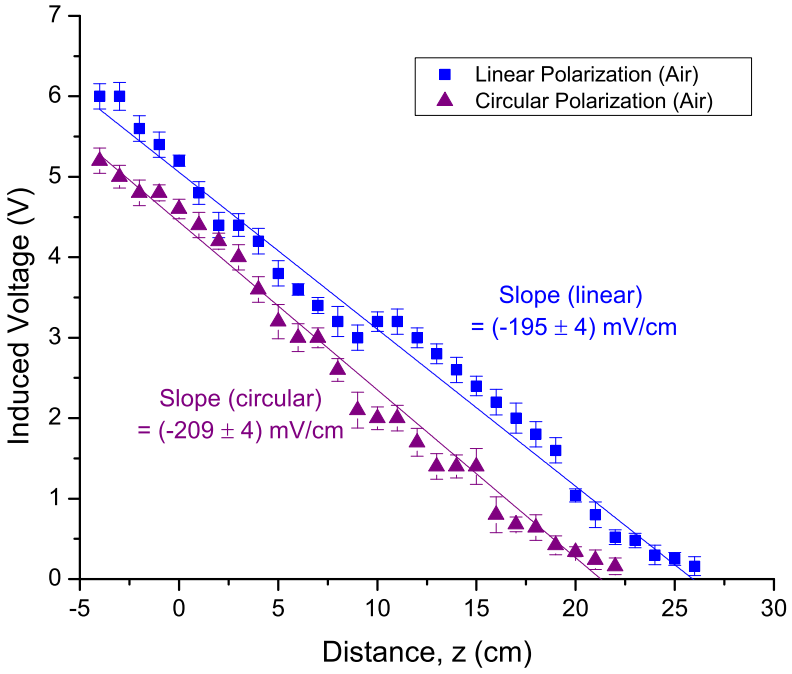

Figure 3.16: Relative ionization by an optical filament that is prepared in air for linear and circular polarization along its propagation path z with the geometrical focus of the lens at $z = 0$. (We have previously reported this result in [40].)

Fig. 3.17 shows the respective distance variation of the electrical breakdown volt-

age in air, triggered by both linearly and circularly polarized filaments that were launched in air. In the case of a circularly polarized filament in air, the breakdown voltage threshold was higher than that for the linearly polarized filament over the measured range of 10 cm $\leq z \leq$ 20 cm. This is consistent with the observation of the relative ionization results obtained in Fig. 3.16 where the induced voltages for circular polarization were less than that for linear polarization. In addition to the decreased ionization level for a circularly polarized filament in air, its plasma channel terminated earlier, as evident in both Fig. 3.16 and Fig. 3.17.

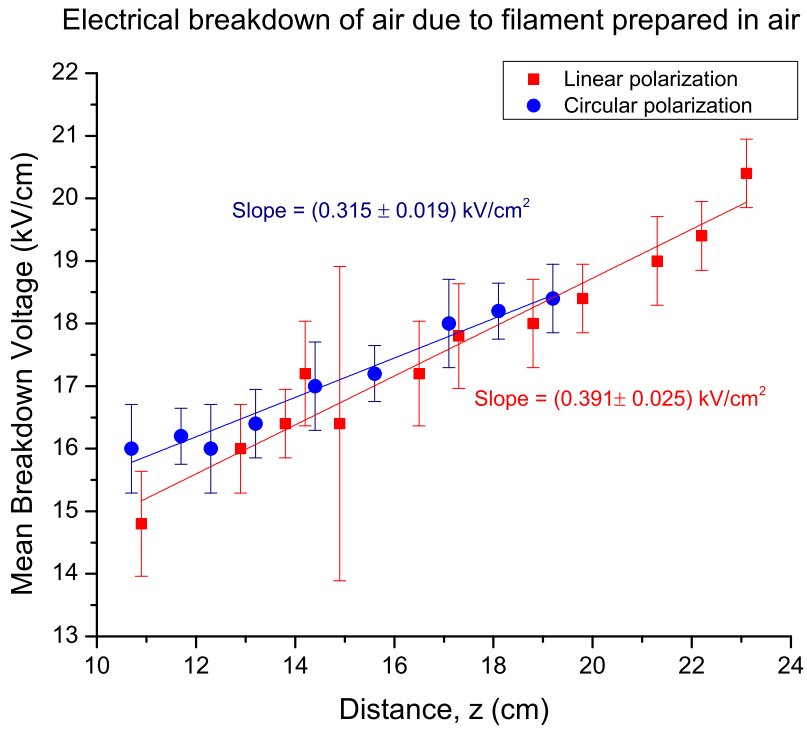

Figure 3.17: Laser-triggered breakdown voltage versus distance by linearly and circularly polarized filament prepared in air.

When a circularly polarized laser pulse was launched into vacuum to create a filament, no induced voltage was detected across the load resistor.

3.4.2 Nitrogen Fluorescence

We repeated the detection of nitrogen fluorescence at $\lambda = 337$ nm using a circularly polarized filament for both cases of the filament being launched in air and also in vacuum. The results are displayed in Fig. 3.18. Firstly, we can see that the maximum fluorescence induced by the circularly polarized filament in air was smaller than that for the linearly polarized filament. Secondly, for circular polarization, the refocusing event took place sooner (at $z = 6$ cm) relative to the linear polarization refocusing event (at $z = 12$ cm). This refocusing event (for circular polarization) also seems weaker than that for the linear polarization.

For circularly polarized filaments that were launched in vacuum and onto the aerodynamic window, no nitrogen fluorescence was detected. This confirmed the earlier relative ionization measurement, where no induced voltages were detected for the case of a circularly polarized filament that was initially prepared in vacuum.

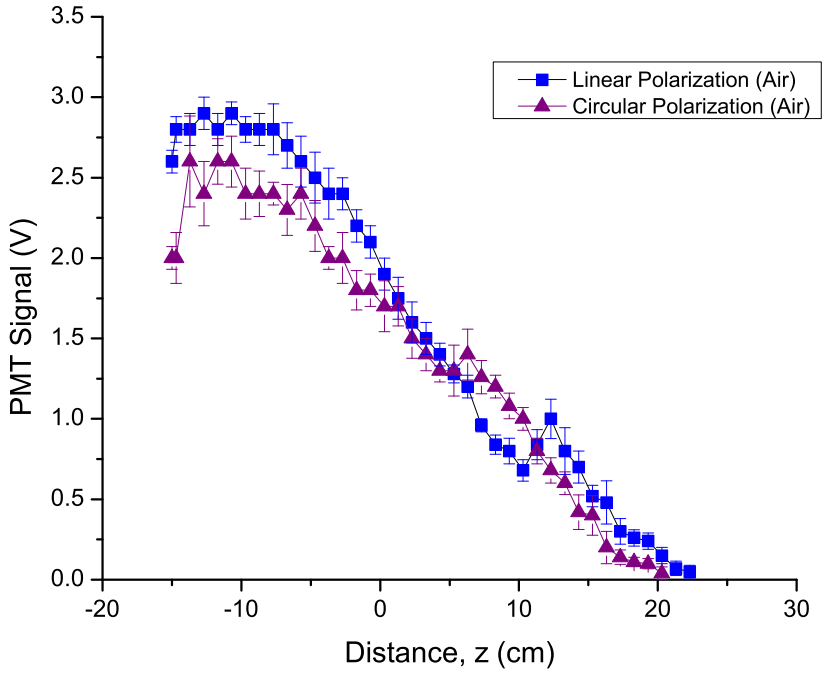

Figure 3.18: Nitrogen fluorescence from linearly and circularly polarized filaments that were prepared in air along the propagation path z with the geometrical focus of the lens at $z = 0$. (We have previously reported this result in [40].)

3.5 Discussion

To understand these experimental results for both linearly and circularly polarized filaments, we must consider the tensor nature of the third-order susceptibility $\chi^{(3)}_{ijkl}$ that is responsible for the nonlinear index of refraction $\tilde{n}_2$. For an isotropic medium like air, the third order nonlinear polarization can be written as [45]:

$$\mathbf{P}^{(3)} = \epsilon_0 A(\mathbf{E}\cdot\mathbf{E}^*) + \frac{1}{2}\epsilon_0 B(\mathbf{E}\cdot\mathbf{E})\mathbf{E}^* \tag{3.6}$$

where $A = 6\chi_{1122}$, $B = 6\chi_{1221}$ and $\mathbf{E} = \frac{1}{2}\tilde{\mathcal{E}}e^{i\omega t}$ + c.c. is the electric field.

Any transverse electric field **E** propagating in the z-direction can be decomposed into a combination of two orthogonal components (for example, either into $\hat{\mathbf{x}}$ and $\hat{\mathbf{y}}$ or into left- and right-hand circular polarization unit vectors $\hat{\sigma_+}$ and $\hat{\sigma_-}$). The circular polarization unit vectors are related to the Cartesian unit vectors through:

$$\hat{\sigma_\pm} = \frac{\hat{\mathbf{x}} \pm i\hat{\mathbf{y}}}{\sqrt{2}} \tag{3.7}$$

with the plus sign (+) corresponding to left-hand circular polarization and the minus sign (–) to right-hand circular polarization. Because of the third-order polarization in Eq. 3.6, the index of refraction in air can be expressed in terms of left- and right-circular polarization terms as [45]:

$$n_\pm^2 = n_0^2\Big(1 + \frac{1}{n_0^2}[A|\tilde{\mathcal{E}_\pm}|^2 + (A+B)|\tilde{\mathcal{E}_\mp}|^2\Big) \tag{3.8}$$

which leads to

$$n_\pm \approx n_0 + \underbrace{\frac{1}{2n_0}[A|\tilde{\mathcal{E}_\pm}|^2 + (A+B)|\tilde{\mathcal{E}_\mp}|^2}_{\delta n_2}\,. \tag{3.9}$$

For circularly polarized light, the change in the refractive index due to the third-order susceptibility is

$$\delta n_{2,circ} = \frac{1}{2n_0}A|\tilde{\mathcal{E}}|^2 \tag{3.10}$$

while for linearly polarized light, the refractive index change is given by:

$$\delta n_{2,lin} = \frac{1}{2n_0}(A + \frac{1}{2}B)|\tilde{\mathcal{E}}|^2. \tag{3.11}$$

Thus, the ratio between Eq. 3.11 to Eq. 3.10 is:

$$\frac{\delta n_{2,lin}}{\delta n_{2,circ}} = 1 + \frac{B}{2A}. \tag{3.12}$$

For nonlinearities arising from molecular orientation, B/A = 6, while for nonresonant electronic nonlinearties, B/A = 1. This means that $\tilde{n}_{2,circ} = \frac{1}{4} \times \tilde{n}_{2,lin}$ if the nonlinear

susceptibility is only due to the orientation of the *molecules* in response to the electric field of the laser pulse; or $\tilde{n}_{2,circ} = \frac{2}{3} \times \tilde{n}_{2,lin}$ when the electronic response of *bound electrons* to the electric field is only considered. In the discussion to follow, we will assume that the nonlinear refractive index for circular polarization is two thirds that of the linear polarization. This means that the critical power for circular polarization is 1.5 times larger than for linear polarization, $P_{cr,circ} = \frac{3}{2} P_{cr,lin}$.

In the experiments above, we observed a shift $\triangle z = 24$ cm in the onset of filamentation based on the nitrogen fluorescence between linearly polarized filaments prepared in air and in vacuum (Fig. 3.15). If we take this shift from the geometrical focus as due to self-focusing alone, we can calculate the self-focusing distance z_{sf} based on:

$$\begin{aligned} \frac{1}{f_{new}} &= \frac{1}{f_{lens}} + \frac{1}{z_{sf}} \\ \frac{1}{z_{sf}} &= \frac{1}{f_{lens}} - \frac{1}{f_{new}} = \frac{1}{3} - \frac{1}{3 - 0.24} \\ \Rightarrow z_{sf} &= 34.5 \text{ meters.} \end{aligned} \tag{3.13}$$

Using this value of z_{sf}, we can proceed to calculating the critical power for linear polarization $P_{cr,lin}$ since we know the peak power of the laser pulse $P = 9$ mJ/250 fs = 36 GW using:

$$z_{sf} = \frac{0.367 k a^2}{\left\{ \left[\left(\frac{P}{P_{cr,lin}} \right)^{1/2} - 0.852 \right]^2 - 0.0219 \right\}^{1/2}} \tag{3.14}$$

from which we obtain $P_{cr,lin} = 0.896$ GW, which is closer to the calculated value of the critical power defined by the wavefront curvature. Assuming that the critical power for circular polarization is 1.5 times larger than that for linear polarization, $P_{cr,circ} = 1.5$ x $P_{cr,lin}$, the self-focusing distance for circular polarization is $z_{sf} =$ 43.78 meters, and the shift in the onset for filamentation for a circularly polarized

laser pulse in air is $\triangle z = 19.24$ cm ≈ 19 cm, which is about 5 cm *later* compared to the onset of filamentation for linearly polarized laser in air[1]. This is consistent with our observation in Fig. 3.18 where the peak of nitrogen fluorescence occurred before the geometrical focus ($z = 0$ cm) for a circularly polarized filament prepared in air although it is difficult to assess how far it is from the peak of the nitrogen fluorescence coming from a linearly polarized filament prepared in air because of its overall reduced intensity with circular polarization.

Despite a stronger focus due to self-focusing in air, the optical filament beam size increased at a larger rate when it was prepared in air instead of in vacuum (Fig. 3.8). This is easily explained by the generation of a plasma that serves to overcome the collapse of the beam due to self-focusing. Without this defocusing effect, the minimum filament spot size can be further reduced, as evident when the the filament was prepared in vacuum. However, even when the filament was prepared in vacuum, the minimum spot size was $w_0 = 200$ μm, which was still larger than the expected minimum spot size ($w_0 = 186$ μm) for a Gaussian beam with $w = 4$ mm (at $1/e^2$), focused by an $f = +3$ m lens. This implies that plasma generation played a role in balancing the self-focusing in the filament. It also appears that $w_0 = 200$ μm may be the lower limit for the filament beam size formed with an $f/375$ lens in air – regardless of whether the filament is initially formed in air or in vacuum. Any reduction in the beam size will lead to greater plasma generation that in turn, will cause a stronger defocusing effect, for which self-focusing may not be able to compensate in order to have a self-sustaining filament.

In our experimental results, a higher ionization level was observed for linearly po-

[1] $\triangle z$ is defined as the difference in distance between the geometrical focus and the onset of filamentation, which occurs before the geometrical focus. If $\triangle z$ is large, the filament begins to form very much prior to the geometrical focus position. Thus, for $\triangle z = 19$ cm, the onset of filamentation is closer to the geometrical focus compared to the case for $\triangle z = 24$ cm. This means that the filamentation will occur at a later stage for a circularly polarized filament.

larized filaments, which were initially prepared in vacuum due to a more constrained beam diameter. The Kerr self-focusing term $\tilde{n}_2 I$ was sufficiently strong to overcome the defocusing due to stronger plasma generation caused by the increase in peak intensity, I. However, if this dynamic balance is offset by a sudden increase in the free electron density, the beam may still generate a laser spark in air, but it will terminate shortly thereafter and diverge very quickly. This case is quite common when a high power beam is focused strongly by a short focal length lens in air. In our experiments where a circularly polarized intense laser beam was launched into vacuum, we did not observe any ionization signal (in the form of an induced current flowing across a pair of electrodes or nitrogen fluorescence) after the aerodynamic window. We hypothesize that the minimum spot size was smaller than $w_0 = 200$ μm because of the higher critical power for circular polarization[2]. This would have created a denser plasma at the interface of vacuum and ambient pressure, and would have defocused the beam more strongly. The generation of this short but strong laser plasma channel would not have provided self-focusing an opportunity to balance the defocusing in a self-sustaining way. Consequently, the circularly polarized "filament" terminated rather abruptly.

We can summarize the experimental results presented in this chapter as the following: Initial conditions are critical to the formation and sustainment of optical filaments in air. The initial conditions can dictate the beam size of the filament, peak intensity and plasma generation that all play a role in the dynamic balance over long propagation distances. We have demonstrated the utility of an aerodynamic window to change the initial conditions in the formation of optical filaments.

[2]Although we had expected that circular polarization would have yielded a slightly smaller beam diameter and thus, a stronger intensity and greater plasma generation, we did not observe this to be the case for filaments that were prepared in air. This may be due to the other nonlinear losses, such as multiphoton excitation of molecules, that are also intensity-dependent – increasing losses at higher intensities, and reducing the overall plasma generation.

Chapter 4

Gas Dynamics and the Interaction of Repeated Optical Filaments in Air

Although the potential of filaments has long been identified for remote sensing applications, either in light detection and ranging (LIDAR) [14] or in laser-induced breakdown spectroscopy (LIBS) [13, 46, 47], and weather applications, such as laser-triggered lightning [7, 16, 9, 48] and cloud seeding [49], much of their promise remains unfulfilled because of intensity clamping that limits the amount of energy that can be coupled into a single filament for long range propagation [1]. Consequently, a single optical filament can only propagate up to a certain distance due to energy losses through ionization and other nonlinear absorption processes. Increasing the pulse energy will not extend the propagation distance of a single filament since a modulational instability will cause the beam to break up into multiple filaments [50] with each individual filament experiencing intensity clamping. Different techniques have been employed to control the onset of multiple filaments by use of a telescope [51], beam ellipticity [52, 53], chirp/dispersion management [54] and phase masks [55, 56].

However, for an initial Gaussian laser beam, these techniques are not capable of extending the propagation of a single filament nor do they enhance the nonlinear effects in the filamentation process – they only influence the start of filamentation. In this chapter, we will investigate and report how gas dynamcis can affect the long range propagation of optical filaments at high repetition rates. This aspect of filamentation dynamics has been performed in my work at PM&AM Research, LLC and has not been explored until now.

4.1 High Repetition Rate Femtosecond Laser System

We used a custom-built two-tier femtosecond laser amplifier system for the experiments reported in this chapter. The overview of the entire laser system is illustrated in the block diagram of Fig. 4.1. This laser system produces 9 W of average power from the kilohertz tier, and over 10 TW of peak power from the 10 Hz tier.

At the very heart of the laser is the Kerr-lens mode-locked titanium:sapphire oscillator which provides a 90-MHz pulse train with pulses less than 25 fs in duration. The spectrum and the calculated transform-limited pulse duration from the oscillator are shown in Fig. 4.2. A bandwidth of $\triangle\lambda \geq 50$ nm is needed to ensure that there is sufficient bandwidth going into the stretcher, amplifier and compressor to produce less than 30 fs pulses at the output.

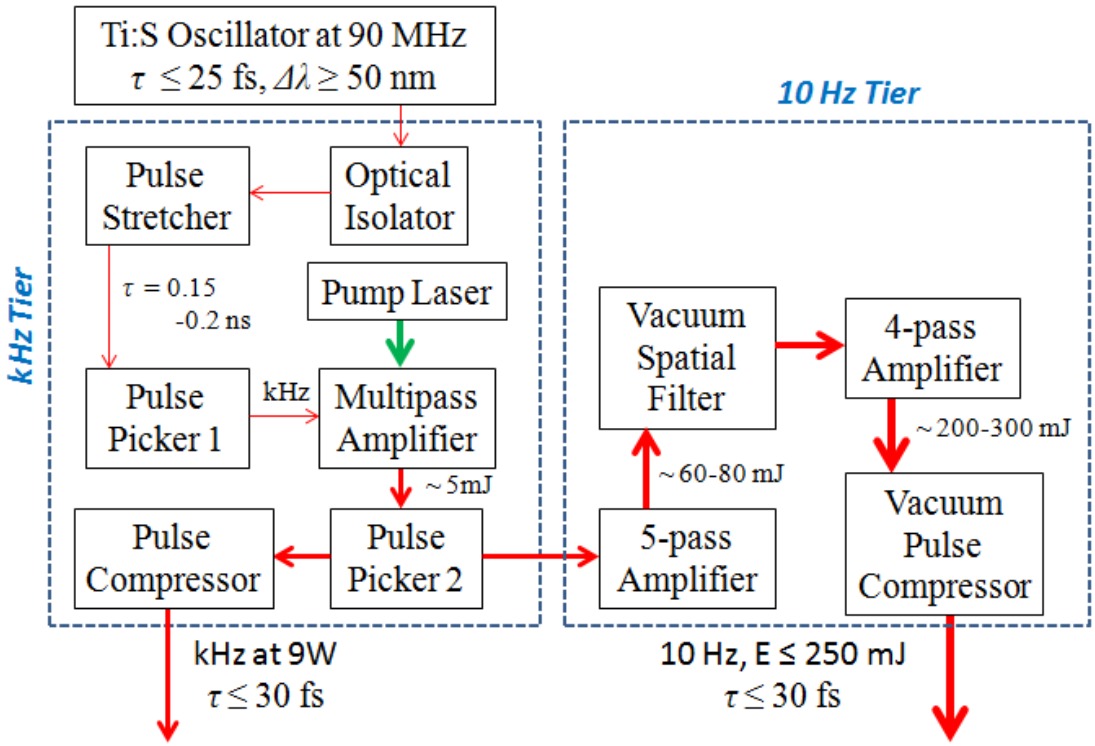

Figure 4.1: Block diagram showing the main sub-assemblies of a two-tier high average power and high peak power femtosecond titanium:sapphire amplifier laser system. (PM&AM Research, IR&D)

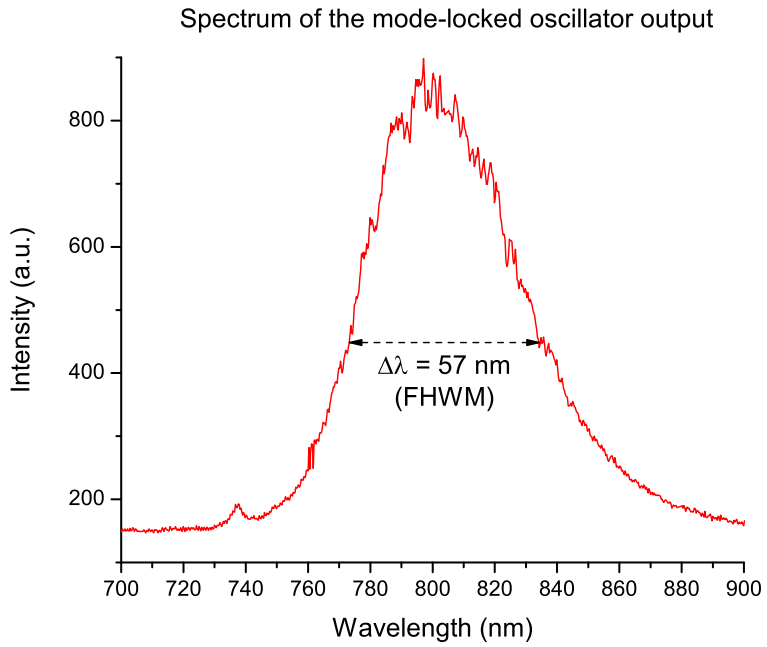

(a) Spectrum of oscillator pulse

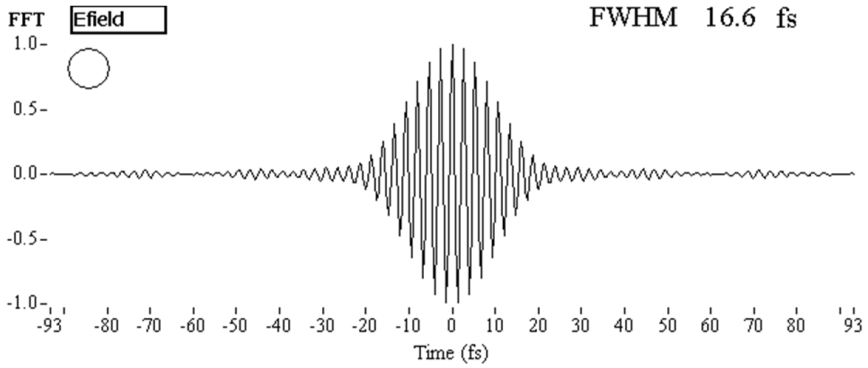

(b) Calculated transform-limited pulse from the oscillator

Figure 4.2: Output of the Kerr-lens mode-locked (KLM) titanium:sapphire oscillator (a) Pulse spectrum; (b) Calculated pulse duration. (PM&AM Research, IR&D)

As with all chirped-pulse amplifier systems, the output of the oscillator is sent to the pulse stretcher via an optical isolator to prevent any feedback into the oscillator. The pulse stretcher increases the pulse duration from sub-25 fs to 150-200 ps by

positively chirping the pulse. Stretching the pulse reduces the pulse intensity, and thus prevents any damage to the optics during the amplification of the pulse. Coming out of the pulse stretcher, the pulse goes into the first pulse picker that consists of a Pockels cell placed between a pair of calcite polarizers. The function of the pulse picker is to select a kilohertz pulse train (nominally at 3 kHz) from the 90-MHz pulse train for amplification. After the pulse picker, the pulse has a vertical (s) polarization going into the multipass amplifier.

In the multipass amplifier, the crystal is pumped by a second harmonic Nd:YLF laser at $\lambda = 527$ nm. The pump laser pulse is also s-polarized in the amplifier stage. The Ti:S crystal is cooled to a cryogenic temperature of at least –232 °C, allowing the operation of the laser at different repetition rates without worrying about thermal lensing in the crystal. After passing through the Brewster-cut titanium:sapphire crystal (Ti:S) 14 times, the pulse emerges from the amplifier with 15 W of average power, or nominally 5 mJ at 3-kHz repetition rate.

This pulse then goes through a second pulse picker, as schematically depicted in Fig. 4.3, which then picks 10-Hz pulses from the kilohertz pulse train for further amplification in the 10-Hz tier. In the normal operation of the second pulse picker, the s-polarized pulses from the amplifier are rotated to p-polarization by the half-wave plate (HWP). A half-wave voltage pulse is applied to the Pockels cell (PC) at 10 Hz to rotate the p-polarized pulses back into s-polarization. These 10 Hz pulses are reflected off the thin film polarizer (TFP) into the 10-Hz tier. The rest of the pulses remain in p-polarization and are transmitted through the TFP into the pulse compressor. If the Pockels cell is turned off, all the kilohertz pulses are directed into the pulse compressor, which then compresses the stretched pulses back to sub-30 fs pulses. The output pulse duration is measured using a commercial frequency-resolved optical gating (FROG) instrument. A typical pulse measurement is shown in Fig. 4.4 where $\tau = 23.5$ fs. The output beam diameter from the kilohertz tier $D =$

6 mm (at $1/e^2$) and the maximum pulse energy is 3 mJ at a repetition rate of 3 kHz.

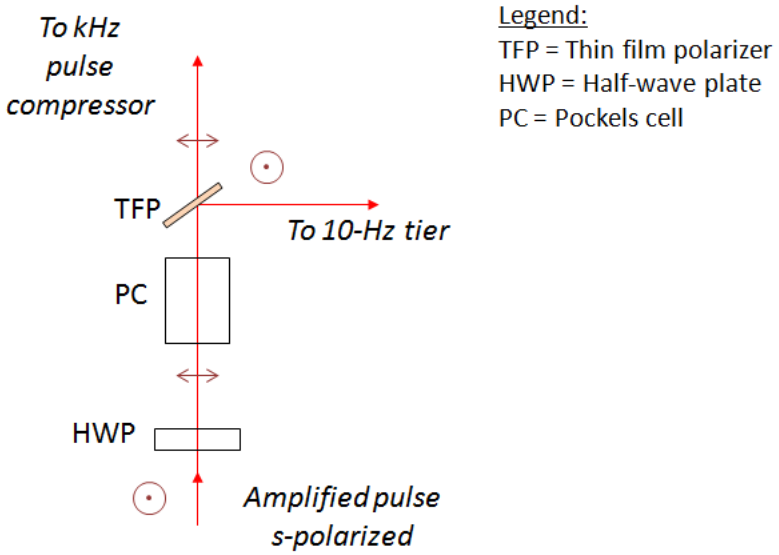

Figure 4.3: Second pulse picker to select 10 Hz pulses for further amplification in the terawatt amplifier stage. (PM&AM Research, IR&D)

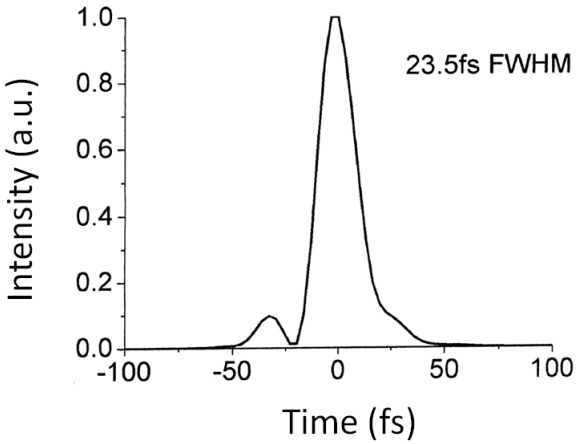

Figure 4.4: Measurement of the pulse duration at the output of the kilohertz tier. (PM&AM Research, IR&D)

In the 10-Hz tier, the nominally 5-mJ uncompressed seed pulse from the kHz tier is sent to a 5-pass amplifier to increase the pulse energy to about 60-80 mJ. A

vacuum spatial filter is used to clean the beam profile before the pulse is further amplified in a 4-pass amplifier crystal, boosting its energy to 300 mJ. The pulse is then compressed back down to a transform-limited pulse of less than 30 fs in the vacuum pulse compressor, with an output pulse energy of up to 250 mJ. For a typical pulse duration of $\tau \leq 25$ fs, the peak power is 10 TW. The output beam diameter from the 10-Hz stage is $D = 35$ mm (at $1/e^2$).

4.2 Observation of Filament Characteristics at High Repetition Rates

In this section, we only used the kilohertz tier of the femtosecond laser amplifier system. The half-wave plate in the second pulse picker was rotated so that the s-polarization from the output of the 14-pass amplifier was maintained, and the pulse was transmitted through the half-wave plate. The Pockels cell was triggered at 1-3 kHz, instead of at 10 Hz, converting the s-polarization back into p-polarization before the pulse compressor. Using this pulse picking scheme, we were able to obtain the different sub-harmonics of the kilohertz pulse train with a high pulse contrast ratio between amplified spontaneous emission (ASE) and the seed pulse. For example, the amplifier could still be pumped at 3 kHz while the Pockels cell in the second pulse picker was triggered to allow every other pulse (or every third pulse) to pass through the thin film polarizer, yielding a 1.5-kHz (or 1-kHz) pulse train that came out of the pulse compressor. We also measured the output power from the kHz tier, and found that the power changed according to the sub-harmonic of the nominal repetition rate of the laser amplifier system. This ensured that that no thermal lensing occured when the repetition rate of the laser was changed using the second pulse picker.

We want to point out that our method to change the repetition rate of the fil-

amenting laser system differs from the conventional technique of using an optical chopper. In a separate laser system that has a regenerative amplifier, we have observed thermal lensing affecting not only the pulse energy, but also the pulse contrast when the Pockels cells were triggered to switch the pulses in and out at different repetition rates. As such, optical choppers may be an economically viable solution, short of installing another pulse picker after the regenerative amplifier in order to change the repetition rate without thermal lensing issues. Commercially available optical choppers are currently capable of changing the repetition rate up to 1 kHz for a beam size of up to 13 mm. To control the repetition rate up to 3 kHz, the laser beam size must be smaller than 4 mm, which would restrict the placement of the optical chopper closer to the point of formation of the filament. This is not desirable since the rotation of the optical chopper wheel may introduce air turbulence that may affect the wavefront of the laser pulse undergoing filamentation in air, especially at high repetition rates. On the other hand, our pulse picking scheme, consisting of a half-wave plate, a Pockels cell and a polarizing beam splitter, is commonly used to increase the contrast ratio of the amplified pulse and to reduce the ASE for the amplification of high pulse energies (3-20 mJ) at high repetition rates (1-20 kHz). Changing the repetition rate does not affect the output pulse energy or the pulse duration, further indicating that thermal lensing is not an issue. Thus, the pulses that emerge after the additional Pockels cell from the cryogenically cooled multipass amplifier are very clean and have high contrast ratio. Selecting the pulse at the different sub-harmonics, using this Pockels cell, provides an accurate method to vary the repetition rates over 1 kHz for typical beam sizes of 5 mm or greater, without inducing any turbulent air flow in the laser beam path.

4.2.1 Displacement of Plasma Channel in a Filament

In the first set of experiments, we simply captured the air fluorescence that was emitted by the optical filaments generated by the kilohertz stage. The output beam from the laser was focused down by an $f/167$ lens, and a digital camera was used to image the plasma channel. The exposure time of the digital camera was adjusted to consistently integrate 3000 filaments in a single image frame as the repetition rate of the laser was changed. The results are shown in the series of images in Fig. 4.5. As can be seen in Fig. 4.5, the filament spanned from the 25-cm mark to the 62-cm mark at 1.5 kHz repetition rate. In these compiled images, the most visible part, corresponding to the highest degree of ionization in air, was generally displaced downstream (i.e. to the right), farther away from the lens, at higher repetition rates. Also, the length of the filament's brightest portion also appeared to generally increase with the repetition rate as it propagated down a spatially modulated density distribution.

For further characterization, we collected the emission spectrum of the filament from the side. The spectrum is shown in Fig. 4.6. The side emission of the filament exhibits strong ultraviolet lines (300 nm $\leq \lambda \leq$ 400 nm). These emission bands have been identified as coming from the the second positive band system for N_2 ($C^3\Pi_u \rightarrow B^3\Pi_g$) [57].

4.2.2 Relative Conductivity Measurements

The combined results shown in Figs. 4.5 and 4.6 imply that the ionization of air in a filament can be affected by a change in the repetition rate of the laser. To further validate and quantify this effect, we proceeded to carry out the relative ionization experiment to probe the change in ionization along the propagation of the filament in air. We employed a 2-kHz train of 25-fs, 2.5-mJ pulses with a beam size (diameter)

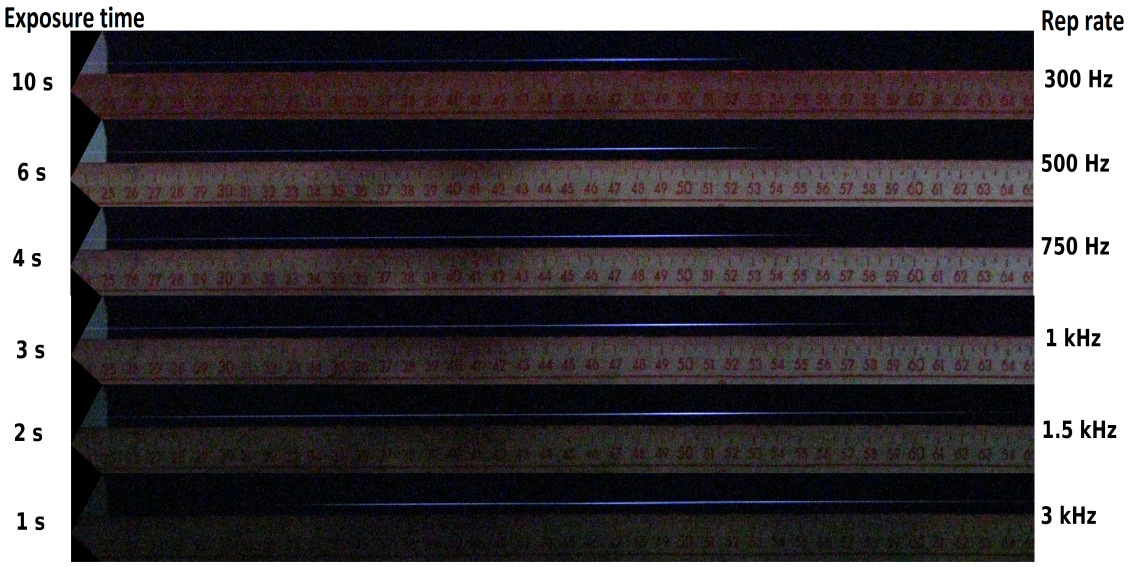

Figure 4.5: Images showing the length and position of a filament's region of brightest ionization at different repetition rates using a digital camera. The laser propagated from left to right starting at the 24.5-cm mark on the left to the 65-cm mark on the right. (PM&AM Research, IR&D)

of 6 mm (at $1/e^2$). This resulted in a peak power of roughly 100 GW, exceeding the critical power of 3.2 GW for self-focusing in air at $\lambda = 800$ nm. An adjustable telescope was used to generate optical filaments within the space constraints of our laboratory. To locate the geometrical focus of the telescope, the output pulse energy was reduced so that the laser power was much less than the critical power. The geometrical focus of the telescope was then determined to be at $z = 3.8$ m after the second lens where the focus was the sharpest. The telescope had an f-number of $f/633$. The pulse energy was then increased to 2.5 mJ. To optimize the chirp of the laser pulse emerging from the amplifier system, the grating compressor in the kilohertz stage was adjusted for the maximum plasma fluorescence at 2 kHz. The optimized pulse chirp also corresponded to the strongest white light generation in the forward direction. The entire experimental setup is schematically depicted in

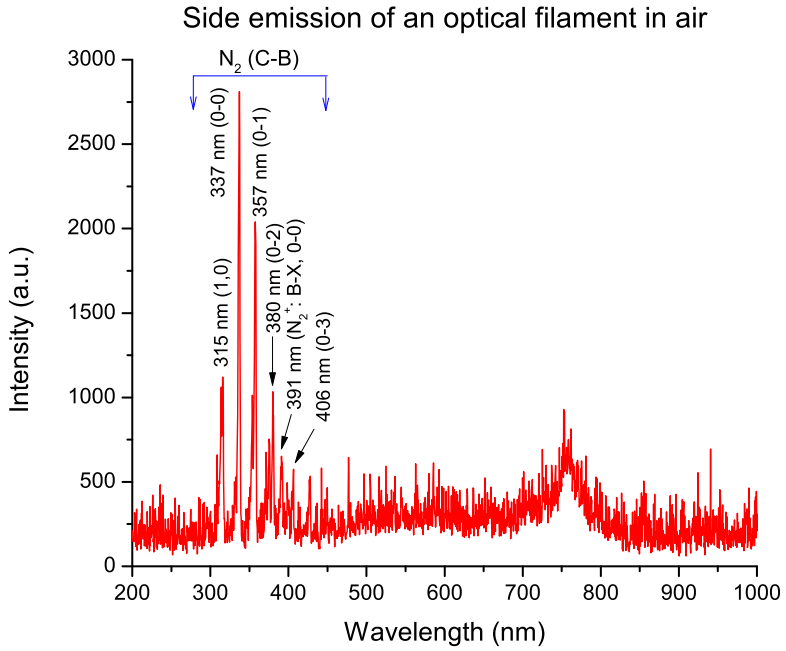

Figure 4.6: Spectral emission collected from the side of a filament using a fiber spectrometer. (PM&AM Research, IR&D)

Fig. 4.7.

The ionization along a filament was characterized using a pair of electrodes with a center bore that scanned along the filament, similar to the electrical ionization setup at UNM. The 1-cm spacing between the electrodes was kept constant. The sudden appearance of an ionized column of air between the electrodes induced a voltage across the 10-Ω resistor, which was then measured by a Tektronix digital oscilloscope DPO7254 (bandwidth: 2.5 GHz, sampling rate: 40 GS/s). The filament was centered at the bore of the electrodes to ensure that the laser pulse did not impinge on either electrode as they were scanned along the filament path. A typical voltage trace for a 2-kV bias is shown in Fig. 4.8; no further signal was observed beyond 80 ns. The observed peak voltage served as a measure of the degree of ionization in the 1-cm portion of filament between the electrodes. By scanning the

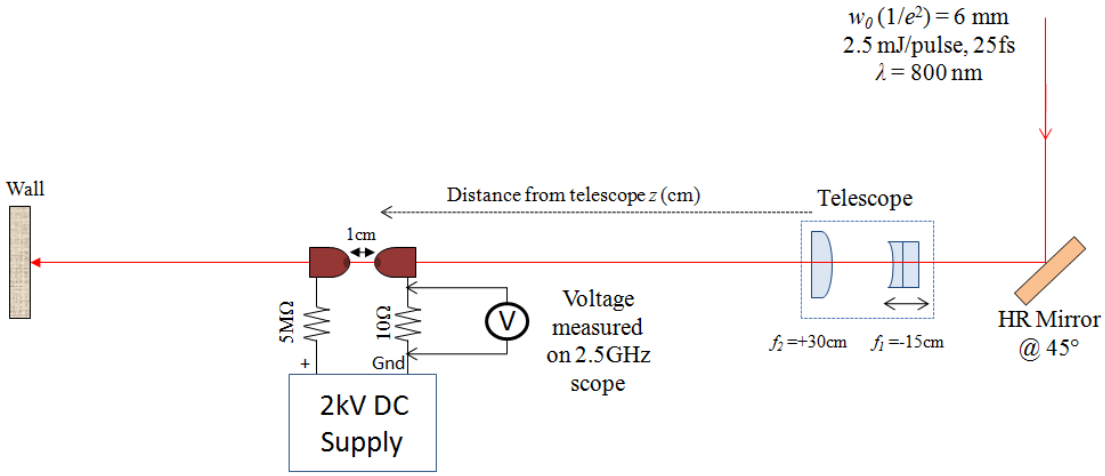

Figure 4.7: Experimental setup to measure the relative degree of ionization along the propagation path z of an optical filament in air. (PM&AM Research, IR&D)

electrode pair along the propagation path of the filament, a longitudinal distribution of the degree of ionization was obtained.

This longitudinal distribution is shown in Fig. 4.9 for five different repetition rates. We see that even at low repetition rates, the 2.5-mJ pulse produced ionization before the geometrical focus of the telescope (z= 3.80 m and $f/633$) due to nonlinear self-focusing of the laser pulse. An electrical signal was observed between 3.65 m $\leq z \leq$ 3.90 m, i.e. the electrical length of the filament is about l = 25 cm. At 1 kHz, the electrical length of the filament extended from z = 3.65 m to z = 4.25 m, while at 2 kHz, it extended beyond 4.25 m. The latter value could not be determined due to the physical constraints of our laboratory. At higher repetition rates, the peak voltage measurement increased and its position was shifted downstream, i.e. farther away from the telescope and the laser.

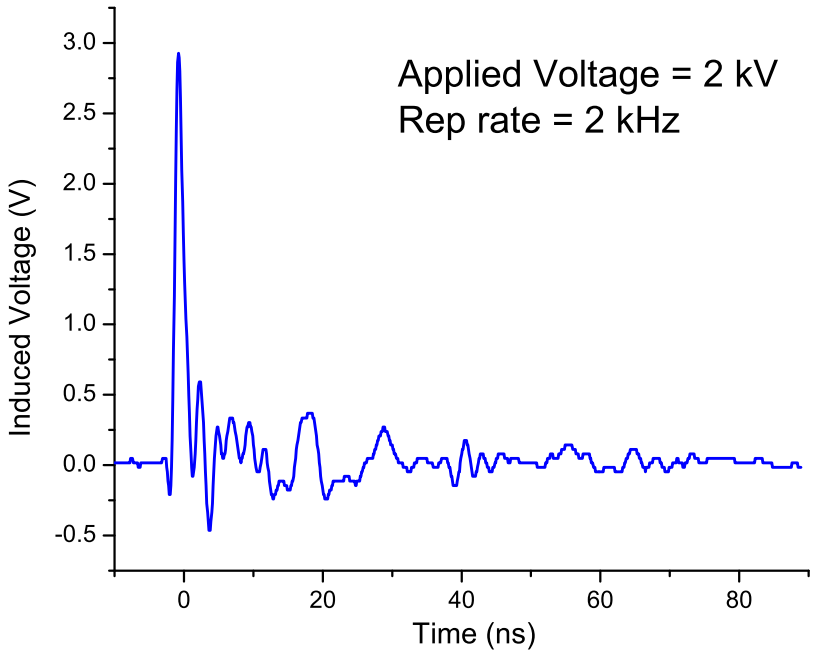

Figure 4.8: Typical waveform of the induced voltage across the 10-Ω resistive load. (PM&AM Research, IR&D)

4.2.3 Enhancement of Supercontinuum

To characterize the dependence of spectral broadening of optical filaments on the laser repetition rate, the same telescope setup ($f/633$) was used. To quantitatively measure the spectrum from a filament, a diffuse reflector was placed roughly at a distance of $z = 4.75$ meters from the f_2 lens of the telescope and at 45 ° with respect to the incident laser beam/filament to avoid any potential laser damage. The spectrum of the supercontinuum was collected from the reflective diffuser by an Ocean Optics HR2000+ fiber spectrometer with a wavelength range of 200–1100 nm and resolution of roughly 1 nm. The tip of the collecting fiber was located roughly 50 mm away from the diffuser. We adjusted the integration time of the spectrometer based on the

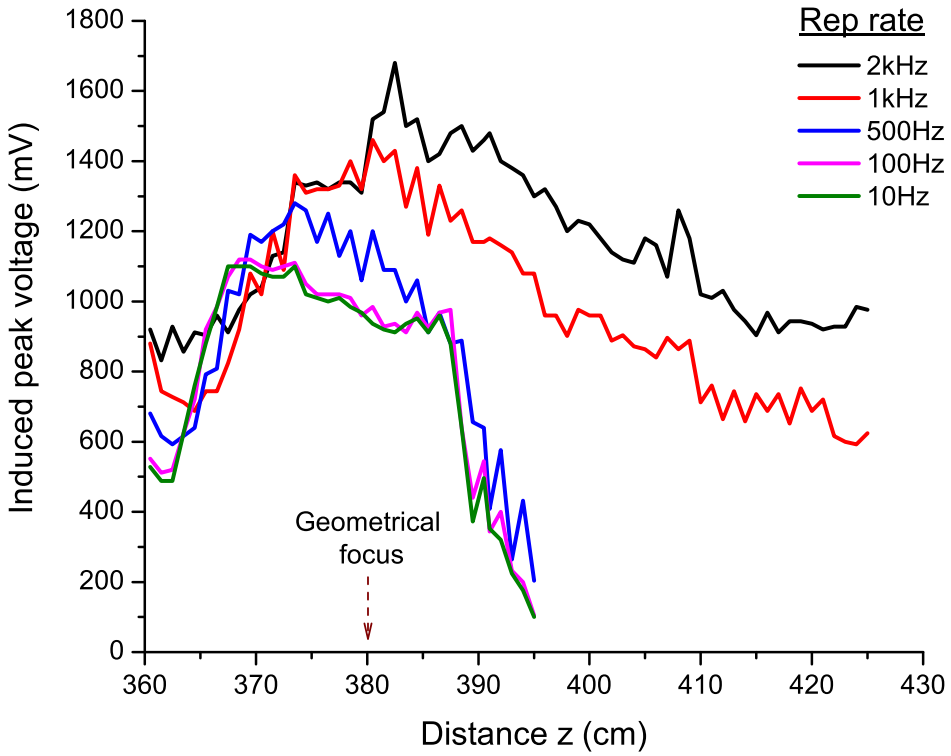

Figure 4.9: Longitudinal characterization of the degree of ionization along a filament, obtained with an adjustable telescope in air at various repetition rates. (PM&AM Research, IR&D)

repetition rate of the output laser pulses to ensure that the same number of pulses was integrated by the spectrometer. For these experiments, each spectrum recorded 10 shots at the different repetition rates. A 1-meter long PVC tube with an inner diameter of 76.2 mm was erected around the focus of the laser to shield the extended ionized path from any air currents.

The inset of Fig. 4.10 shows the spectrally broadened light exiting the ionized region and projected onto a white screen, as seen by the naked eye. The images were captured by a complementary metal-oxide-semiconductor(CMOS) camera that had

a logarithmic response to mimic the response of the human eye. Subsequent spectral measurements confirmed that the bright spot appearing at the center of the laser beam at 1 kHz and 2 kHz repetition rates was not due to saturation of the camera, but due to white light generation associated with filamentation.

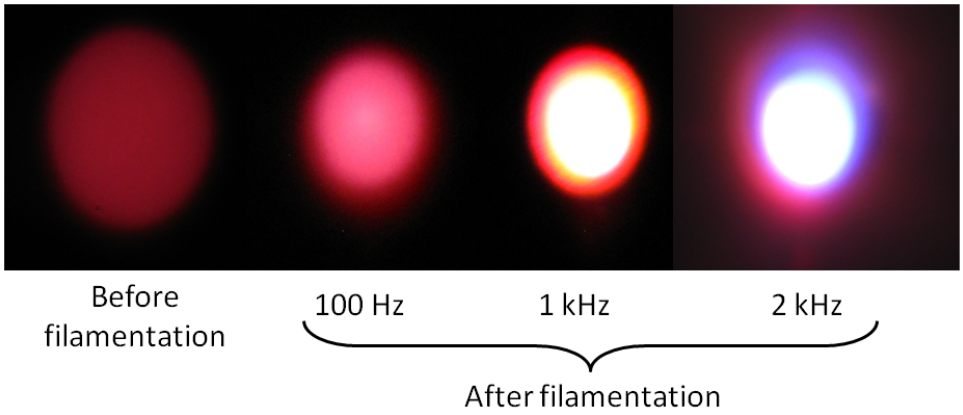

Figure 4.10: Image of the original laser beam (before filamentation), and also after filamentation at 100 Hz, 1 kHz and 2 kHz repetition rates (as seen on the diffuser by the naked eye). (PM&AM Research, IR&D)

We see in Fig. 4.11 that at a low repetition rate of 10 Hz, there was little spectral broadening in the red and blue wavelength components. This is consistent with the experimental observations of the filamentation process in air at 10 Hz, reported in the previous chapter. By increasing the repetition rate of the laser, the broadening of the spectrum increased. The blue end of the spectrum shifted from 700 nm at 500 Hz to 550 nm at 1 kHz; and to almost 400 nm at 2 kHz, while the red end of the spectrum increased from 860 nm at 500 Hz to beyond 900 nm at 2 kHz. This super spectral broadening occurred when the repetition rate of the filamenting laser increased past a threshold between 100 Hz and 1 kHz, causing the short-wavelength side of the continuum to extend further than the long-wavelength side. This produced the white light continuum seen in a filament.

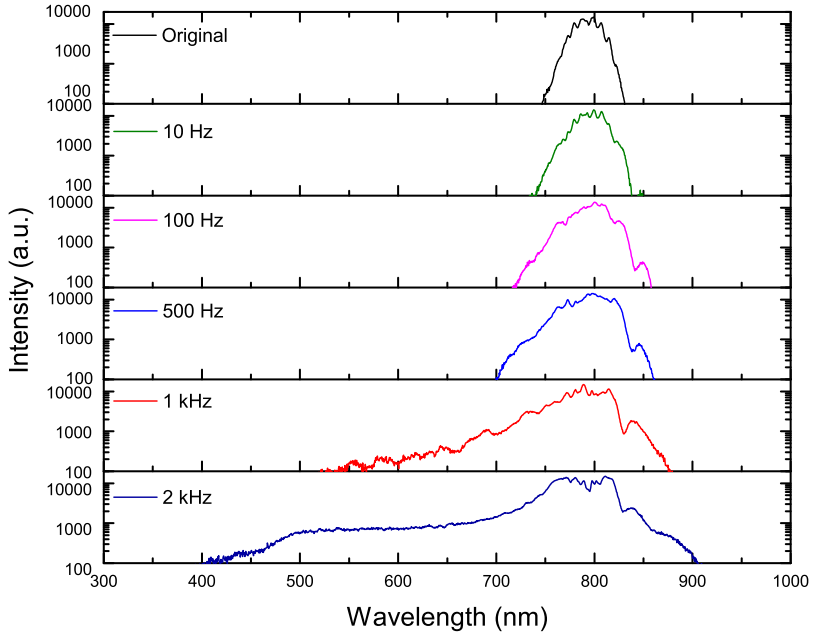

(a) Logarithmic scale

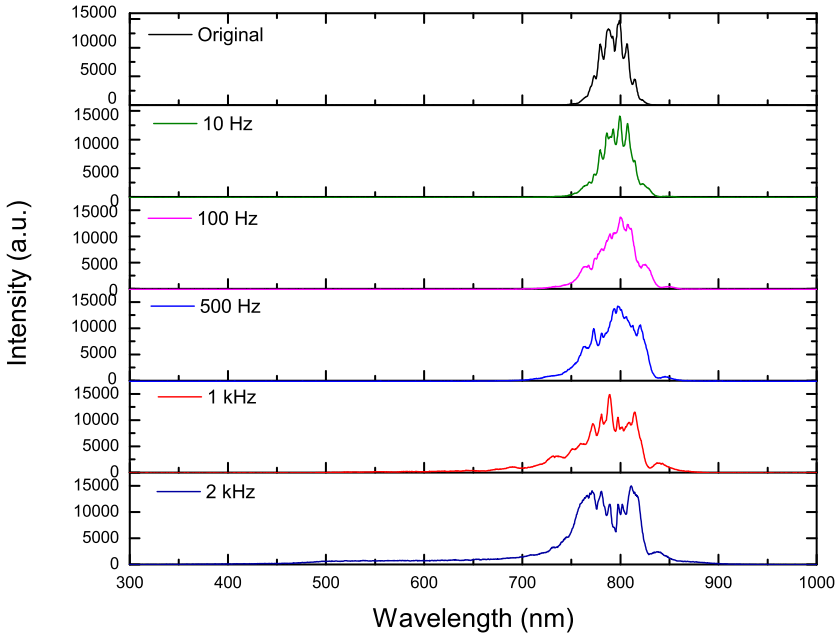

(b) Linear scale

Figure 4.11: Super spectral broadening by a filament at high repetition rates, showing spectral intensity as a function of laser repetition rate on a: (a) logarithmic scale, and (b) linear scale. (PM&AM Research, IR&D)

4.3 Understanding Gas Dynamic Interaction of Filaments through Shadowgraphy

The results in the previous sections demonstrate the existence of a threshold in the laser repetition rate, above which can significantly enhance the characteristics of an optical filament in air. In our experiments, this threshold appears to be at or below 1 kHz, suggesting a strong interaction lasting ≥ 1 ms. Based on the extensive work of PM&AM Research, LLC in this area [58, 59, 60], the effect was presumed to be due to the gas dynamics that follows from the energy deposited in the air by the optical filament. To investigate any events or processes that may have a lifetime or interaction time of up to 1 ms for the enhancement of the optical filaments beyond a 1 kHz repetition rate, we performed a shadowgraphy experiment that utilized the output beam from the 10-Hz tier. The 10-Hz output beam has a diameter $D =$ 35 mm, and the pulse energy was kept at 140 mJ. This beam was then focused at $f/15$ (using a $f = +500$-mm lens) to create a laser plasma in air. A probe beam to image the laser plasma in this shadowgraphy experiment was taken from a frequency-doubled Q-switched Nd:YAG laser. The pulse energy of the probe beam was just a few millijoules, and the duration of the pulse was 8 ns. We expanded the probe beam to 200 mm diameter and sent it perpendicular to the femtosecond laser plasma. The shadowgraph image was projected onto a screen and captured by a charged-coupled device (CCD) camera, as illustrated in Fig. 4.12. A delay generator, controlling both lasers, allowed us to vary the temporal overlap between the probe beam and the femtosecond laser beam in order to visualize the cylindrical shock wave expansion and gas dynamics resulting from the impulsive heating of the air by the laser plasma. The timing jitter between the femtosecond pump laser and the nanosecond probe laser was less than 10 ns.

Fig. 4.13 shows the temporal evolution of the gas dynamics resulting from the

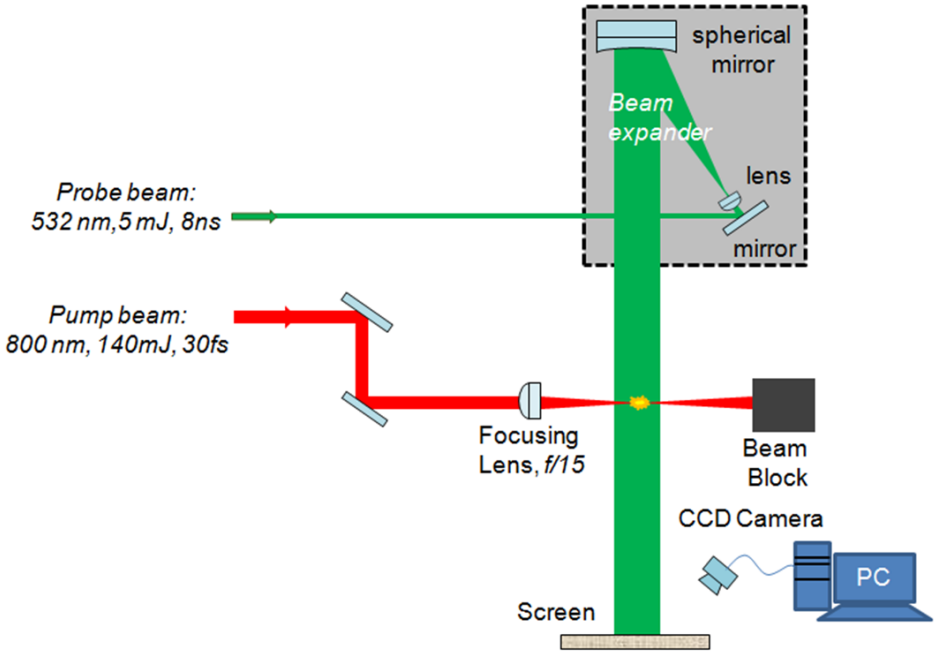

Figure 4.12: Schematic of experimental setup to perform shadowgraphy on laser plasma in air. (PM&AM Research, IR&D)

energy deposited into the air by the laser plasma. As can be seen in Fig. 4.13(a), the supersonic (blast) wave may form over the first few hundred nanoseconds as the initial energy imparted to the charged particles in air by ionization relaxes to the neutral gas particles. As shown in Fig. 4.13, air is pushed outwards by this blast wave, and the final diameter of the low-density tube is established by $t = 5$ μs. After this point, the low-density tube stops expanding, and the supersonic wave relaxes to a sonic wave. The propagation of this sonic wave away from the stationary low-density tube is clearly seen in the 10-μs, 20-μs and 50-μs time frames in Fig. 4.13(a), leaving behind the stationary "tube" containing low-density but high-temperature gas that is equilibrated to ambient pressure.

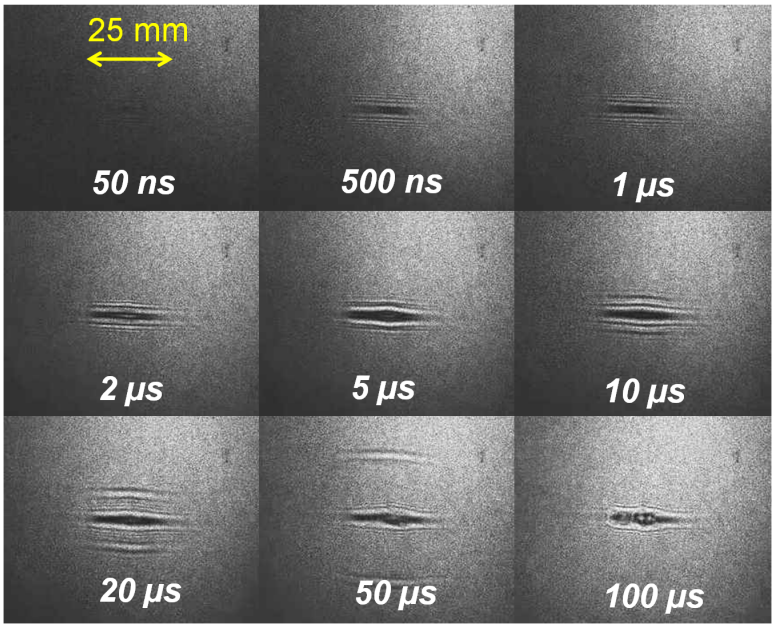

(a) Early times: 50 ns to 100 μs

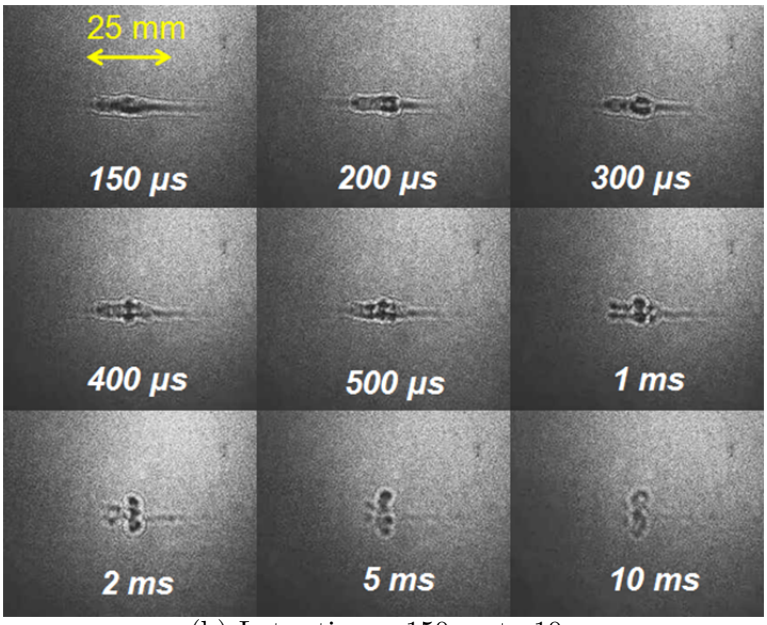

(b) Later times: 150 μs to 10 ms

Figure 4.13: Time evolution of the cylindrical shock wave and gas dynamics, resulting from the energy deposited into the air by the laser plasma: (a) 50 ns to 100 μs, and (b) 150 μs to 10 ms; laser propagates from right to left. (PM&AM Research, IR&D)

The buoyancy-induced instabilities and thermal diffusion, which govern the ensuing homogenization of the low-density tube, are sufficiently slow; and the air disturbance can persist for several milliseconds. This is true even in the presence of turbulence that may assist in the dissipation of the low-density tube [61]. As can be seen in Fig. 4.13(b), after a very long time, relative to its formation, the low-density tube starts to consolidate more markedly into a ring-formation after 2 ms and almost vanishes into the persisting buoyancy-stretched ring structure after 10 ms. This may be attributed to different competing gas-dynamic instabilities in the heated air [62]. The gas dynamics for single 2.5-mJ femtosecond laser pulses are anticipated to be very similar – opening a tube roughly 7.5 times ($= \sqrt{140 \text{ mJ}/2.5 \text{ mJ}}$) smaller in diameter. The 140-mJ pulse was imaged in order to more clearly visualize the governing gas dynamics upon ionization by the femtosecond laser pulse.

In a subsequent experiment, we clearly saw the buoyancy-stretched ring structure using 1 mJ 40-fs pulses at 5 kHz repetition rate. This is shown in Fig 4.14. This buoyancy-induced ring structure is perpendicular to the propagation of the laser plasma and is consistent with the shadowgraph images obtained for the 140-mJ 10-Hz case.

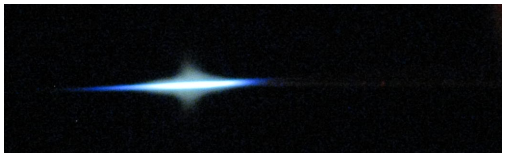

Figure 4.14: Digital photograph of laser plasma in air generated using a 40 fs 1 mJ laser pulse at 5 kHz repetition rate focused by a $f = 30$ cm lens. The laser propagated from left to right. (PM&AM Research, IR&D)

4.4 Discussion

Although optical filaments can be formed with short intense laser pulses through a dynamic balance of various competing forces (such as Kerr self-focusing, plasma defocusing, linear diffraction and other nonlinear losses), their propagation and interaction with air can be significantly enhanced by the preceding pulse(s), if the air medium has not had sufficient time to relax to initial/ambient conditions. We have shown in this chapter that at low repetition rates (below 100 Hz), the conventional undestanding of filament dynamics in air prevails: Above the critical power, the intense laser pulse undergoes self-focusing and generates a plasma trail in air, which in turn, tends to defocus the beam to prevent its collapse to a singularity. Spectral broadening due to *both* self-phase modulation and plasma generation occurs and serves to extend the bandwidth of the filamenting laser pulse in both directions (i.e., towards both longer and shorter wavelengths). The experiments detailed in this chapter show that these traits of optical filaments (filament length, plasma density and supercontinuum) can be further enhanced at high repetition rates (especially so $\geq$ 1 kHz) in ambient air.

While this may be rather surprising since it has gone unnoticed for so long until now, one can easily explain this phenomenon as a result of the relatively slow thermal response of air after a sudden deposition of the laser pulse energy. This energy deposition can take the form of an effectively instantaneous ionization of air (through multiphoton ionization) and excitation of air molecules that may lead to ion formation and non-radiative recombination that will eventually cause the heating of air.

Based on earlier work [58, 59, 63, 64], one possible mechanism for the generation of a long-lived low density region of air is by the impulsive heating of a thin line of air by a laser plasma that leads to the formation of a cylindrical shock wave propagating

faster than the speed of sound. This blast wave (a shock wave traveling faster than the speed of sound) pushes the gas cylindrically outwards at supersonic speed, away from the laser-induced plasma, leaving behind a region (or "tube") of low-density. As the tube opens, the temperature in this low-density region is expected to increase to maintain the same pressure inside the tube as the ambient pressure outside the tube. As the shock wave opens the tube radially, its growth rate begins to slow down, relaxing to a sonic wave. At the same time, the region of low density equilibrates to ambient pressure. At this point, the outward flow of gas will reverse slightly in direction, and a terminal radius r of the low density tube will be established. The final equilibrium radius is approximated by the empirical relationship [58, 59]:

$$E = 5.34 p_0 r^2 \tag{4.1}$$

where E is the energy deposited per unit length and p_0 is the ambient pressure of the gas (or air in our case). The sonic wave continues to propagate radially outward without further effect on the gas, and delivers the "snap" that one hears from the optical breakdown of air[3]. However, more experimental work will be needed, especially in temperature and pressure measurements, to ascertain the notion that the supersonic cylindrical wave is responsible for the creation of the low-density tube through the impulsive heating of air by the femtosecond laser plasma, before it decays to a sonic wave.

In our shadowgraphy experiments, the radius and length of the low density tube are measured to be 1.8 mm and 30 mm, respectively. According to Eq. 4.1, the energy deposited in this low density tube is 53 mJ, which is consistent with the loss in laser pulse energy after the formation of plasma in our experiments. Based on our observation, this low density tube retains its structure up to 63.5 μs before thermal diffusion and instabilities begin to occur, as clearly seen in Fig. 4.13. (The average

[3]This phenomenon can also be observed in nature in lightning strikes that generate thunder, and also supersonic vehicles that generate sonic booms.

propagation speed of the shock wave from $t = 5$ μs to $t = 70$ μs is $\bar{v} = 378 \pm 8$ m/s. This corresponds to a Mach number of 1.08 for ambient conditions in our laboratory.) However, the persistence of an irregularly shaped low-density tube lasts over 1 millisecond, and it is this long-lived low-density column that is responsible for the enhancement of the optical filament at high repetition rates. Because of it, the succeeding laser pulse encounters a column of air that is less dense, due to the ionization and heating by the prior pulse. Consequently, the succeeding pulse will experience less loss (both due to multiphoton ionization and excitation) and will propagate further down along the propagation path, extending the overall ionization channel. It is well within reason to expect that the generated plasma density will increase along the filament channel at high repetition rate since the ionization level of air by a single filament is much less than 1%. This increase in plasma density and the length of the filament at high repetition rates may generate a much broader spectral broadening, as observed in our experiments here. Furthermore, this super spectral broadening *may* also be attributed to self-phase modulation, which would have a stronger effect overall, given the longer dynamic interaction length of a filament at high repetition rates.

To conclude this chapter, we have shown that at repetition rates above a given threshold (for the conditions reported here, this threshold is between 100 Hz and 1 kHz), spectral broadening increases significantly, when measured after exiting the ionized portion of the filament. Combined with shadowgraphy and electrical measurements, we deduce that the super spectral broadening of a filament at high repetition rates, as well as the ability to control it, can be attributed to the persistence of the low atmospheric density region created by prior pulses. The peak and onset of the main ionization segment are displaced downstream, the length of the ionized path is increased, and the longer dynamic interaction length and modified atmosphere created by the preceding pulses result in *super* spectral broadening.

Chapter 5

Conclusion and Future Work

5.1 Concluding Remarks

The experimental work presented in this dissertation demonstrates that air plays an important role in the formation and propagation of optical filaments. By controlling the initial conditions of the formation of a filament, as was achieved with an aerodynamic window, the characteristics of a filament (such as electron density, beam size, spectral broadening) can change because of the *dynamic* balancing of various competing forces. For example, a higher plasma density may result within an optical filament if the initial beam's self-focusing is further aided by the geometrical focusing of a plano-convex lens. But if the density of the generated plasma is too high, resulting in a much stronger defocusing of the beam, the filament ceases to exist beyond the laser spark (the region of optical breakdown containing the plasma). Based on this observation, we can define an optical filament as a channel where the self-actions of the laser pulse (such as self-focusing, plasma defocusing, nonlinear losses, self-phase modulation) dynamically balance each other to overcome linear diffraction as a means to achieve a stable propagation over long distances.

Prior to this work, there has not been any publication that tied the observation of optical filamentation with the repetition rate of the laser. We were the first to report that optical filaments can be enhanced at repetition rates above 1 kHz [65]. When generating femtosecond laser filaments and plasma channels in air above a threshold repetition rate, the low-density tube generated in air does not have time to sufficiently relax back to uniform ambient atmosphere during the time between two consecutive pulses. Consequently, the propagation dynamics of the laser pulse can be affected by the modified atmospheric density-distribution left behind by the preceding pulse(s). For the laser pulse parameters, focusing geometries and atmospheric conditions used in our repetition-rate dependence investigations, the strong filament control and enhancement effects began to be most apparent for pulse separations of $\approx$ 1 ms or shorter, resulting in stronger repetition-rate dependence beginning at repetition rates greater than 1 kHz.

Based on our presentation of the repetition rate dependence of filaments at the 4^{th} International Symposium on Filamentation (COFIL2012) in Tucson [65], Howard Milchberg's group at the University of Maryland has gone on to publish independent results verifying the thermal effects on the formation of filaments in different gases [66]. Using an interferometry technique, they have shown that changes as small as $\delta n = 10^{-5}$ – 10^{-4} in the refractive index of air due to energy deposition can have a significant effect on the propagation dynamics of the subsequent filamenting laser pulses.

The thermal guiding of optical filaments in air, resulting from the gas-dynamic interactions with preceding pulses, is yet another example of how critical the initial conditions are to the formation of filaments in air. Given this newly discovered regime of filamentation, it is important that the repetition rate of the filamenting laser be considered, especially when computational modeling efforts are taken to support experimental observation and results. The omission of the seemingly unimportant

parameter – the laser repetition rate – has resulted in some "colorful" discussion on the origins of the spectral broadening [67, 11, 68, 69, 70, 71] and the existence of higher order nonlinear terms [31, 32]. In a fairly recent paper, optical rogue waves have been observed in the filamentation of short pulses in both still and turbulent air [71]. It remains to be investigated whether optical filaments displaying rogue-wave statistics is a direct consequence of evolution and persistence of the low-density tube.

5.2 Future Work

5.2.1 Thermal Contribution to the Nonlinear Index of Refraction

Until now, existing models for the propagation and formation of filaments have neglected the changes in the column of air left by the preceding laser pulse. Most, if not all, models account for the propagation of a *single* pulse propagating in a Kerr medium. This may not necessarily be the case for experiments performed with filaments, even at 100 Hz repetition rate. Following the analysis of thermal optical nonlinearity in [45], thermal effects can be included in the index of refraction according to:

$$n_{th} = n_0 + \Big(\frac{dn}{dT}\Big)T_l \tag{5.1}$$

where (dn/dT) is the index of refraction temperature dependence of a given material (and it can either be positive or negative), and T_l is the laser-induced temperature change. T_l is assumed to obey the heat transport equation given by:

$$(\rho_0 C_h)\frac{\partial T_l}{\partial t} - \kappa\nabla^2 T_l = \alpha I(r). \tag{5.2}$$

Here $\rho_0 C_h$ is the heat capacity per unit volume in J/cm^3-K, κ is the thermal conductivity in W/m-K and α is the linear absorption coefficient of the material in m^{-1}.

Assume that the temperature has a $1/r^2$-dependence. Eq. 5.2 can be approximated by:

$$(\rho_0 C_h)\frac{T_l}{\tau} - \frac{\kappa T_l}{r^2} = \alpha I(r) \tag{5.3}$$

where $\frac{\partial T_l}{\partial t} \rightarrow \frac{T_l}{\tau}$ and $\nabla^2 T_l \rightarrow \frac{T_l}{r^2}$ with τ being the response time of the medium. In the case of energy deposition through ionization of air by an intense laser pulse, we can estimate the response or relaxation time τ of air. Here, the right hand side of Eq. 5.3 is set to zero since we are specifically considering the relaxation of heated air to ambient conditions. We arrive at an estimate of the response time τ:

$$\tau = \frac{\rho_0 C_h r^2}{\kappa}. \tag{5.4}$$

Taking the heat capacity of air to be $(\rho_0 C_h) = 1.168$ x 10^{-3} J/cm^3-K at temperature $T = 300$ K and 1 atm [72], $\kappa = 26 \times 10^{-3}$ W/m-K [45] and a filament radius $w = r = 500$ μm, the relaxation time is calculated to be $\tau = 11.2$ ms. This means that thermal nonlinearity of air has to be taken into consideration for repetition rates at 100 Hz and above. For our experiments, the threshold for the enhancement of optical filaments in our experiments seem to be at 1 kHz, with a relaxation time of $\tau = 1$ ms. This would correspond to a filament beam diameter $w \approx 300$ μm, which is consistent with the measured beam size of the optical filament $w = 250$ μm at full-width at half maximum (FWHM), as shown in Fig. 5.1.

Based on these results, the size of an optical filament, which ultimately determines the relaxation time τ of air, depends on the initial conditions or the preparation of the filamenting laser pulse. These include external focusing (loose focusing vs. freely propagating filamenting beams) and the polarization of the laser pulse (where the critical power is 50 % higher for circular polarization compared to linear polarization). The energy deposited in a filament through ionization is given by:

$$E = 5.34 p_0 r^2 \tag{5.5}$$

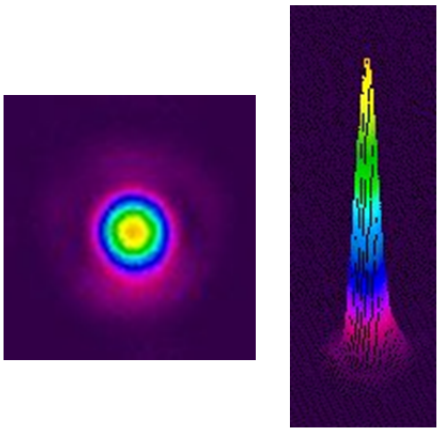

Figure 5.1: Measurement of filament diameter using a beam profiler: $w = 250$ μm (full width at half-maximum). (PM&AM Research, IR&D)

where E is the energy deposited per unit length and p_0 is the ambient pressure. The higher the energy that is deposited, the larger the radius of the low density tube will be. And this means that it will take a longer time for the air to relax to ambient conditions. If the subsequent laser pulse arrives before the air has relaxed to initial conditions, this next pulse will see a modified column of air, which may enhance filamentation effects, resulting in super spectral broadening and higher plasma density.

The experimental results presented here, hopefully, will serve as a motivation for a more comprehensive modeling of the propagation of optical filaments under *actual* atmospheric conditions. How the thermal response affects the nonlinear index of refraction must be taken into account for repetition rates faster than the relaxation of air. Whether these thermal nonlinear effects at high repetition rate also affect the linear diffraction in modeling the propagation of filaments in air will be left for future work.

5.2.2 The Path to More Powerful Filaments for Long Range Propagation

From Eq. 5.2, we can expect that the absorption coefficient α will play an important role in maintaining the low density tube initially created by the preceding filamenting laser pulses. Naturally, the absorption coefficient α depends on the temperature and pressure of the air medium. For low temperatures (below 2000 K), the Herzberg (from 240–260 nm) and Schumann-Runge bands (from 176–192.6 nm) for oxygen are the dominant absorption bands in air [73], as can been in Fig. 5.2(a). It is worth pointing out even there may be sufficient absorption taking place in the blue and violet region ($\lambda \leq 472$ nm or photon energy greater than 2.625 eV) of the electromagnetic spectrum although its value may be a couple orders of magnitude smaller than the absoprtion values in the ultraviolet and extreme ultraviolet region, as seen in Fig. 5.2(b).

To generate stronger and longer optical filaments for remote sensing and directed energy applications, it is conceivable to combine the intense high repetition rate femtosecond laser with a continuous wave (cw) laser having the right wavelength, corresponding to the maximum absorption coefficient in air. Although there is no UV laser powerful enough to generate at least a watt of power to not only maintain the low density tube created in the wake of a filamenting laser pulse but also to enhance the filament formation of subsequent pulses, it is possible to combine the output of a few blue or violet lasers to achieve comparable absorption levels, described by the term αI in Eq. 5.2. There are now commercially available diode lasers capable of providing 1–5 W of cw power at $\lambda = 405$ nm and $\lambda = 445$ nm. Nevertheless, more experiments will be needed to accurately measure the absorption coefficients at temperatures and air densities comparable to the low density tube generated by femtosecond laser pulses. There is a dearth of experimental data for the linear absorption coeffficient of air in this wavelength range.

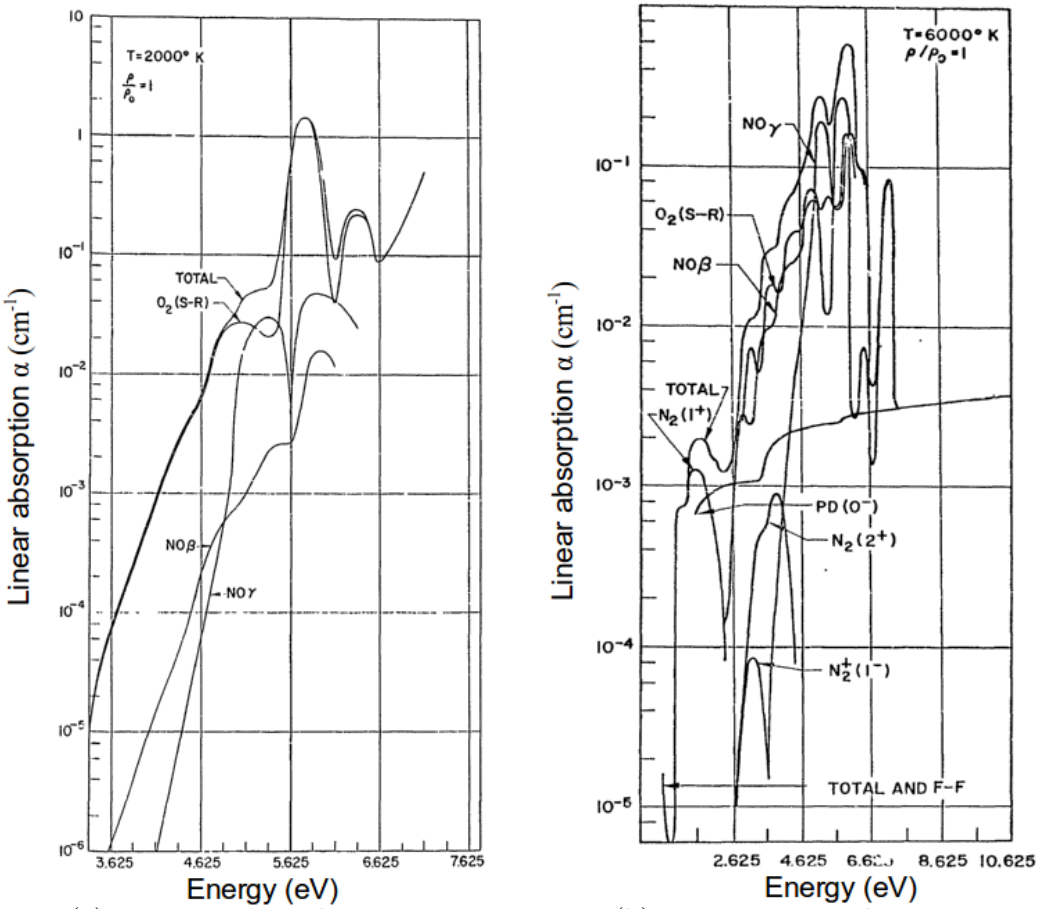

(a) T = 2000 K and P = 1 atm (b) T = 6000 K and P = 1 atm

Figure 5.2: Computed linear absorption coefficient of air at (a) T = 2000 K and P = 1 atm; and (b) T = 6000 K and P = 1 atm [73].

Another set of experiments to consider, in light of the repetition rate effects on the enhancement of optical filaments, is the lifetime of various ions and excited molecules and atoms generated by the multiphoton ionization of intense laser pulses in air. Based on electron beam radiolysis of air mixtures, ozone is the longest lived by-product radiolytic product, and has a lifetime of over 100 ms, as seen in Fig. 5.3(a) [74]. Although the initial formation of ozone from the ionization of oxygen by a femtosecond laser plasma may differ from that by electron pulse radiolysis, the build up of ozone in air is significant when using a kilohertz repetition femtosecond laser system. This is evident from the smell of ozone in the vicinity of the kilohertz laser plasma. In order to effectively maintain the low density tube for the enhancement of optical filaments over long distances at kilohertz repetition rates, more experimental work is needed to characterize the absorption coefficient of ozone so that a cw laser with the suitable wavelength can be used in conjunction with the femtosecond filamenting laser system. It is also worth pointing out that the excited molecular oxygen O_2 ($^1\triangle_g$) also has a lifetime longer than 1 ms, as do O_3^-, O_5^+ and O_4^+, as shown in Fig. 5.3(b). Thus, to enhance optical filamentation over long distances, the wavelength of the secondary cw laser beam has to match the optimum absorption band of the air molecules and their multiphoton ionization by-products, and also to generate ions and excited molecules that will live long enough between successive femtosecond laser pulses.

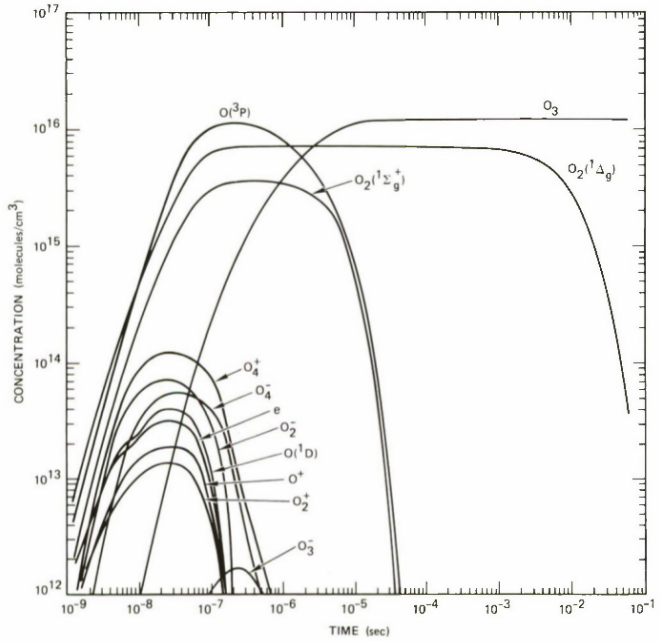

(a) Time-dependent formation of ozone

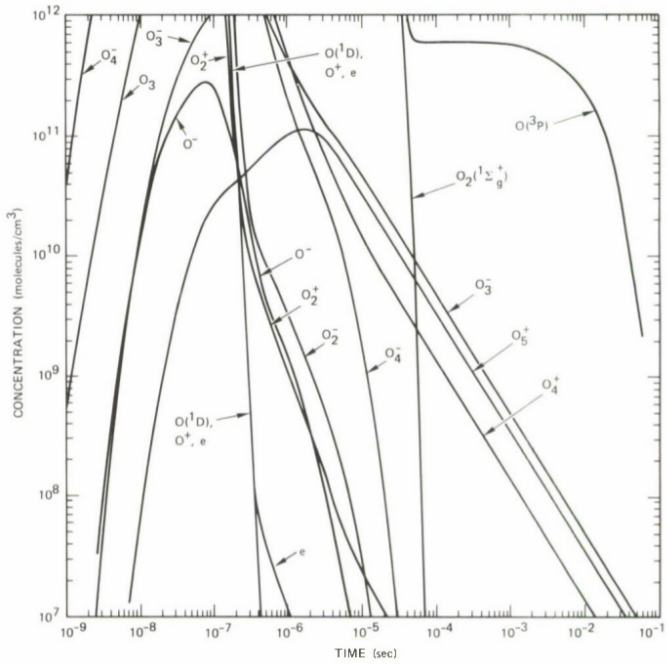

(b) Time-dependent formation of oxygen radiolytes

Figure 5.3: Time-dependent concentration of oxygen from electron pulse radiolysis at 760 Torr and T = 293 K. [74].

Our approach using a secondary cw laser to enhance femtosecond filaments for remote sensing and long range propagation of powerful laser pulses is significantly different from a recently proposed approach by the group at the University of Maryland [75] where an array of femtosecond optical filaments are used to guide powerful nanosecond laser beam. By exploiting the small changes in the index of refraction caused by optical filaments surrouding the nanosecond beam, this high power nanosecond beam may propagate over longer distances without suffering from thermal blooming or linear diffraction. Their approach of guiding a nanosecond beam by an array of filaments in air is not dissimilar to the concept of waveguiding in optical fibers (where light is confined to the fiber by total internal reflection) or channeling microwaves in a cylindrical array of filaments (where the microwaves are reflected and remained confined by electrical conductivity of the optical filaments) [76].

5.3 Potential Applications

With the demonstration that the length of an optical filament can be extended at high repetition rates, the next step is to apply this technique to a long gap high voltage discharges using intense laser pulses. A 600 kV DC discharge setup has been constructed in the laboratory. The details of this high voltage setup can be found in Appendix A.

Although the conductivity within a filament can be increased at high repetition rates, using a second laser beam may further increase the electron density through Joule heating so that the generated free electrons can be kept hot for a longer period of time for laser-triggered lightning discharge [39]. To this end, a Q-switched alexandrite laser with stretched pulses has been built. The design and experimental details are presented in Appendix B.

Appendices

Appendix A

600 kV DC Discharge Setup

A 600 kV DC discharge system has been set up in the laboratory. It consists of two PTS-300 hipots from High Voltage, Inc. that are capable of producing up to ± 300 kV at a rated current of 5 mA each. These hipots are typically used for insulation resistance testing of dielectric materials. Because of this, the hipot controller has a safety relay that trips the 300-kV power supply whenever an overload is detected (110 % of the rated current). Thus, to ensure continuous operation of the hipots for laser-triggered high voltage dischages, a capacitor bank is used instead, as schematically depicted in Fig. A.1. In this electrical circuit, ten 2-nF 40-kV "doorknob" ceramic capacitors have been connected in series to provide an effective capacitance $C =$ 0.2 nF. A $R_L = 60$ MΩ resistor is used to limit the load current of the hipot to 5 mA whenever an electrical breakdown occurs between the two electrodes. The maximum energy stored in each capacitor bank is $E = \frac{1}{2}CV^2 = 9$ Joules.

The capacitors and resistors are immersed in transformer oil to prevent any corona discharge. Fig. A.2 shows the container without the transformer oil. The base plate of the container is connected to a solid ground in the laboratory.

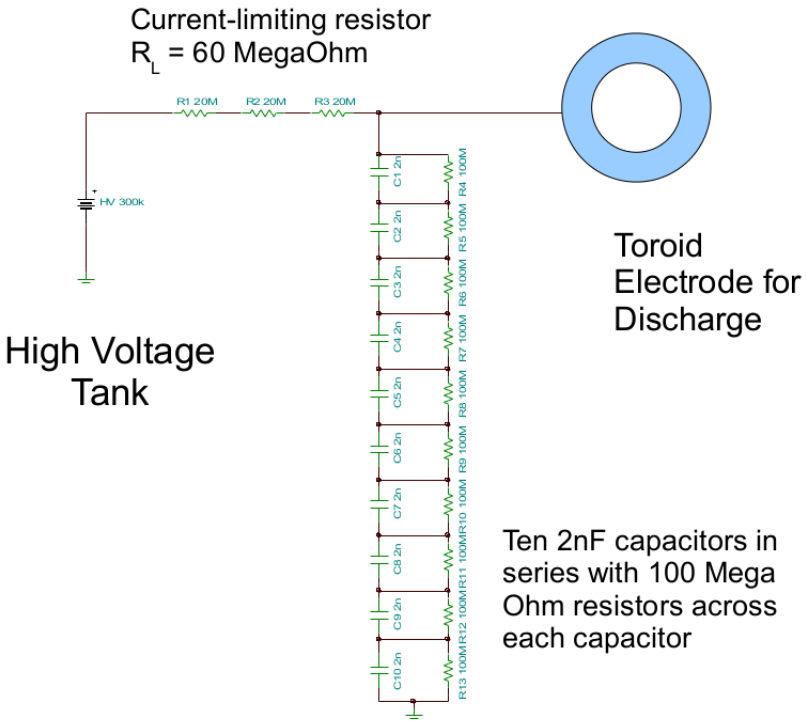

Figure A.1: Schematic of a capacitor bank charged by a 300-kV DC hipot.

Figure A.2: Container for the 300-kV capacitor bank.

A.1 Testing

After completing the construction of the ±300-kV DC capacitor bank (partially shown in Fig. A.3), we tested the system. The maximum voltage it produced without significant corona discharge is roughly ≈ ±250 kV DC. By bringing a grounded electrode to the high voltage electrode, an electrical breakdown can be initiated without tripping the 300-kV power supply as shown in Fig. A.4.

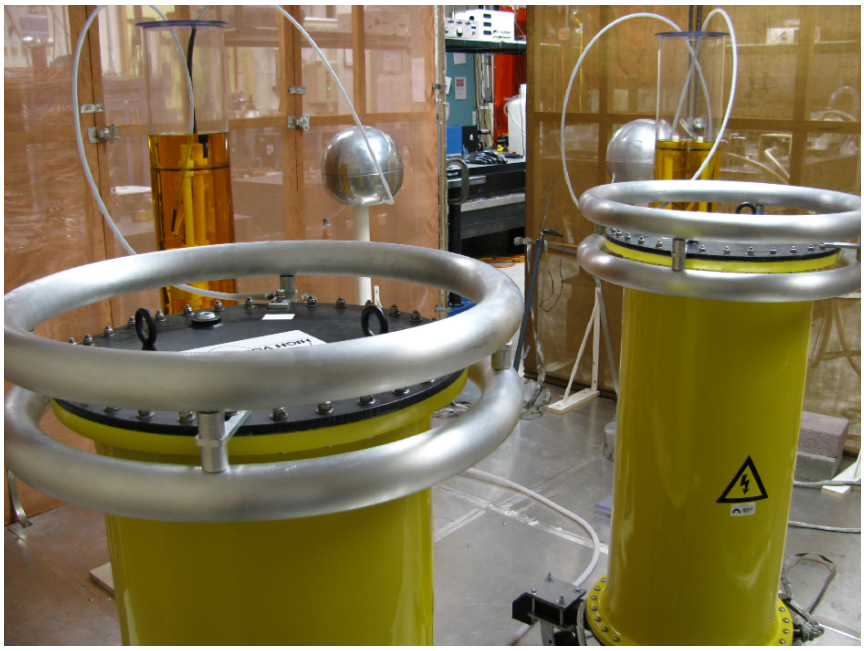

Figure A.3: 600kV discharge setup in the laboratory.

This 600-kV discharge setup is ready for long gap laser-induced high voltage discharges in the laboratory. It represents an improvement over the 200-kV DC discharge system built previously [39].

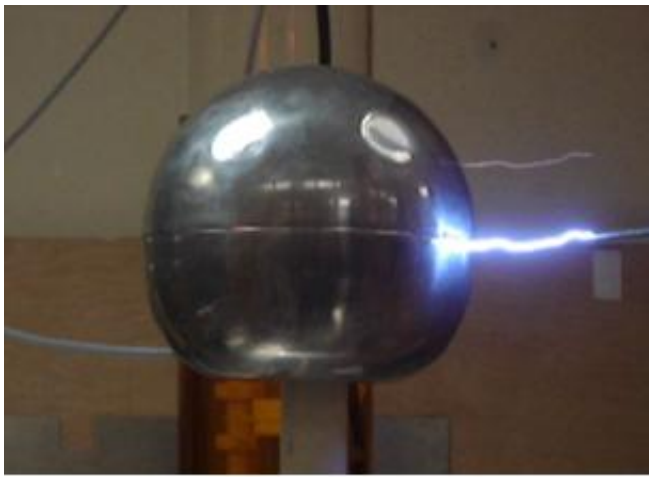

Figure A.4: Electrical discharge between a grounded rod and the high voltage spherical electrode.

Appendix B

Pulse Stretching with Alexandrite Laser

B.1 Motivation

Central to this research, intense laser pulses are used to ionize air with the ultimate goal of triggering lightning with lasers. We have seen in Chapters 3 and 4 that nitrogen fluorescence has been used to characterize the length of an optical filament. The nitrogen fluorescence within an optical filament stems from the following chemical processes:

$$N_2 + 10h\nu|_{(\lambda=800nm)} \rightarrow N_2^+(B^2\Sigma_u^+) + e^- \tag{B.1}$$

$$N_2^+(B^2\Sigma_u^+) \rightarrow N_2^+(X^2\Sigma_g^+) + h\nu|_{(\lambda=391nm)} \tag{B.2}$$

$$N_2^+ + N_2 \rightarrow N_4^+ \tag{B.3}$$

$$N_4^+ + e^- \rightarrow N_2(C^3\Pi_u) + N_2 \tag{B.4}$$

$$N_2(C^3\Pi_u) \rightarrow N_2(B^3\Pi_g) + h\nu|_{(\lambda=337nm)}. \tag{B.5}$$

The first negative system, $N_2^+(B \rightarrow X)$ is short-lived with a lifetime of roughly 0.35 ps in air while the second positive system $N_2(C \rightarrow B)$ is longer lived with a lifetime of 85 ps for a femtosecond laser filament in air [43].

Table B.1 shows the ionization potential and dissociation energy for both molecular nitrogen and oxygen [77]. It also provides the ionization potential for atomic nitrogen and oxygen. Clearly, oxygen has a lower ionization potential compared to nitrogen, requiring only 8 photons to ionize molecular oxygen compared to 10 photons for nitrogen at $\lambda = 800$ nm. Once an oxygen molecule is photoionized by a

Table B.1: Ionization potential and dissociation energy for nitrogen and oxygen [77].

	Molecular N_2	Molecular O_2
Ionization potential	15.58 eV	12.08 eV
No. of photons for ionization at $\lambda = 800$ nm = 1.55 eV	≥ 10	≥ 8
Dissociation energy	9.76 eV	5.12 eV
No. of photons for dissociation at $\lambda = 800$ nm = 1.55 eV	≥ 7	≥ 4
	Atomic N	Atomic O
Ionization potential	14.53 eV	13.62 eV
No. of photons for ionization at $\lambda = 800$ nm = 1.55 eV	≥ 10	≥ 9

femtosecond laser pulse, there are multiple chemical pathways for it to relax to the ground state. The positive molecular oxygen can react with nitrogen molecules to form nitric oxide. A more comprehensive list of reactions of positive nitrogen and

oxygen ions can be found in [77, 78]. In the following, we will simply limit our discussion of the reaction of oxygen species to those described in Table 2 upon the initial multiphoton ionization of the oxygen molecule by the femtosecond laser pulse at $\lambda = 800$ nm:

$$O_2 + 8h\nu \rightarrow O_2^+ + e^- \tag{B.6}$$

Table B.2: Important reaction processes involving oxygen in air after multiphoton ionization process. (T is temperature in Kelvin.)

Reaction	Rate coefficient, k
$e^- + O_2^+ \rightarrow O + O(^1D)$	2.1 x 10^{-7} $(\frac{300}{T})^{0.63}$ cm^3/s
$e^- + O + O_2^+ \rightarrow O^- + O_2$	10^{-31} cm^6/s
$e^- + O + O_2^+ \rightarrow O + O_2^-$	10^{-31} cm^6/s
$O_2^- + O \rightarrow O_3 + e^-$	1.5 x 10^{-10} cm^3/s
$O_2^- + O_2(a) \rightarrow O_2 + O_2 + e^-$	2 x 10^{-10} cm^3/s
$O_2^- + O_2(b) \rightarrow O_2 + O_2 + e^-$	3.6 x 10^{-10} cm^3/s
$O_2^- + N_2(A) \rightarrow O_2 + N_2 + e^-$	2.1 x 10^{-9} cm^3/s
$O_2^- + N_2(B) \rightarrow O_2 + N_2 + e^-$	2.5 x 10^{-9} cm^3/s
$O_2^- + N \rightarrow NO_2 + e^-$	5 x 10^{-10} cm^3/s
$O^- + O \rightarrow O_2 + e^-$	5 x 10^{-10} cm^3/s
$O^- + O_2(a) \rightarrow O_3 + e^-$	3 x 10^{-10} cm^3/s
$O^- + O_2(b) \rightarrow O_3 + e^-$	6.9 x 10^{-10} cm^3/s
$O^- + N_2(A) \rightarrow O + N_2 + e^-$	2.2 x 10^{-9} cm^3/s
$O^- + N_2(B) \rightarrow O + N_2 + e^-$	1.9 x 10^{-9} cm^3/s
$O^- + N \rightarrow NO + e^-$	2.6 x 10^{-10} cm^3/s
$O^- + O_2 \rightarrow O_3 + e^-$	5 x 10^{-15} cm^3/s
$O^- + NO \rightarrow NO_2 + e^-$	2.6 x 10^{-10} cm^3/s

To overcome the electron recombination and attachment processes, a solution has been proposed where a secondary laser beam is used to maintain the free electrons, keeping the electrons that have been liberated by the primary laser pulse (i.e., the femtosecond pulse) energetic. Since the electron affinity E_A is 1.46 eV for atomic oxygen, the secondary laser beam should have a photon energy greater than E_A, or its wavelength $\lambda \leq 843$ nm. (The electron affinity E_A for molecular oxygen is only 0.44 eV, and thus, the detachment of the electron from O_2^- can be achieved by heating the plasma instead of photodetachment using a secondary laser.) Based on the wavelength criterion, an alexandrite laser with central wavelength $\lambda = 755$ nm has been proposed as a secondary laser for the photodetachment of electrons from O^-. Furthermore, if the output pulse from the alexandrite laser is stretched, these energetic electrons can gain further kinetic energy from the laser electric field through inverse bremsstrahlung to knock off even more electrons from O_2^-, ensuring a steady growth of the free electrons for a long-gap high voltage discharge.

B.2 Alexandrite Laser

The alexandrite crystal is chromium-doped chrysoberyl ($BeAl_2O_4$:Cr^{3+}) and was first developed in 1980 by J. C. Walling *et al.* [79]. Table B.3 compares some of physical properties of the alexandrite crystal to those of ruby and Nd:YAG laser crystals [80], and it shows that the alexandrite laser can be Q-switched just like the Nd:YAG laser and can be pumped at higher average powers than the Nd:YAG because of its higher thermal conductivity.

It is also worth pointing out that the alexandrite crystal is orthorhombic and thus, it is a biaxial crystal. The highest gain is achieved when the electric field of the laser E is aligned parallel with respect to the b axis of the crystal (having a gain that is 10 times larger than other crystal orientation [80]). To ensure best performance

Table B.3: Properties of alexandrite, ruby and Nd:YAG laser crystals at $T = 300$ K [80].

Physical Property	Alexandrite	Ruby	Nd:YAG
Laser wavelength, λ (nm)	700–818	692.9, 694.3	946, 1064, 1839
Stimuated emission cross section (cm^{-3})	1 x 10^{-20}	2.5 x 10^{-20}	(2.8–6.5) x 10^{-20}
Spontaneous lifetime (μs)	260	3000	230
Thermal conductivity (W/cm-K)	0.23	0.251	0.14

of the laser, it is very important to align the alexandrite crystal in such a way that the output of a He-Ne laser with p-polarization experiences the most absorption propagating through the crystal.

The alexandrite laser can either operate as a three-level laser or a four-level vibronic laser system, as depicted schematically in Fig. B.1. In the three-level laser scheme, the chromium ions are pumped into the $^4T_2$ state and quickly relax into the ^2E state. Lasing occurs from ^2E to the ground state $^4A_2$ at a wavelength $\lambda = 680$ nm. This lasing transition is very similar to ruby ($\lambda = 694$ nm), and the difference in the emission wavelength is simply due to the slightly different host crystal: Al_2O_3 for ruby and $BeAl_2O_4$ for alexandrite. However, at room temperature, the absorption and fluorescence cross section σ of the alexandrite at $\lambda = 680$ nm are comparable ($\sigma =$ 2.9 x 10^{-19} cm^2 for absorption and $\sigma =$ 2.3 x 10^{-19} cm^2 for fluorescence for electric field E parallel with the b-axis of the crystal, $E \parallel b$ [79]). Because of the strong absorption line at $\lambda = 680$ nm, the three-level lasing efficiency of an alexandrite laser is very low. For four-level lasing with the alexandrite laser, the chromium ions

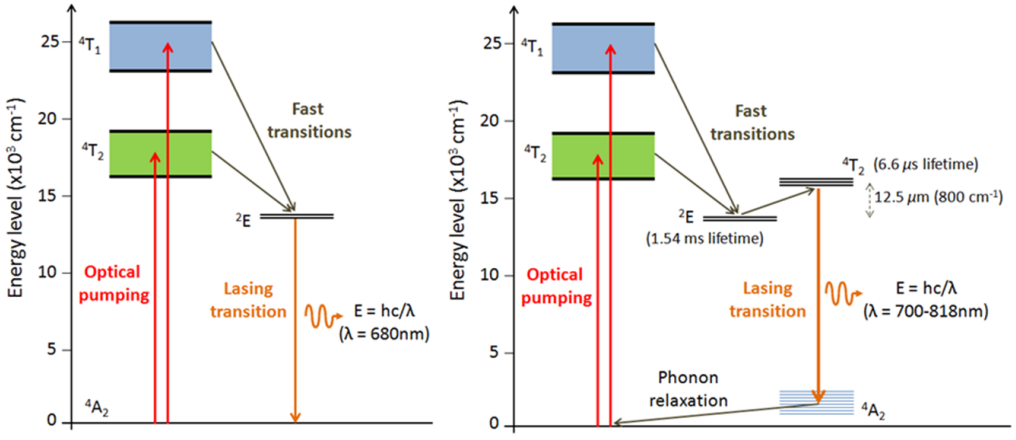

Figure B.1: Energy level diagram for Cr^{3+} in alexandrite for 3- (*left*) and 4-level (*right*) lasing (not drawn to scale).

further excited from the ^2E level to the $^4T_2$ vibronic states since the ^2E state has a long lifetime ($\tau_f = 1.54$ ms). Lasing action occurs at $^4T_2 \rightarrow ^4A_2$. Depending on the final vibronic state within the $^4A_2$ continuum, the emitted photon is accompanied by a phonon so that the Cr^{3+} chromium ion returns to its ground state. Thus, the alexandrite laser wavelength is determined by the lasing action between the vibronic states in $^4T_2$ and in $^4A_2$.

Since the difference in the energy level between the $^4T_2$ and ^2E states is not very large, the $^4T_2$ state can be increasingly populated by ^2E at higher temperatures. Thus, the alexandrite laser exhibits a higher gain at higher temperatures for the same input pump power. However, raising the temperature will also cause the higher vibronic states in $^4A_2$ to be more populated. This will result in the drop of overall lasing efficiency. Furthermore, increasing the operating temperature of the laser will reduce the overall fluorescence lifetime because $^4T_2$ has a shorter lifetime than ^2E, lowering the overall gain of the laser. In the alexandrite laser system that has been built at the University of New Mexico, the operating temperature of the alexandrite crystal is set at 80 °C. Thus, two water cooling systems are needed in the alexandrite:

one is used to cool the flashlamps while the other is used to heat up the alexandrite laser rod.

B.3 Feedback Design for Pulse Stretching Using a Q-Switched Alexandrite Laser

B.3.1 Q-Switch Operation

Q-switching a laser provides a means to generate giant pulses from a laser. This technique involves changing the quality factor, also known as the Q, of the laser resonator. The Q of the resonator can be defined as the ratio of the energy stored in the resonator to the power dissipated from the resonator per unit frequency ω_0 [80]:

$$Q = 2\pi \left[1 - \exp\left(\frac{-T_0}{\tau_c}\right)\right]^{-1} \approx \frac{2\pi\tau_c}{T_0} = 2\pi\nu_0\tau_c \tag{B.7}$$

where τ_c is the decay time constant of the radiation at angular frequency $\omega_0 = 2\pi\nu_0 = 2\pi/T_0$. This decay time constant can be defined as the average lifetime of the photons in the resonator.

In a typical flashlamp-pumped Q-switched laser as illustrated in Fig. B.2, a combination of a Pockels cell (PC) and a polarizing beamsplitter (PBS) is used to alter the Q of the resonator. The polarizing beamsplitter is set to allow p-polarization to pass through while rejecting s-polarization. Typically, a quarter-wave ($\lambda/4$) voltage is applied to the Pockels cell so that the initial p-polarization will be rotated to s-polarization after passing the Pockels cell twice (to and fro). Under this circumstance, lasing is prohibited because the loss in the resonator is so high. Nevertheless, energy is continuously stored in the gain medium until the upper lifetime of the gain medium is reached. At this moment, the quarter-wave voltage on the Pockels cell is removed so that the high Q of the resonator is restored, and lasing occurs. Because

of the stored energy in the laser gain medium, the resulting laser pulse has a high pulse energy (and hence, it is called a giant pulse). Depending on the lifetime of the upper level and the gain of the laser medium, the Q-switched laser pulses can be as short as a few nanoseconds. All the energy stored is switched out in a relatively short amount of time.

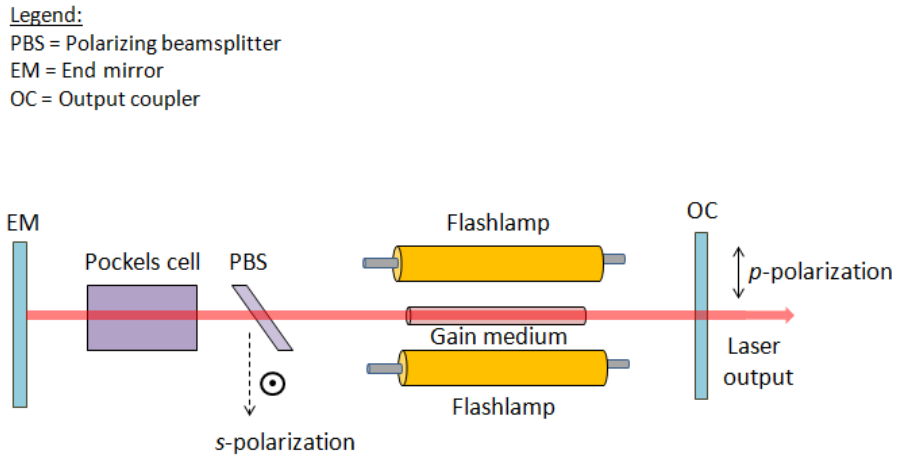

Figure B.2: Typical flashlamp-pumped Q-switched laser components.

B.3.2 Feedback Control for Pulse Stretching of a Q-Switched Alexandrite Laser

Depending on the lifetime of the upper level and the gain of the laser medium, the Q-switched laser pulses can be as short as a few nanoseconds. All the energy stored is switched out in a relatively short amount of time. While this allows us to achieve high energy pulses (up to 1 J of pulse energy in a few nanoseconds, or hundreds of megawatts of peak power), longer pulses are still needed to prolong the free electron lifetime for long gap discharges, and also to reduce the risk of optical damage in the laser components at high peak powers. For this purpose, a pulse

stretching scheme has been developed for the alexandrite laser, and it is based on the compound feedback designed for a ruby laser [81].

The principal idea behind this design is that the photon flux generated from the Q-switched laser pulse can be used to change the potential difference applied across a Pockels cell (see Fig. B.3), and thus, alter the Q of the cavity when the giant laser pulse is being formed. By connecting a vacuum photodiode to the negative electrode of the Pockels cell (PC), a current is induced whenever a light is detected by the photodiode, thereby reducing the effective potential difference across the PC. A vacuum photodiode (ITT FW114A) is used because it can handle the high voltage requirement to offset the quarter-wave voltage of the KD*P Pockels cell where the DC quarter-wave voltage at $\lambda = 755$ nm is 2.4 kV. (Newer silicon photodiodes do not produce sufficient voltage to affect the Q-switch operation of the Pockels cell. These silicon photodiodes only generate up to 12 Vdc, and high speed amplifiers are, thus, needed to increase the voltage level.)

Following the analysis found in [81], the rate of growth of photon density can be written as:

$$\frac{d\phi}{dt} = \frac{1}{t_l}(\alpha_0 n l - \gamma)\phi \tag{B.8}$$

where ϕ is the normalized photon density with $\phi = \Phi/N_0$, N_0 is the density of Cr^{3+} in the alexandrite crystal, α_0 is the absorption coefficient of the alexandrite, t_l is the time to traverse the resonator length l, γ is the fractional loss of photons for each traverse through the resonator, and n is the fractional population inversion given by $n = (N_2 - N_1)/N_0$. N_2 is the density of Cr^{3+} in the excited state while N_1 is the density of Cr^{3+} in the ground state. This equation has to be solved simultaneously with the decay rate of the population inversion given by:

$$\frac{dn}{dt} = -\frac{2\alpha_0 l}{t_L} n\phi \tag{B.9}$$

where the factor of two indicates a roundtrip (or twice the traverse length) in the

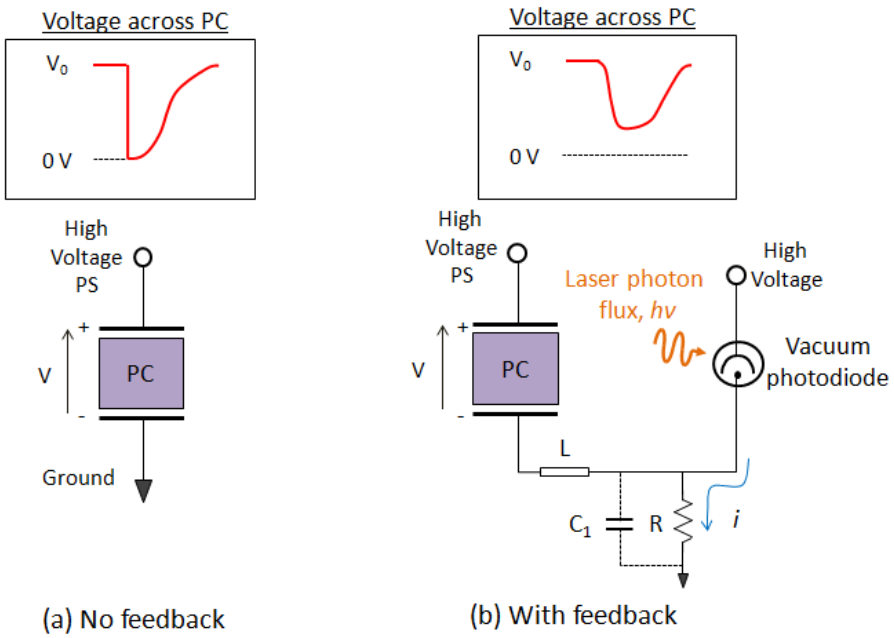

Figure B.3: Pockels cell operation: (a) Without feedback; (b) With feedback where V_0 is the quarter-wave ($\lambda/4$) voltage.

resonator.

In the design of the feedback control for pulse stretching, the fractional loss term γ consists of constant loss term γ_c (due to mirror transmission, i.e., from the output coupler having a reflectivity of R_{oc}) and also due to feedback from the vacuum photodiode $\gamma(\phi)$:

$$\gamma = \gamma_c + \gamma(\phi) \tag{B.10}$$

where $\gamma_c = -\ln(1-T_{oc}) = -\ln R_{oc}$. Assuming that the vacuum photodiode generates an output current i that is proportional to the laser photon flux, i.e., $i = M\phi$ and M is the proportionality constant, the induced voltage V can be written as:

$$V = iR = MR\phi. \tag{B.11}$$

We know that the transmission T of the Pockels cell is:

$$T = \cos^2\left(\frac{\pi}{2}\frac{V}{V_0}\right) \tag{B.12}$$

where V_0 is the DC quarter-wave voltage of the Pockels cell. Thus, the loss term due to Pockels cell feedback can be written as:

$$\gamma(\phi) = -\ln\left[\cos^2\left(\frac{\pi}{2}\frac{V}{V_0}\right)\right]. \tag{B.13}$$

Finally, we must include any delay in the rise of the induced current stemming from the shunt capacitance C of the vacuum photodiode, as schematically depicted in Fig. B.3(b). Since the shunt capacitance C must be charged before a voltage can appear at the negative terminal of the Pockels cell, it follows from Kirchoff's current law:

$$M\phi = C\frac{dV}{dt} + \frac{V}{R}. \tag{B.14}$$

The stray series inductance L can be neglected since the connections are short.

B.3.3 Modeling the Simple Feedback Circuit

Based on the analysis above, the Q-switching of an alexandrite laser has been modeled. Here, we take the cavity length l_c = 66.8 cm, the absorption coefficient of alexandrite α_0 = 0.25 cm^{-1} = 25 m^{-1}, and the length of the alexandrite rod L_{rod} = 12.78 cm. In our modeling, the output coupler has a reflectivity R_{oc} = 82 %. We set the resistance R = 1020 Ω and capacitance C = 4 pF along with fractional population inversion $n(t = 0)$ = 0.5 and initial normalized photon density $\phi(t = 0)$ = 10^{-3}.

Fig. B.4 shows the Q-switched pulse from the alexandrite laser when $M = 0$ (no feedback). In this case, the full width half maximum (FWHM) pulse duration is τ = 30 ns.

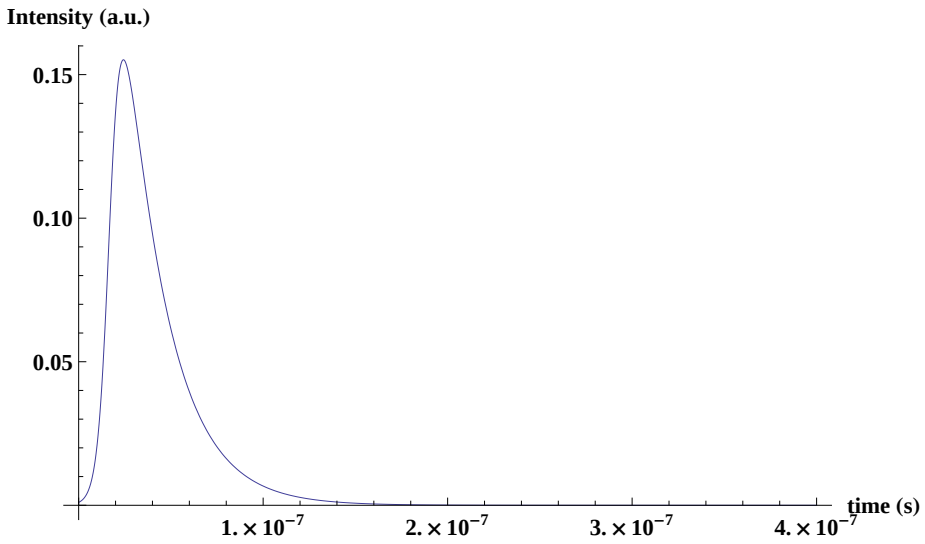

Figure B.4: Q-switched pulse from an alexandrite laser with no feedback ($M = 0$).

To analyze the behavior of the stretched pulse from a Q-switched alexandrite laser using the simple feedback circuit, we set $M = 1000$. This number is arbitrarily set, and it represents the amplification gain of the current coming from the vacuum photodiode. Experimentally, this gain can be increased/reduced by increasing/reducing the applied voltage across the vacuum photodiode. Fig. B.5 displays the stretched pulse from a Q-switched alexandrite laser with the simple feedback circuit. We see that the after the initial spike there is a slow exponential decay of the photon flux: The FWHM pulse duration $\tau = 50$ ns, after which the pulse monotonically decays down close to zero after 400 ns.

B.3.4 Compound Feedback for Pulse Stretching

Although the Q-switched laser pulse has been temporally stretched from 13 ns to 50 ns (FWHM) using the simple feedback circuit, a longer pulse duration is needed for the maintenance of free electrons for long discharge gaps. Preferably, the temporal

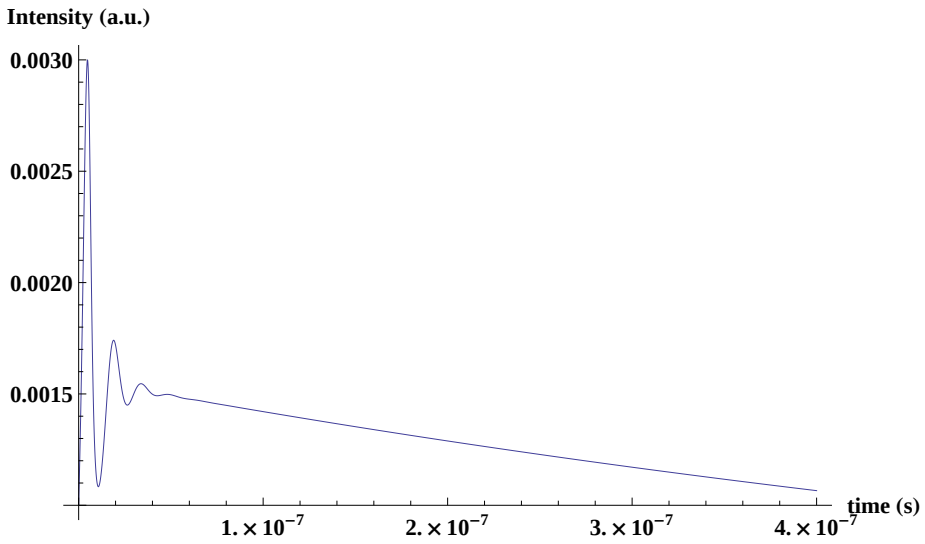

Figure B.5: Temporally stretched pulse from a Q-switched alexandrite laser ($M = 1000$).

shape of the pulse should be rectangular. Otherwise, the intensity of the trailing part of the pulse quickly falls below the threshold needed to keep the electrons energetic in the laser plasma. To achieve this, a compound feedback circuit for the alexandrite has been devised as shown in Fig. B.6. C_1 represents the capacitance of the Pockels cell. In Fig. B.6, Kirchoff's current law dictates that at node V_1:

$$i_0 = i_1 + i_2 + i_3 \tag{B.15}$$

with

$$i_0 = M\phi(t) \tag{B.16}$$

$$i_1 = C_1 \frac{dV_1}{dt} \tag{B.17}$$

$$i_2 = \frac{V_1}{R_1} \tag{B.18}$$

$$i_3 = C_2 \frac{dV_2}{dt} \tag{B.19}$$

$$V = V_1 - V_2 = L_1 \frac{di_3}{dt}. \tag{B.20}$$

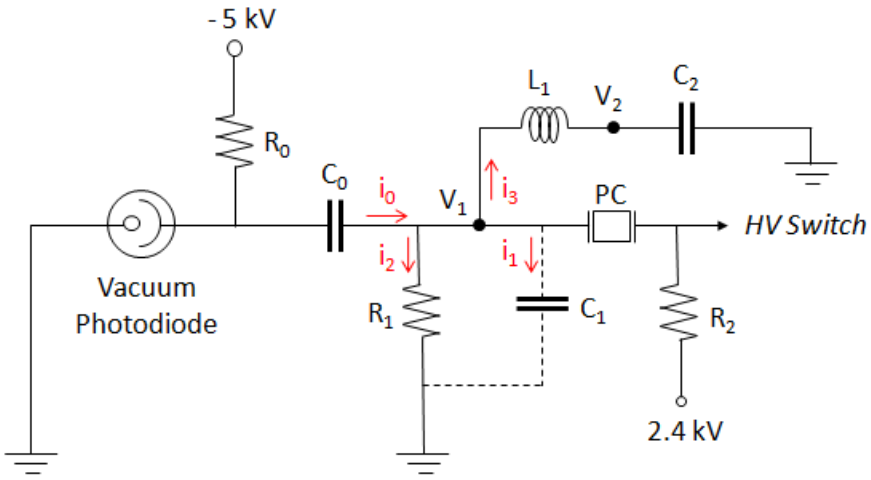

Figure B.6: Compound feedback circuit for pulse stretching.

Inserting Eqs. B.16–B.20 into Eq. B.15 and upon rearranging, we obtain

$$\frac{dV_2}{dt} = \frac{M}{C-2}\phi(t) - \frac{C_1}{C_2}\frac{dV_1}{dt} - \frac{V_1}{R_1 C_2}. \tag{B.21}$$

Differentiating Eq. B.19 with respect to t,

$$\frac{di_3}{dt} = C_2 \frac{d^2V_2}{dt^2}. \tag{B.22}$$

Solving Eqs. B.20 and B.22 simultaneously,

$$\frac{d^2V_2}{dt^2} = \frac{V_1 - V_2}{C_2 L_1}. \tag{B.23}$$

And differentiating Eq. B.21 once more, we arrive at

$$\frac{d^2V_2}{dt^2} = \frac{V_1 - V_2}{C_2 L_1} = \frac{M}{C_2}\frac{d\phi}{dt} - \frac{C_1}{C_2}\frac{d^2V_1}{dt^2} - \frac{1}{C_2 R_1}\frac{dV_1}{dt}. \tag{B.24}$$

Since $V = V_1 - V_2$ from Eq. B.20, Eq. B.24 can be rewritten as:

$$\frac{d^2V_1}{dt^2} + \frac{1}{R_1 C_1}\frac{dV_1}{dt} + \frac{V}{L_1 C_1} - \frac{M}{C_1}\frac{d\phi}{dt} = 0. \tag{B.25}$$

Eq. B.25 can now be solved along with the previous equations governing the growth of the laser photon flux in the cavity. As before:

$$\frac{d\phi}{dt} = \frac{1}{t_l}(\alpha_0 nl - \gamma)\phi \tag{B.26}$$

$$\frac{dn}{dt} = -\frac{2\alpha_0 l}{t_l} n\phi \tag{B.27}$$

$$\gamma(\phi) = -\ln(1 - T_{oc}) - \ln\left[\cos^2\left(\frac{\pi}{2}\frac{V}{V_0}\right)\right]. \tag{B.28}$$

Fig. B.7 shows the simulation results based on the compound feedback circuit shown in Fig. B.6 with the following values: $R_1 = 1020\ \Omega$, $C_1 = 4$ pF, $C_2 = 50$ pF, $L_1 = 1.2$ mH. The FWHM pulse duration is $\tau = 210$ ns, which is roughly four times longer than the stretched pulse from the simple feedback circuit above.

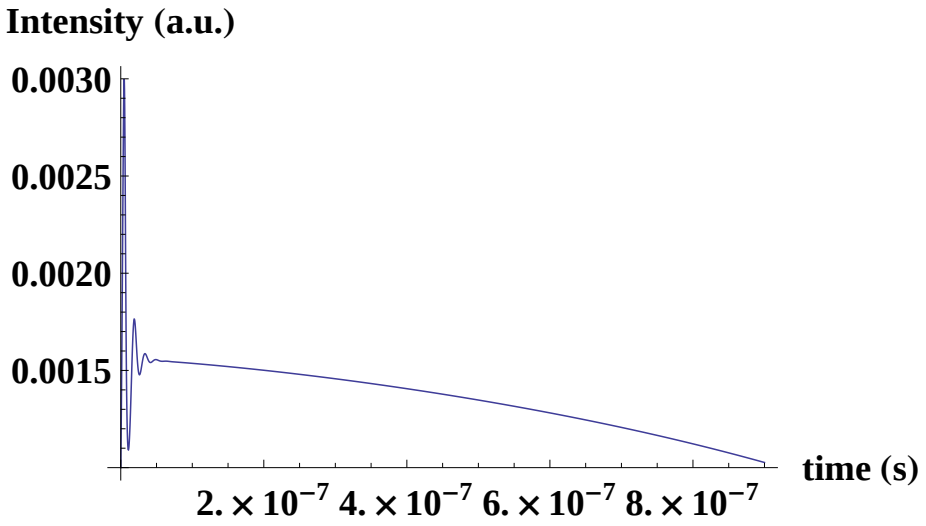

Figure B.7: Pulse stretching from a Q-switched alexandrite laser with compound feedback circuit.

B.3.5 Experimental Results

Based on the simulation results, a pulse stretcher based on the compound feedback circuit was built for the alexandrite laser. The overall circuit is shown in Fig. B.8. An avalanche circuit switch is used to trigger the Pockels cell (PC). It receives an external trigger from the delay generator to change the Q of the laser cavity. Typically, the time delay is set to ≈ 200 μs after the flashlamp is fired. The avalanche switching circuit will be described in further in the next section.

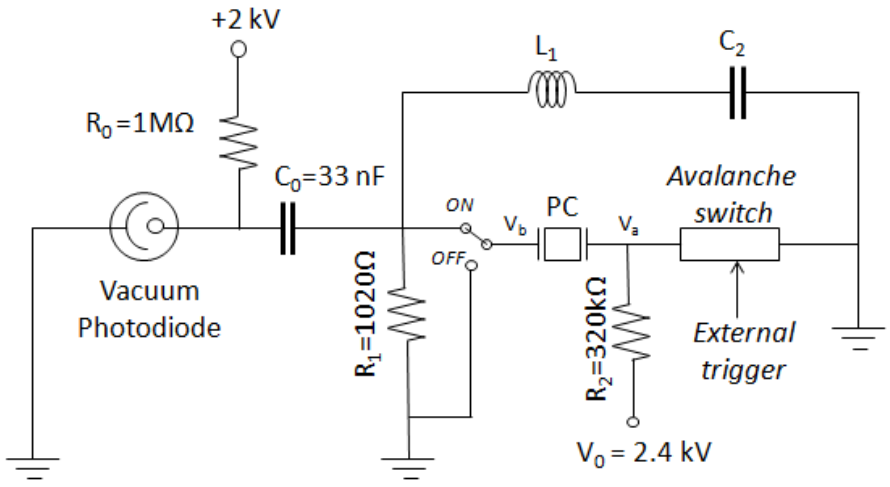

Figure B.8: Compound feedback circuit with an avalanche switch.

When the switch is in the OFF position, the voltage across the Pockels cell is $V = V_a - V_b = V_0$, the quarter-wave voltage of the Pockels cell. As long as the avalanche switch is not triggered, this quarter-wave voltage remains and no lasing occurs because the loss in the cavity is greater than the gain. This allows the population inversion to build up in the alexandrite gain medium. Once maximum population inversion is reached, an external trigger is applied to the avalanche switch bringing the potential V_a to ground, causing a zero voltage across the Pockels cell. At this instant, the loss in the cavity is reduced to zero and Q-switching of the laser

occurs. Fig. B.9 shows the pulse width of a Q-switched alexandrite laser with the compound feedback circuit turned off. The FHWM pulse duration is $\tau = 150$ ns.

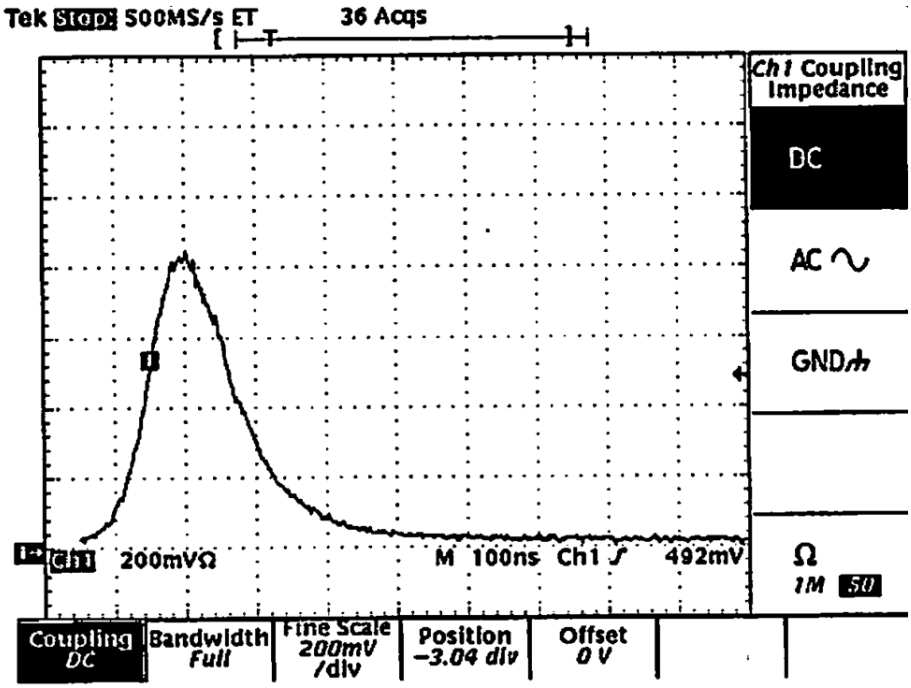

Figure B.9: Pulse duration of an alexandrite laser with the compound feedback circuit turned off. The FWHM pulse duration $\tau = 150$ ns.

If the compound feedback circuit is turned on, an induced voltage appears at V_b due to the photon flux of the alexandrite laser pulse incident on the vacuum photodiode. This changes the voltage across the Pockels cell causing a time-dependent change in the loss/gain of the cavity. Fig. B.10 shows the temporally stretched alexandrite laser pulse when the compound feedback circuit is turned on. Although the pulse displays two peaks, the FWHM pulse duration $\tau = 500$ ns. The apparent discrepancy in the pulse shape can be attributed to the uncertainty in determining the exact value of the proportionality constant M that is used in the simulation, and also to the doping concentration of the Cr^{3+} ions in the alexandrite laser rod. For example, by increasing the value of M from 1000 to 7000, and the initial value of

$\phi(0)$ from 1 x 10^{-3} to 4 x 10^{-3}, a rectangular pulse shape with a FWHM width of τ = 425 ns is obtained from the modeling, as shown in Fig. B.11.

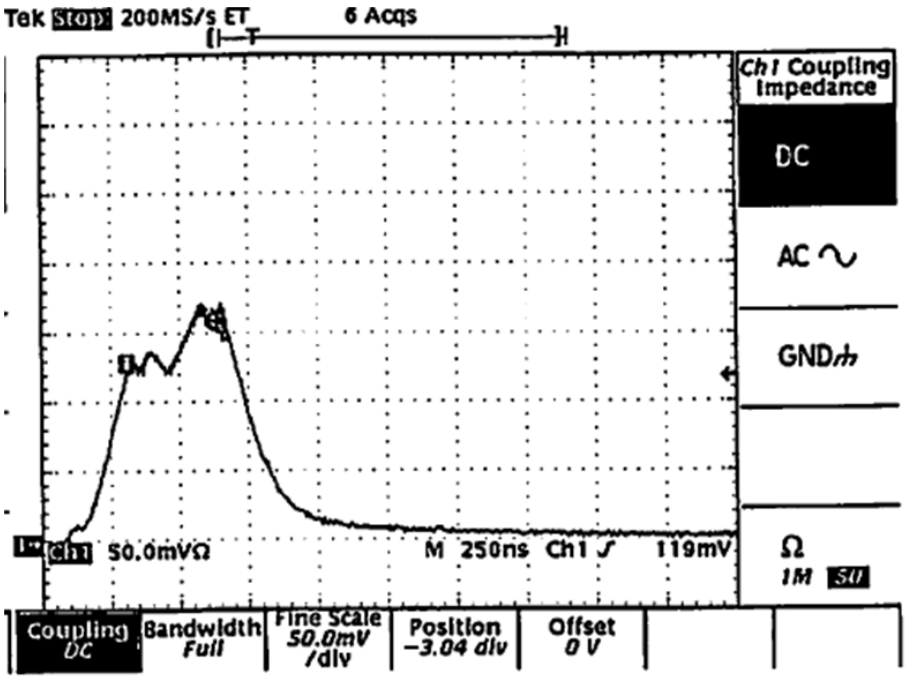

Figure B.10: Pulse duration of an alexandrite laser with the compound feedback circuit turned off. The FWHM pulse duration τ = 500 ns.

B.4 High Voltage Trigger Circuit for Pockels Cell

A high voltage trigger circuit has also been built for the Pockels cell that is used to Q-switch the alexandrite laser. This trigger circuit is based on the avalanche operation of the NPN bipolar junction transistor 2N5551 [82]. The 2N5551 has a breakdown voltage $V_{br} \approx$ 320 V. Thus, the minimum number of NPN transistors needed to maintain the quarter-wave voltage of the Pockels cell (V_0 = 2.4 kV) is 8 when stacked in series, as shown in Fig. B.12.

When the circuit is not triggered, no current flows through the 2N5551 transistors.

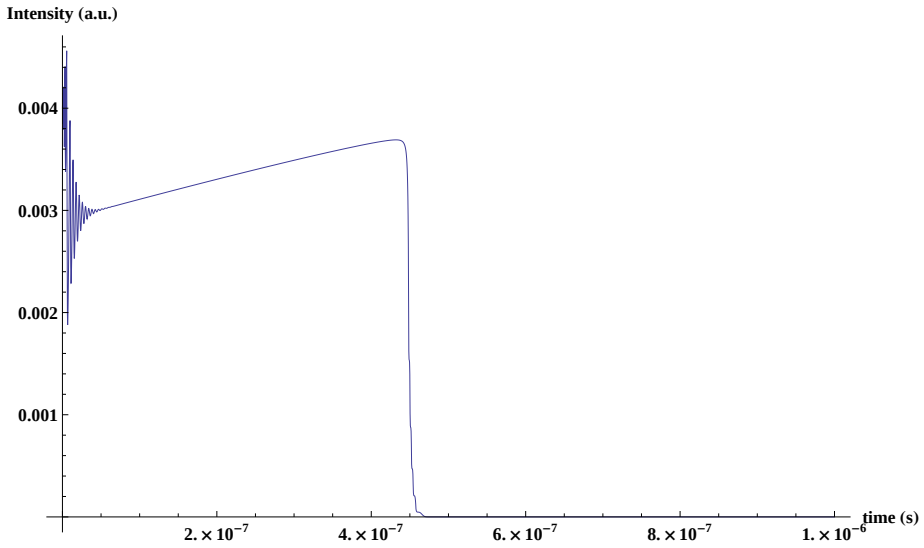

Figure B.11: Rectangular pulse shape with a slow increase in intensity before a sudden decrease at $t = 425$ ns ($M = 7000$ and $\phi(0) = 4$ x 10^{-3}).

V_0 appears at the output ($V_{out} = V_0$), and the voltage across each transistor is exactly $V_0/8 = 300$ V $< V_{br}$ because of the R_2 voltage divider resistors. When a TTL trigger signal is applied to the first transistor Q_1, the voltage across Q_1 quickly becomes zero because the initial voltage of 300 V is larger than the rated collector-base voltage V_{CBO}. This causes an avalanche breakdown in the reverse-biased p-n junction. At this instant, the remaining transistors (Q_2 through Q_8) experience a sudden increase in voltage greater than V_{br}, i.e. the voltage is now $V_0/7 = 343$ V, causing simultaneous avalanche breakdown in all the transistors. Consequently, the breakdown current flows through the transistors, resulting in the grounding of the output of the high voltage switch. In the case of the Pockels cell, the quarter-wave voltage is removed from the terminal of the Pockels cell and lasing occurs. The fall time of the HV pulse has been measured to be less than 100 ns, as shown in Fig. B.13.

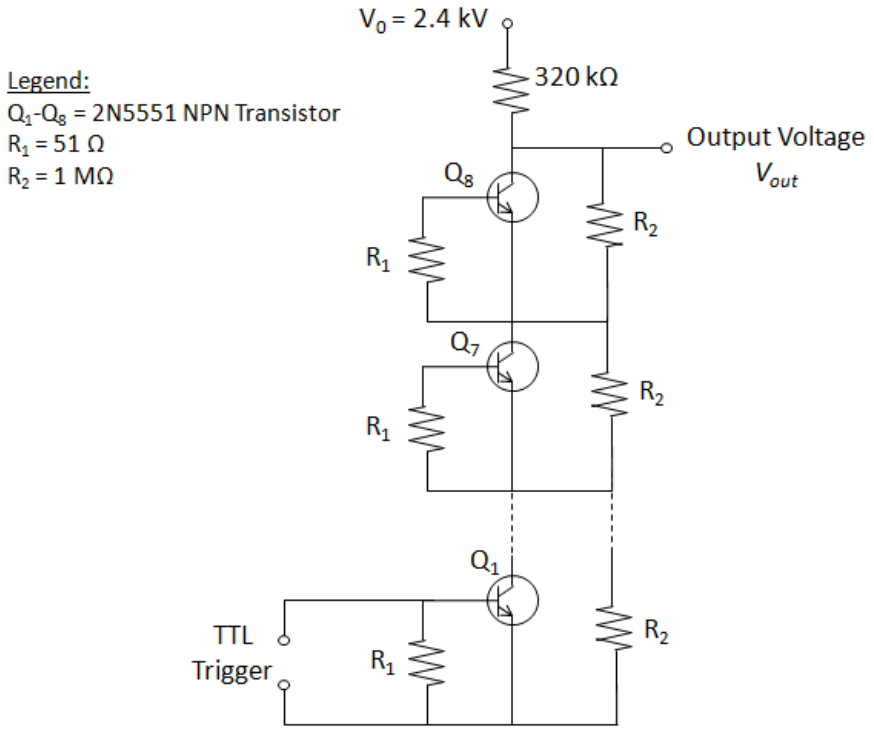

Figure B.12: Avalanche circuit using avalanche operation mode of 2N5551 NPN transistors.

B.5 Future Work

We have demonstrated pulse stretching of a Q-switched alexandrite laser from $\tau =$ 150 ns to $\tau = 500$ ns using a compound feedback scheme. Typical output pulse energies from this laser range from 375–400 mJ when the flashlamps are pumped at 1.9 kV. To obtain higher pulse energies, an amplifier stage can be added to this alexandrite laser, as shown in Fig. B.14. The output of the seed laser is p-polarized and passes through a thin film polarizer and a wave plate before it is further amplified in the flashlamp-pumped alexandrite. The wave plate can either be quarter-wave plate or a Faraday rotator. In the case of a quarter-wave plate, the pulse is circularly polarized when passing through the amplifier crystal. After emerging from amplifier

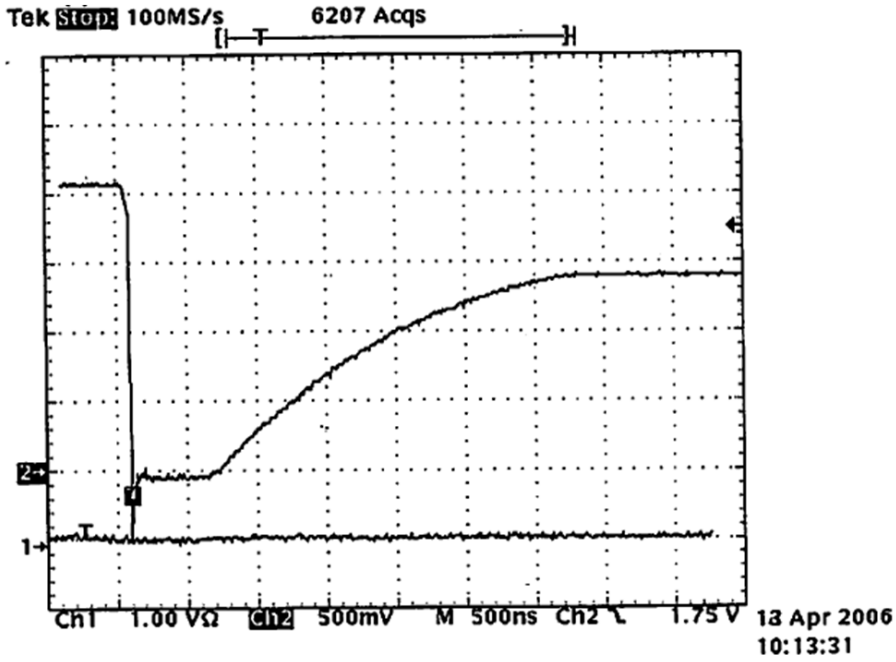

Figure B.13: Voltage at the output of the avalanche circuit (shown as Channel 2) measured by a 1000:1 high voltage probe with a fall time of less than 100 ns.

crystal and through the quarter-wave plate, the beam becomes s-polarized and is reflected off the thin film polarizer. Alternatively, the wave plate can be replaced by a Faraday rotator that rotates the linear polarization by 45 °. After bouncing off the end mirror and through the alexandrite crystal and Faraday rotator the second time, the emerging beam is s-polarized and will be reflected off the thin film polarizer.

Although in both cases the polarization of the emerging beam is s, the gain in the double pass amplifier will be different since the alexandrite laser crystal is biaxial and exhibits the strongest absorption when the electric field is parallel to the b-axis of the crystal. To exploit this gain, both the flashlamps and alexandrite rod need to be positioned correctly (rotated by 45 °) for maximum amplification of the linearly polarized laser beam. This may be difficult in the current setup due to the enclosure of the laser head. Thus, by using a quarter-wave plate, the physical problem may be

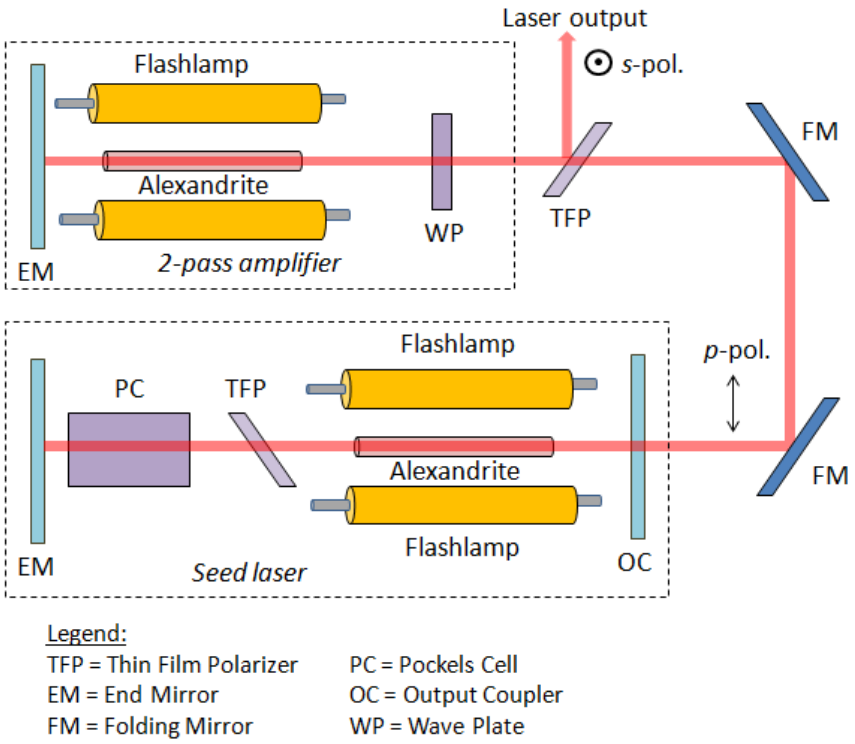

Figure B.14: Double pass amplifier seeded by an stretched Q-switched alexandrite laser.

circumvented, making the amplification process polarization independent although at a reduced gain factor. Nonetheless, using a circularly polarized beam is fairly common for the amplification of high energy laser pulses to prevent Kerr self-focusing in the gain medium. It is left to be explored in the future how much gain can be achieved by using either a quarter-wave plate or a Faraday rotator in the two-pass alexandrite laser amplifier.

References

[1] J. Kasparian, R. Sauerbrey, and S. L. Chin. The critical laser intensity of self-guided light filaments in air. *Appl. Phys. B*, 71:877–879, 2000.

[2] M. Hercher. Laser-induced damage in transparent media. *J. Opt. Soc. Am.*, 54(4):563, 1964.

[3] A. Braun, G. Korn, X. Liu, D. Du, J. Squier, and G. Mourou. Self-channeling of high-peak-power femtosecond laser pulses in air. *Opt. Lett.*, 20(1):73–75, 1995.

[4] X. M. Zhao, P. Rambo, and J.-C. Diels. Filamentation of femtosecond UV pulses in air. In *QELS*, Baltimore, MD, USA, 1995. Optical Society of America.

[5] L. V. Keldysh. Ionization in the field of a strong electromagnetic wave. *Sov. Phys. JETP*, 20(5):1307–1314, 1965.

[6] M. J. DeWitt and R. J. Levis. Calculating the Keldysh adiabaticity parameter for atomic, diatomic, and polyatomic molecules. *J. Chem. Phys.*, 108(18):7739–7742, 1998.

[7] X. M. Zhao, J.-C. Diels, C. Y. Yang, and J. Elizondo. Femtosecond ultraviolet laser pulse induced electrical discharges in gases. *IEEE J. Quantum Electron.*, 31(3):599–612, 1995.

[8] P. Rambo, J. Schwarz, and J.-C. Diels. High voltage electrical discharges induced by an ultrashort pulse UV laser system. *J. Opt. A*, 3(2):146–158, 2001.

[9] M. Rodriguez, R. Sauerbrey, H. Wille, T. Fujii, Y. B. Andre, A. Mysyrowicz, L. Klingbeil, K. Rethmeier, W. Kalkner, J. Kasparian, E. Salmon, J. Yu, and J.-P. Wolf. Triggering and guiding megavolt discharges by use of laser-induced ionized filaments. *Opt. Lett.*, 27(9):772–774, 2002.

[10] S. Skupin, L. Berge, U. Peschel, F. Lederer, G. Mejean, J. Yu, J. Kasparian, E. Salmon, J.-P. Wolf, M. Rodriguez, L. Woste, R. Bourayou, and R. Sauerbrey. Filamentation of femtosecond pulses in the air: Turbulent cells versus long-range clusters. *Phys. Rev. E*, 70(4):046602, 2004.

[11] E. T. J. Nibbering, P. F. Curley, G. Grillon, B. S. Prade, M. A. Franco, F. Salin, and A. Mysyrowicz. Conical emission from self-guided femtosecond pulses in air. *Opt. Lett.*, 21(1):62–64, 1996.

[12] S. L. Chin, H. L. Xu, Q. Luo, F. Theberge, W. Liu, J. F. Daigle, Y. Kamali, P. T. Simard, J. Bernhardt, S. A. Hosseini, M. Sharifi, G. Mejean, A. Azarm, C. Marceau, O. Kosavera, V. P. Kandidov, N. Akozbek, A. Becker, G. Roy, P. Mathieu, J. R. Simard, M. Chateauneuf, and J. Dubois. Filamentation "remote" sensing of chemical and biological agents/pollutants using only one femtosecond laser source. *Appl. Phys. B*, 95(1):1–12, 2009.

[13] K. Stelmaszczyk, P. Rohwetter, G. Mejean, J. Yu, E. Salmon, J. Kasparian, R. Ackermann, J.-P. Wolf, and L. Woste. Long-distance remote laser-induced breakdown spectroscopy using filamentation in air. *Appl. Phys. Lett.*, 85(18):3977–3979, 2004.

[14] J. Kasparian, M. Rodriguez, G. Mejean, J. Yu, E. Salmon, H. Wille, R. Bourayou, S. Frey, Y.-B. Andre, A. Mysyrowicz, R. Sauerbrey, J.-P. Wolf, and L. Woste. White-light filaments for atmospheric analysis. *Science*, 301(5629):61–64, 2003.

[15] G. Mejean, J. Kasparian, E. Salmon, J. Yu, J.-P. Wolf, R. Bourayou, M. Rodriguez, L. Woste, H. Lehmann, B. Stecklum, U. Laux, J. Eisloffel, A. Scholz, and A. P. Hatzes. Towards a supercontinuum-based infrared lidar. *Appl. Phys. B*, 77:357–359, 2003.

[16] H. Pepin, D. Comtois, F. Vidal, C. Y. Chien, A. Desparois, T. W. Johnston, J. C. Kieffer, B. La Fontaine, F. Martin, F. A. M. Rizk, C. Potvin, P. Couture, H. P. Mercure, A. Bondiou-Clergerie, P. Lalande, and I. Gallimberti. Triggering and guiding high-voltage large-scale leader discharges with sub-joule ultrashort laser pulses. *Phys. Plasmas*, 8(5):2532–2539, 2001.

[17] T. Fujii, M. Miki, N. Goto, A. Zhidkov, T. Fukuchi, Y. Oishi, and K. Nemoto. Leader effects on the femtosecond-laser-filament-triggered discharges. *Phys. Plasmas*, 15(1):013107, 2008.

[18] R. Ackermann, Y.-B. Andre, G. Mechain, G. Mejean, B. Prade, P. Rohwetter, E. Salmon, K. Stelmaszczyk, J. Yu, A. Mysyrowicz, R. Sauerbrey, L. Woste,

J.-P. Wolf, and J. Kasparian. Electric events synchronized with laser filaments in thunderclouds. *Opt. Express*, 16(8):5757–5763, 2008.

[19] J.-C. Diels and W. R. Rudolph. *Ultrashort Laser Pulse Phenomena*. Elsevier, Boston, 2nd edition, 2006.

[20] A. Couairon and A. Mysyrowicz. Femtosecond filamnetation in transparent media. *Phys. Rep.*, 441:47–189, 2007.

[21] A. Couairon, E. Gaizauskas, D. Faccio, A. Dubietis, and P. Di Trapani. Nonlinear X-wave formation by femtosecond filamentation in Kerr media. *Phys. Rev. E*, 73(1):016608, 2006.

[22] J. H. Marburger. Self-focusing: Theory. *Progr. Quantum Electron.*, 4(1):35–110, 1975.

[23] W. Liu and S. L. Chin. Direct measurement of the critical power of femtosecond Ti:sapphire laser pulse in air. *Opt. Express*, 13(15):5750–5755, 2005.

[24] S. L. Chin. *Femtosecond Laser Filamentation*. Springer, New York, 2010.

[25] K. D. Moll, G. Fibich, and A. L. Gaeta. Self-similar optical wave collapse: Observation of the Townes profile. *Phys. Rev. Lett.*, 90(20):203902, 2003.

[26] A. Brodeur, C. Y. Chien, F. A. Ilkov, S. L. Chin, O. G. Kosavera, and V. P. Kandidov. Moving focus in the propagation of ultrashort laser pulses in air. *Opt. Lett.*, 22(5):304–306, 1997.

[27] M. Mlejnek, E. M. Wright, and J. V. Moloney. Dynamic spatial replenishment of femtosecond pulse propagating in air. *Opt. Lett.*, 23(5):382–384, 1998.

[28] A. Dubietis, G. Tamosauskas, I. Diomin, and A. Varanavicius. Self-guided propagation of femtosecond light pulses in water. *Opt. Lett.*, 28(14):1269–1271, 2003.

[29] M. Kolesik, E. M. Wright, and J. V. Moloney. Dynamic nonlinear X waves for femtosecond pulse propagation in water. *Phys. Rev. Lett.*, 92(25):253901, 2004.

[30] A. Dubietis, E. Gaisauskas, G. Tamosauskas, and P. Di Trapani. Light filaments without self-channeling. *Phys. Rev. Lett.*, 92(25):253903, 2004.

[31] V. Loriot, E. Hertz, O. Faucher, and B. Lavorel. Measurement of higher order Kerr refractive index of major air components. *Opt. Express*, 17(16):13429–13434, 2009.

[32] P. Bejot, J. Kasparian, S. Henin, V. Loriot, T. Vieillard, E. Hertz, O. Faucher, B. Lavorel, and J.-P. Wolf. Higher-order Kerr terms allow ionization-free filamentation in gases. *Phys. Rev. Lett.*, 104(10):103903, 2010.

[33] B. C. Stuart, M. D. Feit, S. Herman, A. M. Rubenchik, B. W. Shore, and M. D. Perry. Optical ablation by high-power short-pulse lasers. *J. Opt. Soc. Am. B*, 13(2):459–468, 1996.

[34] J. Schwarz. *High Intensity Laser Pulse Propagation through the Atmosphere, Lightning Protection and Filamentation*. PhD thesis, University of Jena, 2003.

[35] J. Schwarz, J. Yeak, F. Holch, J.-C. Diels, W. H. Behrens, and K. Kremeyer. Aerodynamic window: Novel diagnostic tool to characterize filaments. In *Quantum Electronics and Laser Science (QELS), Postconference Digest*, page QTuG22. IEEE, 2003.

[36] D. J. Mirell. *Experimental Study of Infrared Filaments under Different Initial Conditions*. PhD thesis, University of New Mexico, 2009.

[37] E. M. Parmentier and R. A. Greenberg. Supersonic flow aerodynamic window for high-power lasers. *AIAA Journal*, 11(7):943–949, 1973.

[38] S. Couris, M. Renard, O. Faucher, B. Lavorel, R. Chaux, E. Koudoumas, and X. Michaut. An experimental investigation of the nonlinear refractive index (n_2) of carbon disulfide and toulene by spectral shearing interferometry and z-scan techniques. *Chem. Phys. Lett.*, 369:318–324, 2003.

[39] P. K. Rambo. *Laser-Induced Lightning*. PhD thesis, University of New Mexico, 2000.

[40] J.-C. Diels, J. Yeak, D. Mirell, R. Fuentes, S. Rostami, D. Faccio, and P. Di Trapani. Air filaments and vacuum. *Laser Phys.*, 20(5):1101–1106, 2010.

[41] S. Tzortzakis, M. A. Franco, Y. B. Andre, A. Chiron, B. Lamouroux, B. S. Prade, and A. Mysyrowicz. Formation of a conducting channel in air by self-guided femtosecond laser pulses. *Phys. Rev. E*, 60(4):3505–3507, 1999.

[42] S. A. Hosseini, Q. Luo, B. Ferland, W. Liu, N. Akozbek, G. Roy, and S. L. Chin. Effective length of filaments measurement using backscattered fluorescence from nitrogen molecules. *Appl. Phys. B*, 77:697–702, 2003.

[43] H. L. Xu, A. Azarm, J. Bernhardt, Y. Kamali, and S. L. Chin. The mechanism of nitrogen fluorescence inside a femtosecond laser filament in air. *Chem. Phys.*, 360:171–175, 2009.

[44] F. Martin, R. Mawassi, F. Vidal, I. Gallimberti, H. Pepin, J. C. Kieffer, and H. P. Mercure. Spectroscopic study of ultrashort pulse laser-induced breakdown plasmas in air. *Appl. Spectrosc.*, 56(11):1444–1452, 2002.

[45] R. W. Boyd. *Nonlinear Optics*. Academic Press, New York, 3rd edition, 2007.

[46] T. Fujii, N. Goto, M. Miki, T. Nayuki, and K. Nemoto. Lidar measurement of constituents of microparticles in air by laser-induced breakdown spectroscopy using femtosecond terawatt laser pulses. *Opt. Lett.*, 31(23):3456–3458, 2006.

[47] H. L. Xu, W. Liu, and S. L. Chin. Remote time-resolved filament-induced breakdown spectroscopy of biological materials. *Opt. Lett.*, 31(10):1540–1542, 2006.

[48] K. Guo, J. Lin, Z. Hao, Z. Gao, Z. Zhao, C. Sun, and B. Li. Triggering and guiding high-voltage discharge in air by single and multiple femtosecond filaments. *Opt. Lett.*, 37(2):259–261, 2012.

[49] T. Leisner, D. Duft, O. Mohler, H. Saathoff, M. Schnaier, S. Henin, K. Stelmaszczyk, M. Petrarca, R. Delagrange, Z. Hao, J. Luder, Y. Petit, P. Rohwetter, J. Kasparian, J.-P. Wolf, and L. Woste. Laser-induced plasma cloud interaction and ice multiplication under cirrus cloud conditions. *Proc. Nat. Acad. Sci. USA*, 110(25):10106–10110, 2013.

[50] L. Berge, S. Skupin, F. Lederer, G. Mejean, J. Yu, J. Kasparian, E. Salmon, J.-P. Wolf, M. Rodriguez, L. Woste, R. Bourayou, and R. Sauerbrey. Multiple filamentation of terawatt laser pulses in air. *Phys. Rev. Lett.*, 92(22):225002, 2004.

[51] W. Liu, F. Theberge, J.-F. Daigle, P. T. Simard, S. M. Sarifi, Y. Kamali, H. L. Xu, and S. L. Chin. An efficient control of ultrashort laser filament location in air for the purpose of remote sensing. *Appl. Phys. B*, 85(1):55–58, 2006.

[52] S. Eisenmann, E. Louzon, Y. Katzir, T. Palchan, A. Zigler, Y. Sivan, and G. Fibich. Control of the filamentation distance pattern in long-range atmospheric propagation. *Opt. Express*, 15(6):2779–2784, 2007.

[53] Y. Kamali, Q. Sun, J.-F. Daigle, A. Azarm, J. Bernhardt, and S. L. Chin. Lens tilting effect on filamentation and filament-induced fluorescence. *Opt. Commun.*, 282(5):950–954, 2009.

[54] R. Ackermann, E. Salmon, N. Lascoux, J. Kasparian, P. Rohwetter, K. Stelmaszczyk, S. Li, A. Lindinger, L. Woste, P. Bejot, L. Bonacina, and J.-P. Wolf. Optimal control of filamentation in air. *Appl. Phys. Lett.*, 89(17):171117, 2006.

[55] P. Rohwetter, M. Queisser, K. Stelmaszczyk, M. Fechner, and L. Woste. Laser multiple filamentation control in air using a smooth phase mask. *Phys. Rev. A*, 77(1):013812, 2008.

[56] P. Polynkin, M. Kolesik, J. V. Moloney, G. A. Siviloglou, and D. N. Christodoulides. Curved plasma channel generation using ultraintense airy beams. *Science*, 324(5924):229–232, 2009.

[57] N. Subhash, S. C. Kartha, and K. Sathianandan. New vibrational bands in nitrogen laser emission spectra. *Appl. Opt.*, 22(22):3612–3617, 1983.

[58] K. Kremeyer. Shock wave modification method, apparatus, and system. *US Patent*, (6,527,221; 7,063,288; 7,121,511; 7,648,100; 8,079,544; 8,141,811; 8,511,612; 8,534,595), 2002.

[59] K. Kremeyer, K. Sebastian, and C.-W. Shu. Computational study of shock mitigation and drag reduction by pulsed energy lines. *AIAA Journal*, 44(8):1720–1731, 2006.

[60] K. Kremeyer and J. Yeak. Method and technique to control laser effects through tuning of parameters such as repetiton rate. *US Patent*, (13/567,809 (Pending)), 2011.

[61] H. J. Kull. Theory of the Rayleigh-Taylor instability. *Phys. Rep.*, 206(5):197–325, 1991.

[62] G. O. Ludwig and M. M. F. Saba. Bead lightning formation. *Phys. Plasmas*, 12(9):093509, 2005.

[63] M. N. Plooster. Shock waves from line sources. Numerical solutions and experimental measurements. *Phys. Fluids*, 13(11):2665–2675, 1970.

[64] M. N. Plooster. Erratum: Shock waves from line sources. Numerical solutions and experimental measurements. *Phys. Fluids*, 14:2248, 1971.

[65] J. Yeak, M. Lenzner, and K. Kremeyer. Femtosecond laser filaments and aerodynamics. In *4th International Symposium on Filamentation*, Tucson, AZ, USA, 2012.

[66] Y.-H. Cheng, J. K. Wahlstrand, N. Jhajj, and H.M. Milchberg. The effect of long timescale gas dynamics on femtosecond filamentation. *Opt. Express*, 21(4):4740–4751, 2013.

[67] G. G. Luther, A. C. Newell, and J. V. Moloney. Short-pulse conical emission and spectral broadening in normally dispersive media. *Opt. Lett.*, 19(11):789–791, 1994.

[68] O. G. Kosavera, V. P. Kandidov, A. Brodeur, C. Y. Chien, and S. L. Chin. Conical emission from laser-plasma interactions in the filamentation of powerful ultrashort laser pulses in air. *Opt. Lett.*, 22(17):1332–1334, 1997.

[69] N. Akozbek, S. A. Trushin, A. Baltuska, W. Fuss, E. Goulielmakis, K. Kosma, F. Krausz, S. Panja, M. Uiberacker, W. E. Schmid, A. Becker, M. Scalora, and M. Bloemer. Extending the supercontinuum spectrum down to 200 nm with few-cycle pulses. *New J. Phys.*, 8(9):177, 2006.

[70] P. Maioli, R. Salame, N. Lascoux, E. Salmon, P. Bejot, J. Kasparian, and J.-P. Wolf. Ultraviolet-visible conical emission by multiple laser filaments. *Opt. Express*, 17(6):4726–4731, 2009.

[71] J. Kasparian, P. Bejot, J.-P. Wolf, and J. M. Dudley. Optical rogue wave statistics in laser filamentation. *Opt. Express*, 17(14):12070–12075, 2009.

[72] D. R. Lide, editor. *CRC Handbook of Chemistry and Physics*. CRC Press, 82nd edition, 2001.

[73] R. E. Meyerott, J. Sokoloff, and R. W. Nicholls. Absorption coefficients of air. *Geophysical Research Papers*, (68), 1960.

[74] R. P. Turco and F. Gilmore. Ozone formation and ion chemistry in oxygen radiolysis. *DTIC Technical Report*, (ADA176699), 1986.

[75] M. Wilson. A long-lived optical waveguide made out of thin air. *Phys. Today*, 67(3):16–18, March 2014.

[76] M. Chateauneuf, S. Payeur, J. Dubois, and J.-C. KIeffer. Microwave guiding in air by a cylindrical filament array waveguide. *Appl. Phys. Lett.*, 92(9):091104, 2008.

[77] M. Capitelli, C. M. Ferreira, B. F. Gordiets, and A. I. Osipov. *Plasma Kinetics in Atmospheric Gases*. Springer-Verlag, Berlin, 2000.

[78] I. A. Kossyi, A. Yu Kostinsky, A. A. Matveyev, and V. P. Silakov. Kinetic scheme of non-equilibrium discharge of nitrogen-oxygen mixtures. *Plasma Sources Sci. T.*, 1(3):207–220, 1992.

[79] J. C. Walling, O. G. Peterson, H. P. Jenssen, R. C. Morris, and E. W. O'Dell. Tunable alexandrite lasers. *IEEE J. Quantum Electron.*, 16(12):1302–1315, 1980.

[80] W. Koechner. *Solid-State Laser Engineering.* Springer-Verlag, Berlin, 5th edition, 1999.

[81] R. V. Lovberg, E. R. Wooding, and M. L. Yeoman. Pulse stretching and shape control by compound feedback in Q-switched ruby laser. *IEEE J. Quantum Electron.*, 11(1):17–21, 1975.

[82] S. M. Oak, K. S. Bindra, B. S. Narayan, and R. K. Khardekar. A fast cavity dumper for picosecond glass laser. *Rev. Sci. Instrum.*, 62(2):308–312, 1991.